

Image-Based Mechanical Characterization of Soft Tissue using Three Dimensional Ultrasound

A dissertation presented

by

Petr Jordán

to

The School of Engineering and Applied Sciences

in partial fulfillment of the requirements

for the degree of

Doctor of Philosophy

in the subject of

Engineering Sciences

Harvard University

Cambridge, Massachusetts

August 2008

©2008 - Petr Jordán

All rights reserved.

Image-Based Mechanical Characterization of Soft Tissue using Three Dimensional Ultrasound

Abstract

Computational biomechanical models have become integral components in many areas of modern medical care, including diagnostic applications, image-guided procedures, robot-assisted procedures, and surgical simulators. The development of appropriate models for the mechanical behavior of soft tissues is challenging due to the inherent complexities of the material response, and the limitations on testing protocols associated with *in vivo* settings. Current *in vivo* soft tissue testing is dominated by indentation due to the simplicity of the instrumentation and low risk of injury associated with the procedure. Much of the information related to the interplay between shear and bulk compliance in the complex deformation field beneath the indenter is lost when capturing the single (time-displacement-force) output of the tool. Supplemental experimental methods are necessary for well-conditioned characterization of the tissue response. Image-based methods are a promising solution, as they provide the means for noninvasive *in vivo* measurement of the tissue response with improved sensitivity and uniqueness of the recovered material parameters.

A constitutive inverse modeling framework is presented, relying on conventional indentation testing along with real-time three dimensional ultrasound imaging of the internal tissue deformation. The internal organ deformation field is estimated with a novel, mechanically regularized nonrigid image registration algorithm. A physically-based visco-elastic constitutive model of the liver response is developed and its material parameters are estimated within the proposed inverse modeling framework. Three perfused porcine livers were characterized using tests representative of surgical manipulation, including cyclic loading tests spanning applied strain rates between 0.01 s^{-1} and 1.0 s^{-1} and stress relaxation tests. The proposed model and the identified material parameters offer good fit to the experimental response and show good predictive capability for alternative loading histories. The proposed material testing methods are independent of imaging modality and constitutive law, suggesting potential applications for other tissues and scales (i.e. nanoindentation, confocal microscopy, etc.).

Contents

| | |
|--|-----------|
| Title Page | i |
| Abstract | iii |
| Table of Contents | v |
| Acknowledgments | viii |
| Dedication | xiii |
| 1 Introduction | 1 |
| 1.1 Tissue Modeling and Characterization | 4 |
| 1.2 Thesis Overview | 7 |
| 2 Modeling the Generalized Nominal Response of Soft Tissues | 10 |
| 2.1 Introduction | 10 |
| 2.2 Methodology | 14 |
| 2.2.1 Generalized Stress-Strain Response | 14 |
| 2.2.2 System Equations and Solution Approach | 15 |
| 2.2.3 Elastic Constitutive Elements | 18 |
| 2.2.4 Viscous Constitutive Elements | 19 |
| 2.2.5 Data Fitting and Nonlinear Parameter Optimization | 23 |
| 2.3 Results | 24 |
| 2.3.1 Applications to Other Tissues | 29 |
| 2.4 Discussion and Conclusions | 30 |
| 3 Estimating Experimental Tissue Deformation | 40 |
| 3.1 Introduction | 40 |
| 3.2 Relation to Existing Work | 43 |
| 3.2.1 Nonrigid Image Registration Algorithms | 47 |
| 3.2.2 Framework for Image-Mechanics Coupling | 50 |
| 3.3 Methodology | 53 |
| 3.3.1 Mechanical Regularization Framework | 53 |
| 3.3.2 Meshing | 54 |
| 3.3.3 Local Optical Flow Estimation | 56 |
| 3.3.4 Mechanically Regularized Deformation | 58 |
| 3.4 Evaluation and Results | 62 |

| | | |
|----------|--|------------|
| 3.4.1 | Synthetic Unit Cube: Unconfined Uniaxial Compression . . . | 64 |
| 3.4.2 | Synthetic Unit Cube: Torsion | 68 |
| 3.4.3 | Liver Indentation: Inner Field Estimation | 70 |
| 3.5 | Discussion | 72 |
| 4 | Image-Based Mechanical Characterization of Soft Tissues | 76 |
| 4.1 | Introduction | 76 |
| 4.2 | Methods | 78 |
| 4.2.1 | Experimental Setup | 79 |
| 4.2.2 | Nonrigid Image Registration and Constitutive Modeling | 81 |
| 4.2.3 | Method Validation: Synthetic Volumetric Data | 87 |
| 4.2.4 | Perfused Porcine Liver Constitutive Modeling | 90 |
| 4.3 | Results | 91 |
| 4.3.1 | Method Validation: Synthetically Generated Volumetric Data | 91 |
| 4.3.2 | Perfused Porcine Liver Constitutive Modeling | 93 |
| 4.4 | Conclusions and Discussion | 96 |
| 5 | Viscoelastic Characterization of Perfused Porcine Liver | 100 |
| 5.1 | Introduction | 100 |
| 5.2 | Materials and methods | 102 |
| 5.2.1 | Design of experiments | 102 |
| 5.2.2 | Finite-element model | 107 |
| 5.2.3 | Mesh Convergence | 115 |
| 5.2.4 | Internal Deformation Field Estimation | 115 |
| 5.2.5 | Material parameter estimation | 118 |
| 5.3 | Results | 121 |
| 5.3.1 | Sensitivity Analysis | 132 |
| 5.3.2 | Validation | 134 |
| 5.4 | Discussion | 137 |
| 6 | Conclusion and Future Work | 145 |
| 6.1 | Image-based Mechanical Characterization of Soft Tissues | 145 |
| 6.2 | Nonrigid Image Registration for Image-Guided Surgery | 146 |
| 6.3 | Future Directions | 147 |
| 6.4 | Final Words | 150 |
| | Bibliography | 152 |
| A | Deriving Laplacian-Smooth Horn & Schunck Optical Flow | 164 |
| A.1 | Euler-Lagrange Equations | 170 |
| A.1.1 | Gradient-Smooth Horn & Schunck | 170 |
| A.1.2 | Laplacian-Smooth Horn & Schunck | 171 |

Acknowledgments

I have been waiting five years for the opportunity to write these introductory words about my graduate school experience. And frankly, a few times along the way I did not think that this moment would actually come. When I started my graduate journey in 2003, I was told that this experience would test my mental stamina and determination, but often times the difference between a successful thesis and the alternative is determined by the mentors and colleagues one surrounds himself with. I took these words to heart and, five years later, I can overwhelmingly attest to the validity of that observation. I can also reflect on the frightful alternatives, had I not been so fortunate in surrounding myself with such an outstanding team of mentors, colleagues, and friends.

When I initially met with my adviser, Professor Robert D. Howe, to discuss my potential doctoral project, combining signal processing, medical imaging, finite-element modeling, and biomechanical tissue testing, I can only remember thinking “Oh boy, what did I get myself into!” What I did not know at the time, however, was the fact that I would be very fortunate to assemble a thesis committee team, spanning all of these diverse areas, that would successfully guide me through these formidable waters of multidisciplinary research.

My advisor, Professor Robert D. Howe, was the fearless leader, whose sense of direction, always keeping the big picture in mind, and expertise in all of the above areas were essential in steering this project toward success. Additionally, I cannot say enough about the endless and tireless help and direction of Professor Simona Socrate, a bona fide finite-element modeling guru and an expert in tissue mechanics. She spent countless hours working with me on mechanical models and was always enthusiastic to teach me something new about mechanics just about every time we met. Professor Todd Zickler and his expertise in computer vision provided the necessary expertise and sense of direction in the imaging intricacies of the project. He has always provided fresh insight and suggestions on my work, especially in times of desperation and has always shown a great aptitude for encouragement. I will always be thankful for all of the contributions and guidance of my thesis committee and, in retrospect, it is now apparent that it would have been difficult not to succeed under their tutelage.

The graduate school experience is most certainly defined by the research group and fellow graduate students, postdocs, and undergraduate students. The five years spent in the Biorobotics Laboratory have truly been a life changing experience, allowing me to work with some of the brightest and smartest engineers and scientist, who also happened to be great friends to hang out and have a beer with. Amy Kerdok, my big sis, was the biggest mentor of them all. Starting from the first apartment hunt, to passing all the wisdom of being a dual citizen at Harvard and MIT, to the liver modeling methodology and expertise she has developed during her impressive graduate career. In fact, much of this work would not have been possible without Amy’s work on liver modeling, experimental protocols, devices, and most importantly the data she has tirelessly collected. The next person that deserves much credit is Doug Perrin, the wise and supportive postdoc, who was always there to not only bounce ideas, but also as a friend. I have always been amazed with Doug’s ability to

have an educated opinion on all subjects in life. In fact, much of my exploration of interesting problems in computer vision and science in general were sparked by my conversations with Doug and he has certainly shaped the direction of my graduate career. I also must thank Shelten Yuen for always being willing to brainstorm with me and offer his brilliant analytical mind to provide fresh perspectives on hard problems I faced along the way. I feel an enormous deal of gratitude to all the graduate students - Rob, Sam, Pete, Paul, Aaron, Chris, Ryan, Sol, Anna, Heather, and Yuri; the postdocs - Marius and Mahdi; and the brightest undergraduates I had the privilege to work with - Yi, Cami, Diana, Ross, Dan, and Jackie.

Much of my graduate career was defined by my association with the Harvard-MIT Division of Health Sciences and Technology (HST), undoubtably the most unique medical engineering and clinical training program for engineers and scientist. While balancing medical school classes and research was quite a challenge, some of my most fun and rewarding times came during my HST training. Anatomy dissections are certainly something I will remember for the rest of my life, but most importantly the time spent caring for patients and learning the ins and outs of clinical medicine in the ICM series were the paramount experience of my graduate training. At times of disillusion with engineering and science, a quick recollection of my experiences with the patients at Mt. Auburn Hospital seemed to quickly recharge my determination to work on projects and ideas that may positively impact the quality of healthcare.

While reflecting on my graduate school experience, I must not forget my undergraduate mentors at Lipscomb University, who were instrumental in my motivation to pursue a doctoral degree. Dr. George O'Connor has taught me all there is to know about engineering design, circuit analysis, signals & systems, and digital design. I have always appreciated our friendship, as he was always there to discuss all topics in life, whether it may be science, politics, philosophy, or religion. In retrospect, I am amazed at how single seemingly insignificant events, such as a visit to Professor's office, may completely shape one's future direction and, in my case, future career. I owe much of my early exposure to biomedical research to my undergraduate research advisor, Dr. Alan Bradshaw, who gave me the opportunity to explore exciting problems in medical sciences and engineering. Alan was a wonderful mentor and a friend and I owe much of my motivation to pursue biomedical research to him.

Getting to this point was not necessarily an easy journey and it certainly had its cost in terms of missing out on the time spent with immediate and extended family. Unfortunately, my grandmother Bozena and my grandfather Emil passed away just a few months before having the opportunity to celebrate the completion of my studies and I will missed them greatly.

My parents, Milos and Vera, have always been there to support me and encouraged me to pursue my dreams, even at the cost of leaving the home when I was sixteen. In many ways, I feel that my accomplishments are just as much their accomplishments and I will always be grateful for their sacrifices to give me the best opportunity to succeed. My brother Paul and sister Lenka are the best older siblings one could ask

for and I believe that it is now time for me to repay them for putting up with the little brother. Finally, I would like to thank my wife, Brooke, who has been there for me throughout it all. She has always been the cheerleader and the emotional crutch when things got rough and I would not have finished this journey without her support.

I will always look at my graduate school years with fond memories, despite all the stresses, demands, and sleepless nights. I think it is a true testament to the wonderful people I was surrounded with and supported by during these years. In fact, it is ironic that I have come across some of the warmest and most thoughtful people during my years in Boston, one of the coldest cities in the United States.

*Dedicated to my parents Věra and Miloslav,
my brother Pavel, my sister Lenka,
and my wife Brooke.*

Chapter 1

Introduction

The rapid development of computer-assisted medical technologies over the past two decades has created a strong demand for accurate biomechanical models of tissues and whole organs. Computational biomechanical models have become integral components in many areas, including diagnostic applications, image-guided procedures, robot-assisted procedures, and surgical simulators. The development of appropriate models involves two general challenges. The first difficulty lies in the formulation of a suitable constitutive law capable of capturing the large-strain, nonlinear, viscoelastic response of tissues. The second challenge involves the development of experimental testing protocols appropriate for unique identification of the material parameters. The aim of this thesis is to develop a framework for constitutive modeling of the liver mechanical response, including methods for rapid model prototyping, material parameter estimation, and image-based inverse modeling. The contributions of this work rely on the fusion of methods from computational biomechanics, computer vision, and medical image processing.

Image-Guided Procedures

Mechanical models of soft tissues are an important component of emerging image-guided procedures, especially in applications where mechanically accurate registration of image data is necessary for intra-operative guidance. Image-guided tasks, such as tumor localization during brain shift [6, 29, 87, 131, 127], liver resection [26], needle biopsy and prostate brachytherapy [2, 46, 4, 5, 38, 37, 36, 98, 130], require a close interplay of computational biomechanical models with preoperative and intra-operative imaging. Soft tissue procedures often involve large strains, instrument-tissue contact, and fracture (i.e. cutting) of tissues. This necessitates the use of sophisticated mechanical modeling techniques and complex constitutive laws that accurately capture the large-strain, viscoelastic, and highly nonlinear response of soft tissue. The materials models must then be validated and parameterized by experimental testing protocols appropriate for unique identification of the material

constants. Additionally, the observed patient-to-patient mechanical variability of soft tissues often requires patient-specific (personalized) models, which must be generated and parameterized with clinically feasible testing protocols.

Surgical Simulation

Medical training simulators and virtual surgical environments aim at improving the quality of medical personnel training [34], reducing training cost, and eliminating the need for animal subjects. In general, surgical simulators fall in the categories of simulators for minimally invasive surgery (MIS) [121, 74, 123], catheter and needle-based procedures [124, 81], and open surgery [20, 15]. Simulation of MIS procedures, including arthroscopic, laparoscopic, and catheter procedures, has seen a vast amount of work over the recent years, as it requires the surgeons to develop specific technical skills to work with the contra-intuitive mapping between the motions of the surgeon's hand and the motion of the instrument. The patient benefits of minimally invasive surgery over open surgical procedures are well documented [86, 107, 123] and include: shorter recovery time, lower risk of complications, smaller incisions, and less local tissue damage. MIS procedures, however, are intrinsically more difficult due to the associated decrease in dexterity, loss of visual information, and limited or nonexistent haptic feedback. Gallagher and Cates [49] have presented compelling evidence that virtual reality based simulators can be effective in skill assessment and training.

The role of computational soft tissue models in surgical simulation is to improve the realism and accuracy of the visual and haptic feedback. Additionally, the models must predict the tissue behavior during common tasks, such as cutting, suturing, clamping, etc. The large deformation response of heterogeneous soft biological tissues is nonlinear, time and rate-dependent, making the formulation of fast and accurate models challenging.

Other Applications

Other clinical applications of soft tissue models include, but are not limited to, image segmentation [19], robot-assisted surgical procedures [92], and applications in disease detection and diagnosis. For example, mechanical properties of breast tissue, have been shown to correlate with histopathologic changes [73, 129, 70], the mechanical properties of cervical tissue have been linked to cervical incompetency [95], and Carter et al. [24] have shown changes in mechanical properties associated with liver disease.

1.1 Tissue Modeling and Characterization

Much of the soft tissue experimental data reported in the literature has been acquired *ex vivo*. This data, however, is often inappropriate for accurate modeling

and characterization, as the material properties of soft tissues vary significantly between *in vivo* and *in vitro* settings [48, 91, 93, 53, 90, 71]. The liver is a frequently manipulated organ during abdominal procedures, therefore mechanical modeling and characterization of its response is a crucial step towards improving surgical simulation and image-guided procedures. The liver is a complex organ composed of vascular, structural, and cellular elements (blood, bile, lymph, collagen, hepatocytes, endothelial cells), which requires a constitutive model capable of capturing its nonlinear, viscous, and rate-dependent response. Because the liver is a highly perfused organ, its observed mechanical properties are strongly dependent on the physiological conditions (i.e. temperature, arterial pressure, venous pressure, orientation, etc.). A recent study by Nava et al. [96] and a study by Carter et al. [24] report on the measurements of intra-operative *in vivo* mechanical properties of human liver. Numerous other studies [23, 100, 112, 125, 97] have performed *in vivo* mechanical tests in porcine and bovine animal models. Kerdok et al. [71] have demonstrated that near *in vivo* mechanical behavior may be achieved by using physiologic perfusion conditions in an *ex vivo* setting.

Current *in vivo* soft tissue testing is dominated by indentation due to the limited access requirements, simplicity of the instrumentation, and low risk of injury associated with the procedure [11]. The single force-displacement history obtained during conventional indentation experiments is governed by the mechanical response of the whole material domain, combining near-field (large strain) and far-field (low strain) contributions. Much of the information related to the interplay between shear and bulk compliance in the complex deformation field beneath the indenter is lost when capturing this single output. Therefore, supplemental experimental methods, such as secondary indentation sensors [11], tissue surface tracking [41, 42], or independent tests of bulk compliance (i.e. confined tissue compression) are necessary for well-conditioned parameter identification. Image-based characterization methods are a promising solution, as they provide the means for noninvasive, *in vivo* estimation of material parameters and offer improved sensitivity and uniqueness of recovered parameters. This thesis proposes an image-based approach to estimation of constitutive model parameters, which combines conventional indentation tests with real-time volumetric imaging using three-dimensional ultrasound. The parameter estimation process relies on a nonlinear inverse finite-element modeling approach, which iteratively adjusts material properties to obtain good agreement between experimental and modeled response of the tissue (Figure 1.1).

Elastography

Elastographic imaging is an area of research related to the methods proposed in this thesis. Elastography [99], a technique for noninvasive imaging of soft tissue elasticity, has witnessed an immense growth over the past decade due to its vast diagnostic potential in breast cancer [51, 50, 59], prostate cancer [67, 3], liver fibrosis

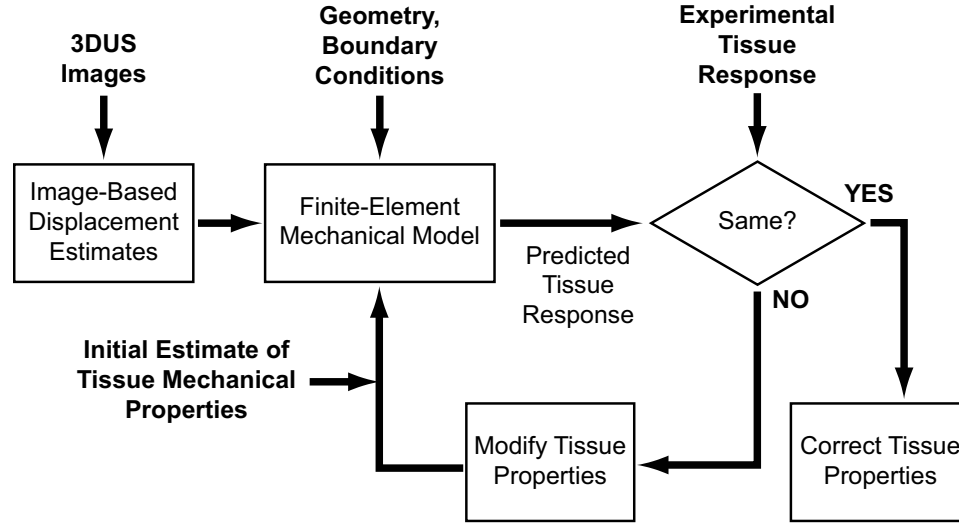


Figure 1.1: Image-based approach to material property estimation using iterative finite-element modeling.

[77], and congenital heart disease [35, 12]. The key concept behind elastography is estimation of strain fields resulting from uniaxial tissue compression (usually less than 1% nominal strain). Traditional elastography [99] uses a 2D ultrasound probe to compress a tissue sample and estimates the resulting 2D strain field (elastogram) from radio-frequency (RF) echo lines in the region of interest. As changes in mechanical properties of soft tissues have been demonstrated to correlate with pathophysiology [73, 129], an elastogram can localize stiff nodules with sensitivities superior to manual palpation. Other techniques, such as sonoelastography and magnetic resonance (MR) elastography, rely on propagation of slow acoustic waves (100-1000 Hz) to estimate local elastic moduli. In general, elastographic techniques assume that soft tissues behave as isotropic linear elastic materials and aim to detect local variations of elastic moduli. In contrast, the tissue characterization methods in this thesis neglect relative fluctuations in material properties and place the focus on accurate prediction of the large-displacement viscous behavior of the whole organ.

1.2 Thesis Overview

This thesis expands on the work of Kerdok [69], which developed an extensive testing and characterization protocol and proposed a nonlinear, visco-poro-elastic constitutive model to capture the response of perfused porcine liver. The main contributions are:

1. Introduction of a simplified constitutive modeling framework, using generalized

nominal response of tissues to identify the simplest constitutive form capable of capturing the salient features of their time-dependent response;

2. Formulation of a revised and simplified constitutive law, while maintaining excellent model-experiment agreement and reducing the number of material parameters;
3. Development of a mechanically constrained non-rigid image registration algorithm for estimation of the three-dimensional internal tissue strain field;
4. Incorporation of image-based volumetric imaging into the inverse finite-element tissue modeling;
5. Complete visco-elastic characterization and validation of the proposed model using three perfused porcine liver specimens.

Chapter 2 addresses the challenge of formulating an appropriate soft tissue constitutive law by presenting a general approach to constitutive modeling of the generalized stress-strain time-dependent behavior. This chapter proposes a general rheological framework, consisting of elastic and viscous elements, which may be altered in a modular fashion to rapidly prototype various constitutive laws and their ability to capture various aspects of the tissues time-dependent response. The conclusions of this chapter and the identified constitutive formulation serve as the basis for the final constitutive liver model presented in Chapter 5.

Chapter 3 proposes a novel nonrigid image registration algorithm, which uses mechanical finite-element models to regularize sparsely estimated local displacements to obtain global deformation fields that are consistent with the mechanical response of the involved tissues. The algorithm is not only suitable for classical image registration problems, such as intra-operative guidance in neurosurgery, liver surgery, or prostate radiotherapy, but is also an appealing technique for estimation of organ deformation during mechanical testing.

Chapter 4 addresses the use of the nonrigid image registration algorithm in constitutive model development and material parameter identification using conventional visco-elastic and poro-elastic constitutive laws. The parameter identification process is also validated on synthetic data and shown to provide good accuracy and consistent convergence to correct material parameter values.

Chapter 5 introduces a revised nonlinear visco-elastic constitutive model, which captures the response of liver across a wide range of frequencies (DC-2 Hz), as well as accurately predicts the organ's stress relaxation response. The model is validated by demonstrating good agreement with experimental response obtained from alternative loading histories.

Chapter 6 provides a discussion of the contributions of this work, both in the areas of constitutive liver modeling as well as nonrigid image registration. While this

work proposes a soft tissue modeling and characterization framework using perfused porcine liver and 3D ultrasound imaging, it is suitable for *in vivo* organ testing and some future work considerations are discussed. Additionally, the methods are directly applicable to other imaging modalities, tissue, as well as to other scales (i.e. nano-indentation and cellular mechanics).

Chapter 2

Modeling the Generalized Nominal Response of Soft Tissues

2.1 Introduction

Accurate characterization of the mechanical behavior of biological soft tissues is a necessary step for advancing many medical technologies including surgical simulation, image-guided procedures, robot-assisted surgery, and diagnostic procedures. The complex structure and nonlinear elastic and dissipative behavior of tissues make modeling their mechanical response challenging. Soft biological tissues have been likened to cross-linked polymers since their structural components consist of protein fibers (collagen and elastin). Soft tissues often display limited volumetric compliance, as they are filled with fluids (blood, lymph, ground substance, etc.) and can often undergo large strains before failure [45, 48]. Furthermore, they exhibit stresses that vary nonlinearly with finite strains, have loading rate and time dependencies, are anisotropic, achieve an equilibrium compliance under relaxation, and are sensitive to the conditions (e.g. temperature and hydration) under which they are tested [126]. Since medical manipulations typically involve large deformations with complex geometries and boundary conditions, realistic modeling of soft tissues requires characterization of the large strain response of the tissues often across a range of time scales.

Researchers have modeled soft tissues using an array of simple elastic [27, 66, 100] as well as complex constitutive models that include nonlinear elastic, viscous, and porous elements [16, 22, 23, 24, 33, 68, 72, 88, 96, 109, 118, 119]. Viscoelastic material characterization is accomplished by varying loading histories over different modes of deformation since volume changes (bulk) and shape changes (shear) relate to different mechanisms of deformation [126]. Common modes of deformation used on soft tissues include: uniaxial compression/extension [43, 62, 88, 89, 95], shear [39, 82], indentation [22, 24, 71, 69, 72, 100], torsion [66, 125], grasping [23], and aspiration [97]. To

characterize the time-dependent large strain response of soft tissues a few loading histories are commonly used: creep response to a constant step load [71], stress relaxation to a constant step displacement [23, 95, 109, 69], and constant strain rate ramp loading and unloading [23, 72, 95, 69]. Though not applicable to large deformations, the dynamic stress response to sinusoidally oscillating small strains is also commonly measured to provide insight into the balance between energy storage and dissipation in the material [45, 48, 69, 100, 126]. Each of these tests captures different aspects of the viscoelastic behavior of the material at different time scales and thus more than one is necessary for complete material characterization.

The utility of a model lies in its ability to accurately and efficiently predict the desired mechanical responses of the material. Three-dimensional constitutive models of soft biological tissues are required to reflect both the complexity of the time dependent response, and the dependence of the response on the mode of deformation. The process of formulating a predictive 3D model can be both time-consuming and challenging, as the path to success is not well defined and often an iterative approach of “trial and error” is utilized. Typically, the material model parameters are estimated by fitting the experimental response through finite-element implementation of the full constitutive formulation and iteratively solving the inverse problem. Considering an experimental response of a given tissue (for example, see Fig. 2.3 for the time-dependent response of liver in indentation), it is a challenging task to determine which constitutive law is appropriate for the specific application and tissue type. Furthermore, the new applications of biomechanical models, especially in image-guided procedures, require characterization of a wide array of tissues with distinct mechanical response characteristics. Following the “trial and error” procedure before ascertaining that the assumed form of the model is able to reproduce the main features of the observed tissue behavior can be unnecessarily time intensive and inefficient.

When modeling the mechanical response of the whole organ, it can be argued that the salient features of its time-dependent, dissipative response can be separated from the contributions due to the geometry and the boundary conditions of the organ. Within the first order of approximation, therefore, the characteristic features of the tissue response may be initially modeled with a simplified one-dimensional model. We propose the use of a one-dimensional computational testbed for the determination of the simplest and most appropriate rheological configuration, which efficiently captures the necessary features of the response (e.g. nonlinear force-displacement, hysteresis with full recovery, non-exponential stress relaxation) with the fewest material parameters. We have developed an analytical tool that allows users to explore the form and the response of common visco-elastic rheological configurations and allows for any linear or nonlinear constitutive relations to govern the response of the individual elastic and dissipative elements. The tool also incorporates a nonlinear optimization scheme that identifies material parameter values by minimizing the error between experimental data and predicted model response. A MATLAB (Mathworks Inc., Natick, MA, USA) implementation of the tool is made freely available on the au-

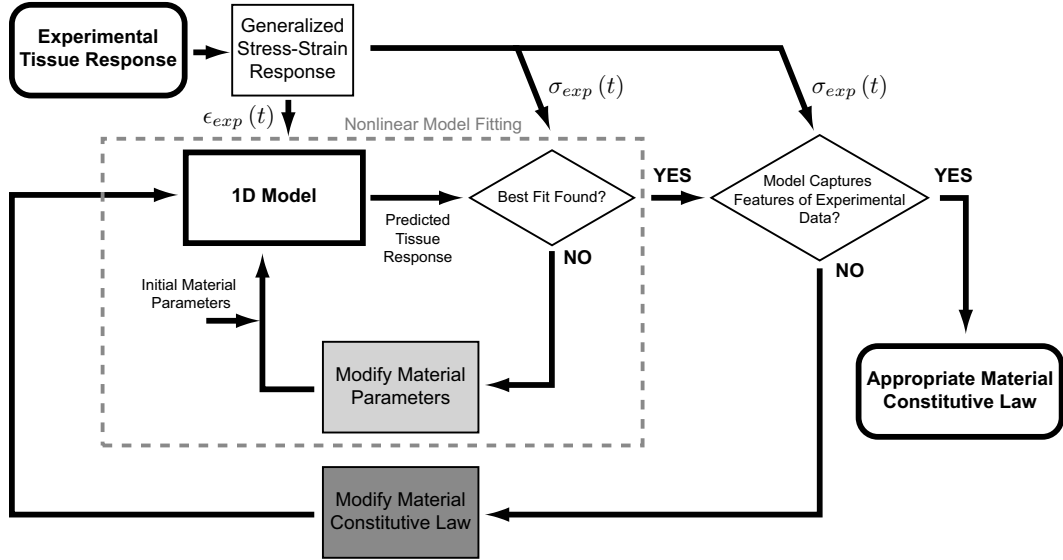


Figure 2.1: A schematic view of the constitutive model selection process, comprising an “inner loop” for material parameter fitting and an “outer loop” for constitutive law adjustments.

thor’s website and is easily extensible with user-defined constitutive elements. Using this initial constitutive modeling paradigm illustrated in Figures 2.1, the proposed tool facilitates the fitting of a wide array of constitutive laws to experimental data and aids in the determination of the simplest and most appropriate configuration before proceeding with full three-dimensional modeling. To demonstrate the utility of the tool, we subjected perfused porcine liver to complete viscoelastic testing in indentation and determined the form of the minimal rheological model necessary to reproduce the observed behavior. The same approach was then followed to determine forms of the model that could reproduce the characteristic tissue responses of brain tissue in indentation and cervical tissue in compression.

2.2 Methodology

2.2.1 Generalized Stress-Strain Response

In the following sections, we describe a modeling methodology intended for initial development of constitutive material laws. Considering various single input-output relationships obtained from experimental material tests, we introduce the concept of generalized one-dimensional nominal response. Intuitive examples of single input-output relationships include test measurements with loading conditions, such as indentation, uniaxial compression or tension, confined compression, applied torsion, or

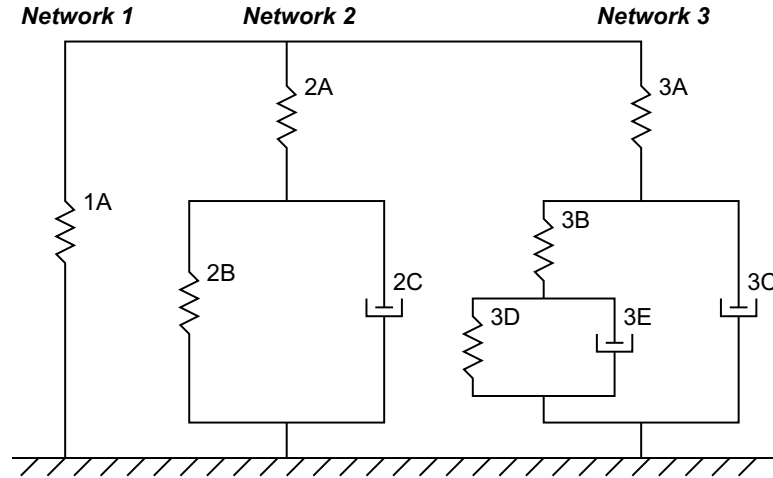


Figure 2.2: General rheological arrangement comprising three parallel networks of increasing complexity.

surface aspiration [85, 96]. All of these loading conditions can be examined in terms of their generalized time-dependent nominal stress-strain behavior. In indentation, for example, nominal stress can be obtained by dividing the load of the indenter by its cross-section area and the nominal strain can be defined as the indenter displacement divided by the sample thickness. Similarly, in surface aspiration tests, the generalized stress can be defined as the applied pressure, while the resulting surface deflection divided by the diameter of the suction device may be considered as an appropriate measure of nominal strain. The generalized one-dimensional nominal stress-strain response serves as a basis for the proposed modeling approach, in which we aim to identify the necessary viscous and elastic components and their rheological arrangement, which is consistent with the observed time-dependent response.

2.2.2 System Equations and Solution Approach

In Figure 2.2 we propose a general rheological arrangement, which we find to be sufficiently broad to capture the response of most soft tissues. It comprises three branches of increasing complexity with individual constitutive elements (springs and viscous dashpots), which may be defined (and deactivated) in a modular way to accommodate for a large number of rheological configurations. The first branch comprises only an elastic element (1A). The second branch is in the configuration of the standard linear solid (SLS) element with an instantaneous response through the elastic element (2A) and viscous dissipative response (2C) with a corresponding back stress provided by an elastic element 2B. The third network increases the complexity of the second network by introducing a time-dependent back stress to capture the

response of materials with dissipative mechanism with distinctly different relaxation times. The time-dependent back stress is incorporated through an SLS arrangement comprised of the two elastic elements (3B and 3D) and a viscous element (3E).

Out of this complex rheological arrangement, it is possible to construct simpler models by deactivating individual elements. To eliminate the contributions of an elastic element, it is defined as either completely rigid or infinitely compliant, depending on its serial or parallel arrangement with the neighboring elements. Analogously, viscous elements are deactivated by specifying their viscous flow resistance to zero. For example, isolated network 3 may be reduced to network 2 by deactivating the elastic element 3D (making it fully rigid) and viscous element 3E. Similarly, we can deactivate networks 2 and/or 3 by making elements 2A and 3A infinitely compliant. We may also construct a rheological arrangement for viscoelastic fluid by deactivating 3D, 2B, and 1A.

To compute the response of a given rheological arrangement, we use standard numerical techniques for solving systems of ordinary differential equations [114]. The model is given a prescribed strain history, while the stress and accumulated strain histories in each component of the network are computed by integration of the corresponding differential equations. The system of equations that describes the response of the whole system consists of the constitutive equations of each element and the compatibility equations and equilibrium equations for the system.

The compatibility equations for the proposed general system may be written as

$$\epsilon_{exp} = \epsilon_1^A = \epsilon_2^A + \epsilon_2^B = \epsilon_3^A + \epsilon_3^B + \epsilon_3^D \quad (2.1)$$

$$\epsilon_2^B = \epsilon_2^C \quad (2.2)$$

$$\epsilon_3^D = \epsilon_3^E \quad (2.3)$$

$$\epsilon_3^C = \epsilon_3^B + \epsilon_3^D, \quad (2.4)$$

where the subscript denotes the network and the superscript denotes the element within the network (i.e. ϵ_3^A is the strain in element 3A). The equilibrium equations for the proposed system are

$$\sigma_{total} = \sigma_1^A + \sigma_2^A + \sigma_3^A \quad (2.5)$$

$$\sigma_2^A = \sigma_2^B + \sigma_2^C \quad (2.6)$$

$$\sigma_3^A = \sigma_3^B + \sigma_3^C \quad (2.7)$$

$$\sigma_3^B = \sigma_3^D + \sigma_3^E \quad (2.8)$$

The constitutive equations describe the characteristic response of individual elements. The elastic elements are described in terms of a constitutive relationship between the elastic strain (ϵ^e) in the element and the corresponding stress (σ^e):

$$\sigma^e = f(\epsilon^e). \quad (2.9)$$

The response of viscous elements may be explicitly prescribed through a constitutive relationship determining the rate of viscous deformation ($\dot{\epsilon}^v$) in terms of the driving stress (σ^v):

$$\dot{\epsilon}^v = f(\sigma^v, \chi). \quad (2.10)$$

For certain constitutive formulations the rate of viscous deformation may also depend on the state variables ($\chi = \{\epsilon^v, \dot{\epsilon}^v, \dots\}$) of the viscous element. We consider one relationship in this class in the reptation-limited nonlinear power law, where the rate of viscous deformation depends on the accumulated viscous flow in the element.

2.2.3 Elastic Constitutive Elements

The elastic elements discussed in this chapter comprise the linear elastic law, exponential law, and the freely jointed chain (FJC) model. These formulations are discussed because they have full three-dimensional embodiments (FEM) proposed in the literature (see e.g. Gasser et al. (2006) [52] and Bischoff et al. (2004) [17]). While both the exponential law and the FJC model are capable of capturing highly nonlinear stress-strain relationships, their features are significantly different to warrant the discussion of both. The proposed elastic constitutive elements are summarized in Table 2.1, including their constitutive equations, material parameters, and characteristic stress-strain response curves.

In a simple linear elastic element, the stress is directly proportional to the applied strain ($\sigma^e = E\epsilon^e$) through the stiffness modulus E . In our implementation of the elastic exponential element, the nonlinearity of the stress-strain response is controlled through an initial slope parameter A and an exponential parameter b :

$$\sigma^e = \frac{A}{b} (e^{b\epsilon^e} - 1). \quad (2.11)$$

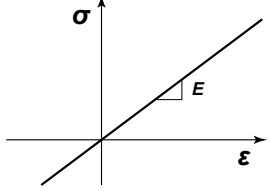
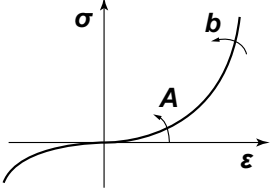
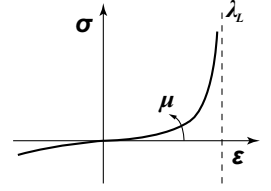
In the FJC model, we introduce a one-dimensional equivalent of the full three-dimensional formulation [7, 118]. In the one-dimensional form, the stress-strain relationship may be expressed as

$$\sigma^e = \mu_0 \lambda_L \left(\frac{\beta \left(\frac{\lambda}{\lambda_L} \right)}{\lambda} - \beta_0 \right), \quad (2.12)$$

where

$$\beta \left(\frac{\lambda}{\lambda_L} \right) = \mathcal{L}^{-1} \left(\frac{\lambda}{\lambda_L} \right) \quad (2.13)$$

Table 2.1: List of elastic constitutive elements, including their constitutive equations, associated parameters, and their characteristic response.

| Elastic Element | Constitutive Equation | Parameters | Response |
|----------------------|--|--------------------|--|
| Linear | $\sigma^e = E\epsilon^e$ | E |  |
| Exponential | $\sigma^e = \frac{A}{b} (e^{b\epsilon^e} - 1)$ | A, b |  |
| Freely Jointed Chain | $\sigma^e = \mu_0 \lambda_L \left(\frac{\beta \left(\frac{\lambda}{\lambda_L} \right)}{\lambda} - \beta_0 \right)$ | μ_0, λ_L |  |

is the inverse of the Langevin function

$$\mathcal{L}(\beta) = \coth(\beta) - \frac{1}{\beta}. \quad (2.14)$$

In this formulation, λ is the material stretch ($\lambda = 1 + \epsilon$) and β_0 is the initial inverse Langevin factor defined through Eq. 2.13 with $\lambda = 1$. The material parameters μ_0 and λ_L determine the initial slope and the asymptotic stretch limit, respectively.

2.2.4 Viscous Constitutive Elements

We introduce two types of viscous constitutive elements, which are summarized in Table 2.2. The first is the standard linear viscous element with a single viscosity parameter η . In most biological materials, however, processes with a range of energy barriers accommodate the viscous flow. Consequently, increasing levels of stress enable additional mechanisms to become active and motivate the need for viscous constitutive relationships in which the viscous strain rate $\dot{\epsilon}^v$ increases nonlinearly with the driving stress, σ^v . We introduce a nonlinear viscous power law defined as

$$\dot{\epsilon}^v = \dot{\epsilon}_0^v \left(\frac{\sigma^v}{S_0} \right)^n, \quad (2.15)$$

where $\dot{\epsilon}_0^v = 1 \text{ s}^{-1}$ is a constant introduced for dimensional consistency, while S_0 and n are model parameters. A physical interpretation of the constitutive parameters, $[S_0, n]$, can be obtained by considering the dependence of viscous strain rate on the driving (viscous) stress. The viscous strength, S_0 , represents the viscous stress necessary to drive viscous strain at a rate of 100% per second ($\dot{\epsilon}_0^v$). The stress exponent, n , represents the stress sensitivity of the viscous mechanisms. For $n = 1$ the model behaves as a linear Newtonian material (with viscosity $S_0/\dot{\epsilon}_0^v$). For larger values of n , the model captures the effects of superposing stress-activated mechanisms on viscous flow, and the viscous rate dramatically increases for stresses exceeding S_0 .

In our experience, a viscous constitutive relationship defined by the nonlinear power law may not be sufficient for some biological materials. For example, as viscous strain in soft tissues accumulates and the collagen network exhausts all possible avenues of reorganization to accommodate the imposed deformation, the viscous strain rate (under constant driving stress) tends to decrease. This is a well-known effect in macromolecular solids [14], where this effect is ascribed to the physics of reptation of elastically inactive macromolecules. Following Bergstrom and Boyce (2001) [14], we express the dependence of strain rate on accumulated viscous deformation through a single additional model parameter, α :

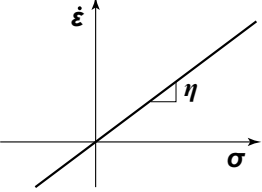
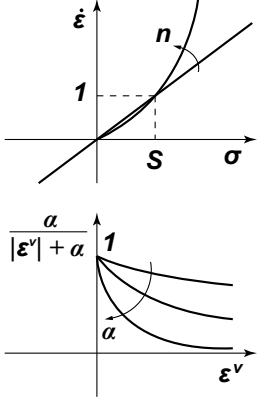
$$\dot{\epsilon}^v = \dot{\epsilon}_0^v \frac{\alpha}{|\epsilon^v| + \alpha} \left(\frac{\sigma^v}{S_0} \right)^n. \quad (2.16)$$

Note that for $\epsilon^v = 0$ the form (Eq. 5.18) of the constitutive relationship is recovered, and, at constant driving stress, the viscous strain rate diminishes with increasing levels of accumulated viscous strain. Typical values of the parameter α are in the range [0.0001 to 0.01], where larger values of α provide the ability to accommodate larger levels of viscous strain through collagen reptation and realignment, and can therefore be associated with loosely cross-linked collagen networks.

2.2.5 Data Fitting and Nonlinear Parameter Optimization

The goal of any modeling methodology is to identify a model configuration and associated model parameters that minimize the difference between the model and the experimental response. We address the choice of the objective function (Φ), which quantify the model-experiment agreement and the method for identification of the models material parameters. In this chapter we follow the intuitive formulation of the objective function in terms of the mean squared error (MSE) between the experimental and modeled stress history defined in discrete-time as

Table 2.2: List of viscous constitutive elements, including their constitutive equations, associated parameters, and their characteristic response.

| Elastic Element | Constitutive Equation | Parameters | Response |
|-----------------|--|------------------|---|
| Linear | $\sigma^v = \eta \dot{\epsilon} \quad \dot{\epsilon} = \frac{\sigma^v}{\eta}$ | η |  |
| Power law | $\dot{\epsilon}^v = \dot{\epsilon}_0^v \frac{\alpha}{ \dot{\epsilon}^v + \alpha} \left(\frac{\sigma^v}{S_0} \right)^n$ | S_0, n, α |  |

$$\Phi(p_n) = \frac{1}{N} \sum_{i=1}^N (\sigma_{exp}[i] - \sigma_{model}[i])^2, \quad (2.17)$$

where σ_{exp} is the experimental stress history, σ_{model} is the modeled response, N is the number of time increments, and p_n is the vector of n material parameters. Under this definition of the objective function, we use the bounded downhill simplex method [76] to iteratively identify the material parameters that minimize $\Phi(p_n)$. The user must be aware that while the downhill simplex method is generally robust, it does not guarantee convergence to global minima for nonconvex objective functions. Repeatable convergence of multiple minimizations initiated from varying initial locations in the parameter space is suggested to evaluate the global convergence for the given objective function.

Alternative definitions of the objective function are an important consideration during the modeling process. For example, it may be beneficial to define $\Phi(p_n)$ as the mean absolute error (MAE) in some situations, to minimize the unwanted contributions from outliers and noise in the experimental data. The formulation of $\Phi(p_n)$ can also be modified to increase the significance of certain features of the model response, by introducing a time-dependent weighting factor. Such modifications of the objective function affect the optimization process and the resulting material parameters. Experimenting with the objective function also allows constitutive modeling scenarios in which one can explore the model's ability to capture specific features of the time-dependent response (by increasing its weighting coefficients), while observing the penalty of reduced fit to other features of the response.

2.3 Results

Using the proposed methodology, we demonstrate the modeling process and incrementally identify the simplest rheological configuration that captures the salient features of the time-dependent nonlinear response of an intact perfused *ex vivo* porcine liver undergoing large strain indentation. Whole porcine livers were freshly harvested and tested under near physiologic conditions (perfusate temperature 33°C, venous pressure 8 mmHg, arterial pressure 95 mmHg). The experimental boundary conditions include a flat plate beneath the liver with a 12 mm diameter flat cylindrical indenter on the top surface. The loading history of the indenter consists of a multiple load/unload ramps up to 40% nominal strain at rates from 1.8 to 360%/sec and a step response to 30% nominal strain (500%/sec instantaneous load held constant for 1200 seconds). The details regarding the experimental procedure and specimen variability may be found in Kerdok (2006) [69].

The characteristic features of the liver tissue (see Figure 2.3) include a prominent nonlinear elastic component, significant strain rate dependence, and long-scale

relaxation with a time constant on the order of 10 s. The generalized nominal stress-strain response was obtained from the experimentally measured force-displacement indentation response. The nominal strain was computed as a ratio of the indenter displacement ($d_{max} = 11.0 \text{ mm}$) and the local thickness of the organ ($h = 30.3 \text{ mm}$). The nominal stress was calculated by dividing the indenter reaction force ($F_{max} = 6.1 \text{ mN}$) by the cross-sectional area of the cylindrical indenter tip ($A = 1.131 \times 10^{-4} \text{ m}^2$). In this work we limit our focus on the characteristic features in the generalized time-dependent response and incrementally construct the required rheological configuration.

By examining the liver response, both in cyclic loading and in stress relaxation shown in Figure 2.3, we can observe that the tissue exhibits viscoelastic and rate-dependent behavior and also note the tissues tendency to relax to nonzero equilibrium stiffness. Considering this requirement of nonzero equilibrium back stress, we begin the model identification with a standard linear solid arrangement. This is the default arrangement of network 2. Using the bounded downhill simplex method to minimize the objective function $\Phi(p_n)$ (Eq. 5.27), defined as

$$\Phi(p_n) = \Phi_{LU}(p_n) + \Phi_{SR}(p_n), \quad (2.18)$$

where $\Phi_{LU}(p_n)$ evaluates the model fit to the cyclic load-unload block and $\Phi_{SR}(p_n)$ quantifies the model fit to the stress relaxation response. From the best model fit (shown in Figure 2.4) we can clearly appreciate the limitations of the standard linear solid model and conclude that a suitable constitutive model must include a nonlinear elastic component to account for the highly nonlinear instantaneous response commonly observed in collagenous tissues. See Table 2.3 for optimized material parameters and objective function values.

In the subsequent modeling iteration, we introduce an exponential elastic element in the 2A position with the intent to capture the instantaneous response of the tissue, while maintaining a linear viscous element in 2C and a linear elastic element in the 2B position to account for the long-time relaxation back stress. Such enhancement of the constitutive model increases the total parameter count to four, but the fitting results demonstrate significant improvement in the experimental agreement (see Figure 2.5). However, the model does not fully capture the stress relaxation of the material and underestimates the resistance to deformation at the lower displacement rates (slower hysteresis loops).

To further improve the model fit, we extend the viscous element 2C to a nonlinear power law formulation, to capture the nonlinear relationship between the driving stress and the viscous strain rate. In our experience, the power law relationship tends to overestimate the viscous deformation at high stresses. To take into account the limiting effect of the accumulated total viscous flow, we use a formulation that accommodates the limiting behavior with the reptation factor [14]. The configuration consisting of the SLS with exponential elastic element and reptation-limited nonlinear

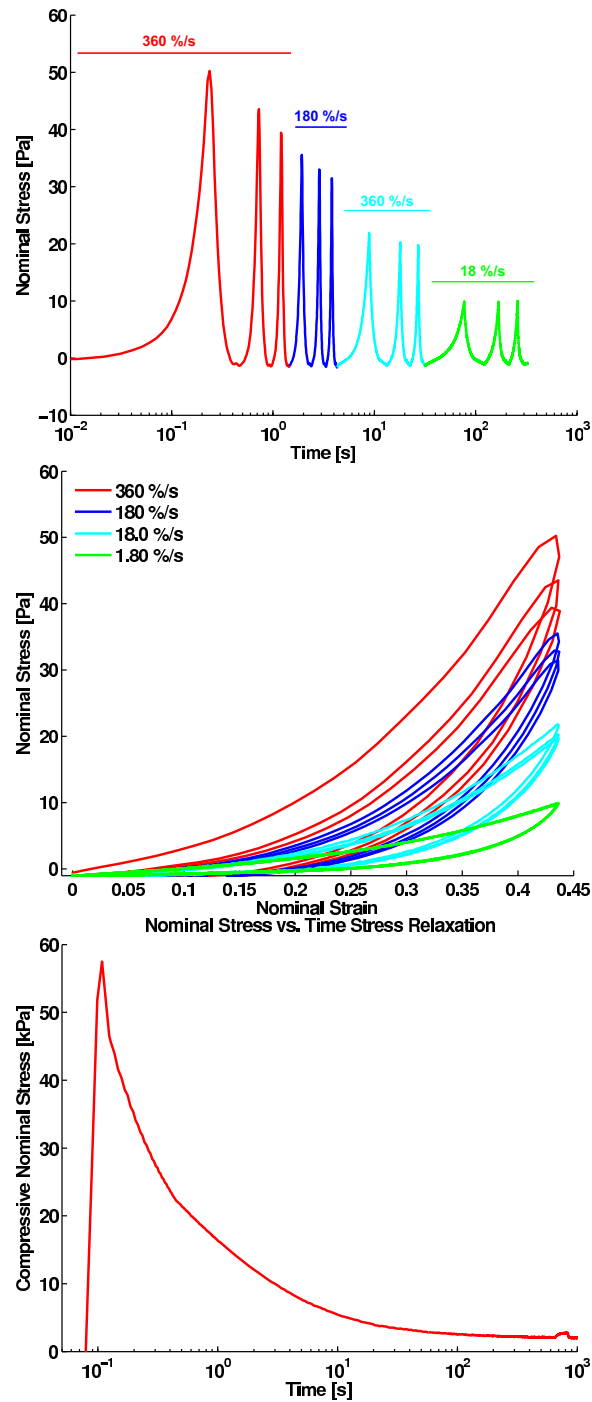


Figure 2.3: Indentation response of perfused porcine liver in indentation. A continuous segment of cyclic load/unload ramps is shown on the left. The corresponding stress-strain response is shown in the middle with individual displacement ramps distinguished by color. The stress relaxation response is shown on the right. All data was collected at the same location on the same liver specimen, allowing 30 minutes of recovery between the the cyclic tests and the stress relaxation.

viscosity has a total of 6 parameters and offers a good fit to the experimental data (see Figure 2.6). Considering the good agreement with the experimental data, this form of the constitutive material law may be considered an appropriate configuration in many applications. It optimizes the tradeoff between the number of material parameters and the goodness of fit to experimental data.

If some features of the model response are critical, such as the steady state in slow hysteresis loops necessary for surgical simulation, we may proceed to further increase the complexity of the rheological configuration. To capture the intermediate time scale as well as the long time scale relaxation response demonstrated in the data, we extend the configuration of network 2 with a time-dependent back stress in the form of another SLS configuration. This significantly more complex arrangement is the default configuration of network 3 and allows for incorporation of the long-time relaxation response through an additional time constant. The improvement comes at a cost of two additional parameters, however, and needs to be weighted in terms of its cost-benefit ratio. As we aim to improve the model agreement the experimental response from slow load/unload cycles, we expand the form of the objective function in a way that increases the significance of these features in the total objective score. We introduce an objective function with a time-dependent weighting coefficient vector $w[i]$ defined as

$$\Phi^*(p_n) = \Phi_{LU}^*(p_n) + \Phi_{SR}(p_n) \quad (2.19)$$

$$\Phi_{LU}^*(p_n) = \frac{1}{N} \sum_{i=1}^N w[i] (\sigma_{exp}[i] - \sigma_{model}[i])^2 \quad (2.20)$$

where $w[i] = 2.0$ for all i which include the 0.2 mm/s and 2.0 mm/s load-unload cycles and $w[i] = 1.0$ for all other indices. We may see in Figure 2.7 (middle) that the stricter enforcement of the model at slower load-unload cycles and the inclusion of the additional relaxation mechanism improves the model-experiment fit and the steady state in hysteresis loops at the slower rates. The material parameters of the discussed constitutive models and the associated objective function values are summarized in Table 2.3.

2.3.1 Applications to Other Tissues

The proposed modeling paradigm may be easily extended to other materials and tissues. In this section we demonstrate that the same rheological configuration developed in the previous section may be successfully applied to generalized response of brain tissue obtained in uniaxial compression. Upon examination of the brain tissue response, we may notice that it exhibits nonlinearity, rate-dependence, and long-term relaxation similar to the porcine liver discussed in previous sections. By fitting the

8 parameter formulation of network 3 developed for the liver, we obtain an excellent model-experiment fit, as shown in Figure 2.8.

Similarly, we extend the modeling methodology to an additional tissue type and mode of deformation. We show that cervical tissue in compression may be modeled within the proposed framework. In this case, however, the generalized time response only consists of experimental measurement of the stress relaxation and load/unload cycles at a single strain rate. Since no load/unload cycles at additional strain rates are considered, a simplified rheological configuration, comprising the network 2 configuration with reptation-limited power law viscous element, is capable of capturing the characteristic response and offers an excellent model experiment agreement (see Figure 2.9). The associated material parameters for the brain tissue and the cervical tissue in compression are summarized in Table 2.4.

2.4 Discussion and Conclusions

The goal of this chapter was to develop a constitutive modeling framework for rapid prototyping of constitutive material formulation, which simultaneously maximizes the agreement with observed experimental response and minimizes the number of required material parameters.

By discussing the material response within the simplified generalized nominal stress-strain response, we were able to simplify the complexity of the required models (removed the requirement of geometrical effects) and were able to focus our attention on the features of the time-dependent material response. While the material parameters identified within this study may not be true estimates of the parameters obtained from more rigorous inverse finite-element modeling, our approach provides the necessary means for exploration of the proper constitutive forms and the starting point for inverse FE modeling. Such approach offers an efficient and effective method for evaluating suitable rheological model configurations and assessing the cost-benefit ratio associated with introduction of constitutive elements of higher complexity (and higher parameter count). The desirability of this approach stems mostly from the ease of implementation of the constitutive laws during the prototyping period and the speed of execution. Based on our experience during the development of the liver constitutive model presented, typical ODE solutions of stress-strain history containing 12 consecutive liver indentations generally require less than 1 second of computational time on a standard personal computer.

In this study we also demonstrated the effect of objective function choice on the final model fit. By increasing the relative weight of the model response history containing specific features of interest, we demonstrated that the objective function formulation may be used to finely adjust the desirable/important features of the model-experiment fit. Such experimentation and fine adjustment of the objective function definition is made feasible by the computational efficiency of the one-dimensional

numerical simulation and further illustrates the utility of this approach in the early stages of constitutive modeling of time-dependent tissue response.

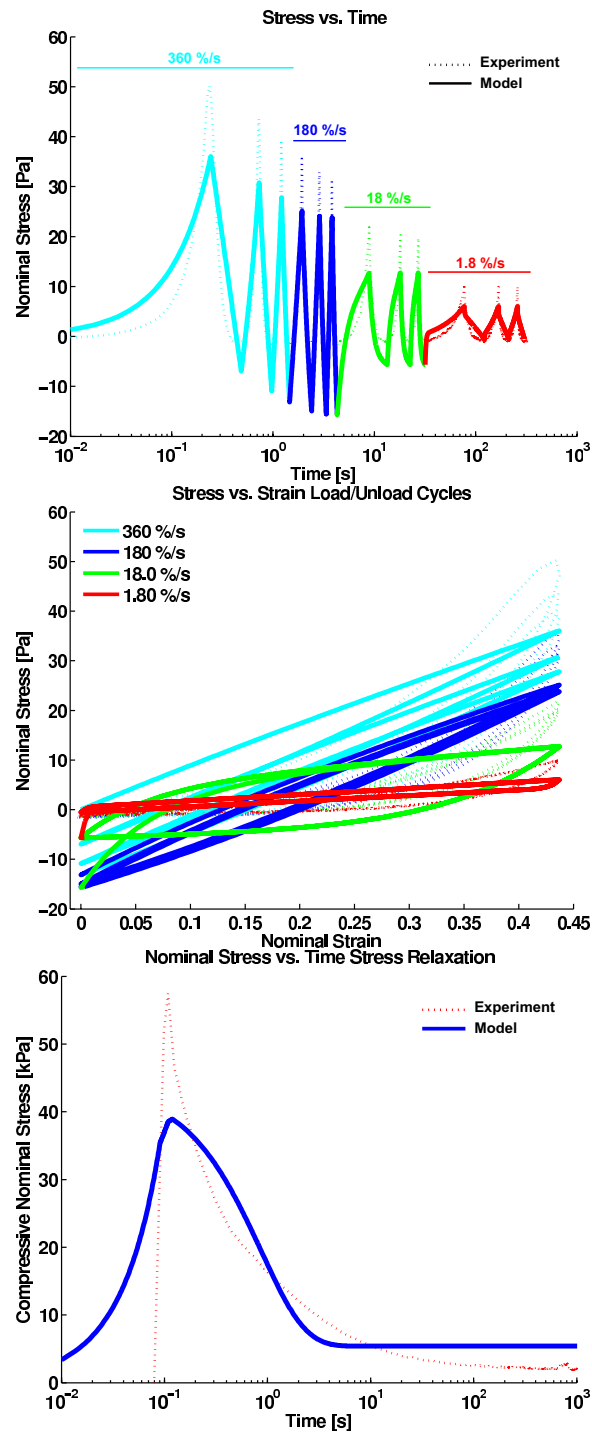


Figure 2.4: . Configuration 1 (3 material parameters): linear elastic element in 2A, linear back stress elastic element (2B), and a linear dashpot (2C). Material parameters shown in Table 2.3.

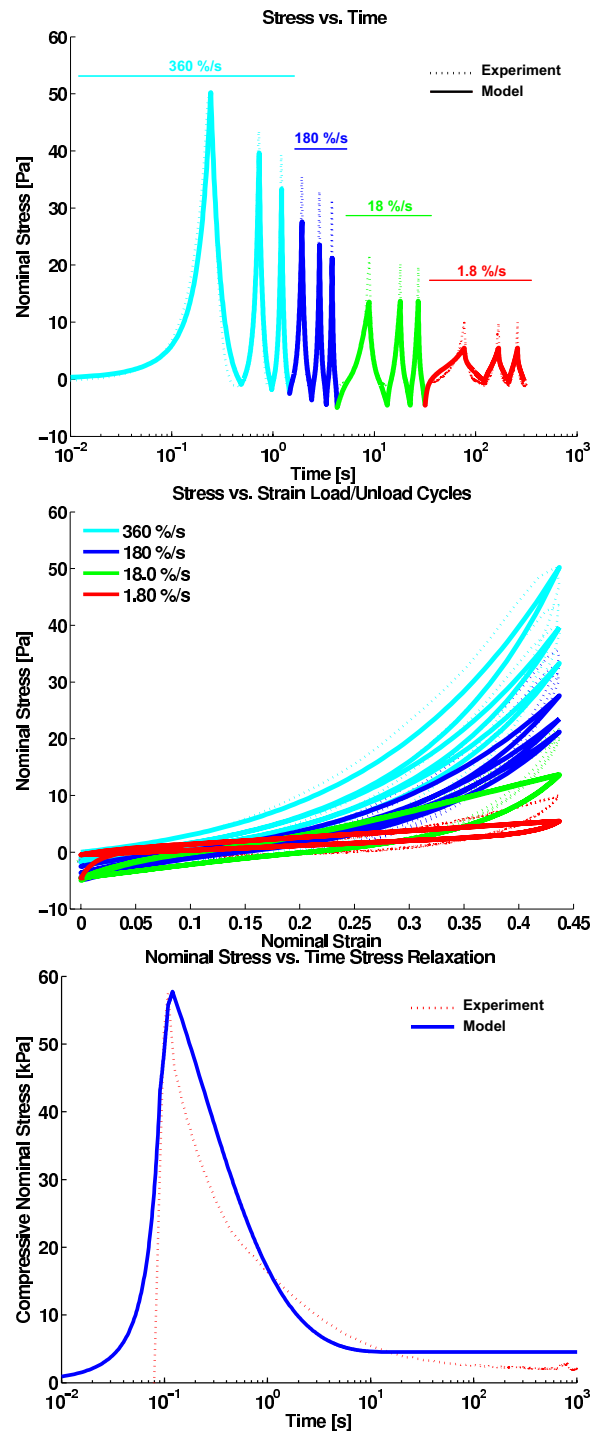


Figure 2.5: . Configuration 2 (4 material parameters): exponential elastic element in 2A, linear back stress elastic element (2B), and a linear dashpot (2C). Material parameters shown in Table 2.3.

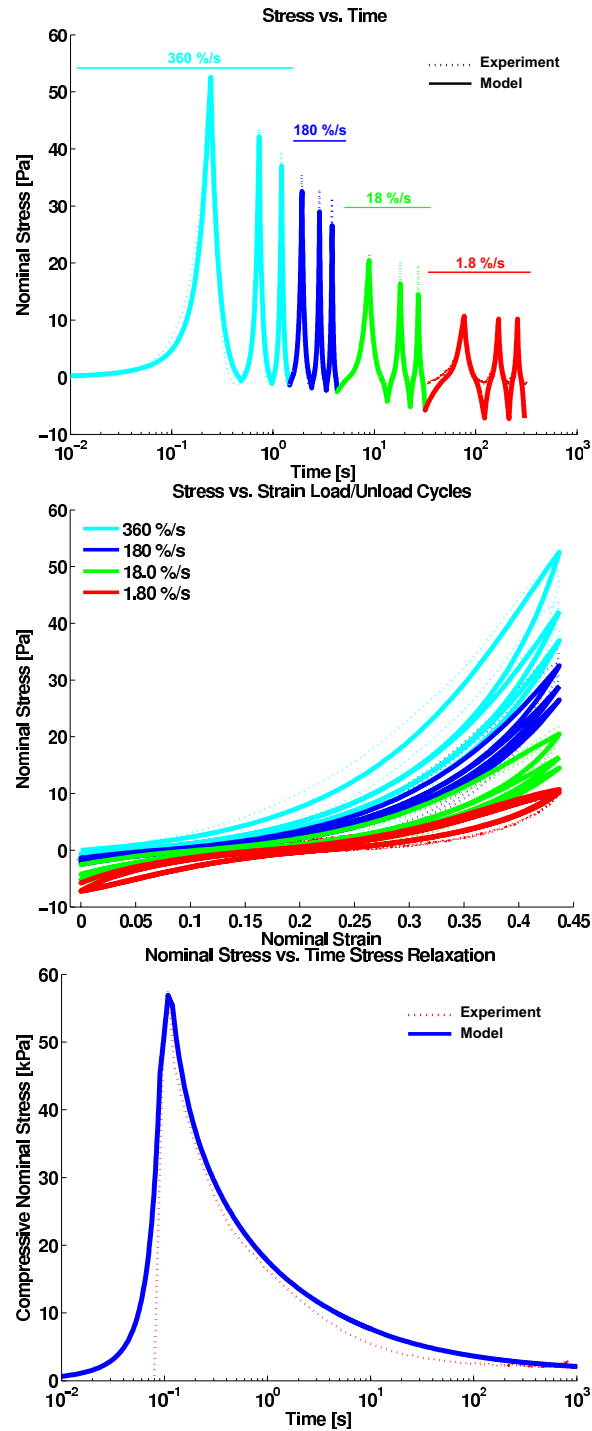


Figure 2.6: . Configuration 3 (6 material parameters): exponential elastic element in 2A, linear back stress elastic element (2B), nonlinear viscous power law dashpot with reptation-limited flow (2C). Material parameters shown in Table 2.3.

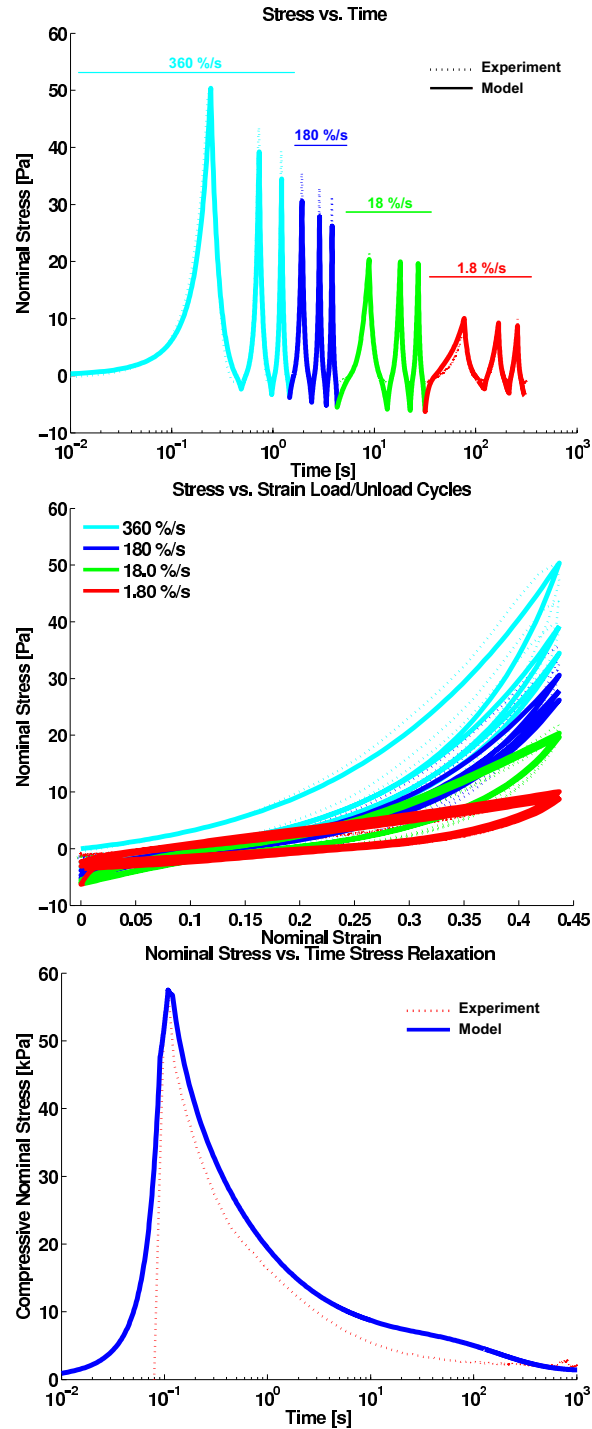


Figure 2.7: . Configuration 4 (8 material parameters): exponential elastic element in 3A, nonlinear viscous power law dashpot with reptation-limited flow (3C), and time-dependent back stress in SLS arrangement (3B,3D,3E). Material parameters shown in Table 2.3.

Table 2.3: Material parameters and the associated objective function for perfused porcine liver. (* denotes the alternative form of Φ defined in equation 2.19)

| Configuration | Element A | Element B | Element C | Element D | Element E | Φ |
|----------------------|-----------------------------|------------------|---|------------------|--------------------|--------------------------|
| Network 2 (SLS) | $E = 91.9Pa$ | $E = 13.7Pa$ | $\eta = 91.4Pa.s$ | - | - | 75.45 |
| Network 2 | $A = 21.17Pa$ $b = 6.85$ | $E = 14.1Pa$ | $\eta = 150.7Pa.s$ | - | - | 29.49 |
| Network 2 | $A = 14.81Pa$ $b = 8.23$ | $E = 3.46Pa$ | $S_0 = 53.16Pa$ $n = 2.7$ $\alpha = 0.45$ | - | - | 22.82 |
| Network 3 | $A = 21.12Pa$ $b = 8.0$ | $E = 24.81Pa$ | $S_0 = 12.9Pa$ $n = 1.44$ $\alpha = 0.0072$ | $E = 3.72Pa$ | $\eta = 3,505Pa.s$ | 27.98* |

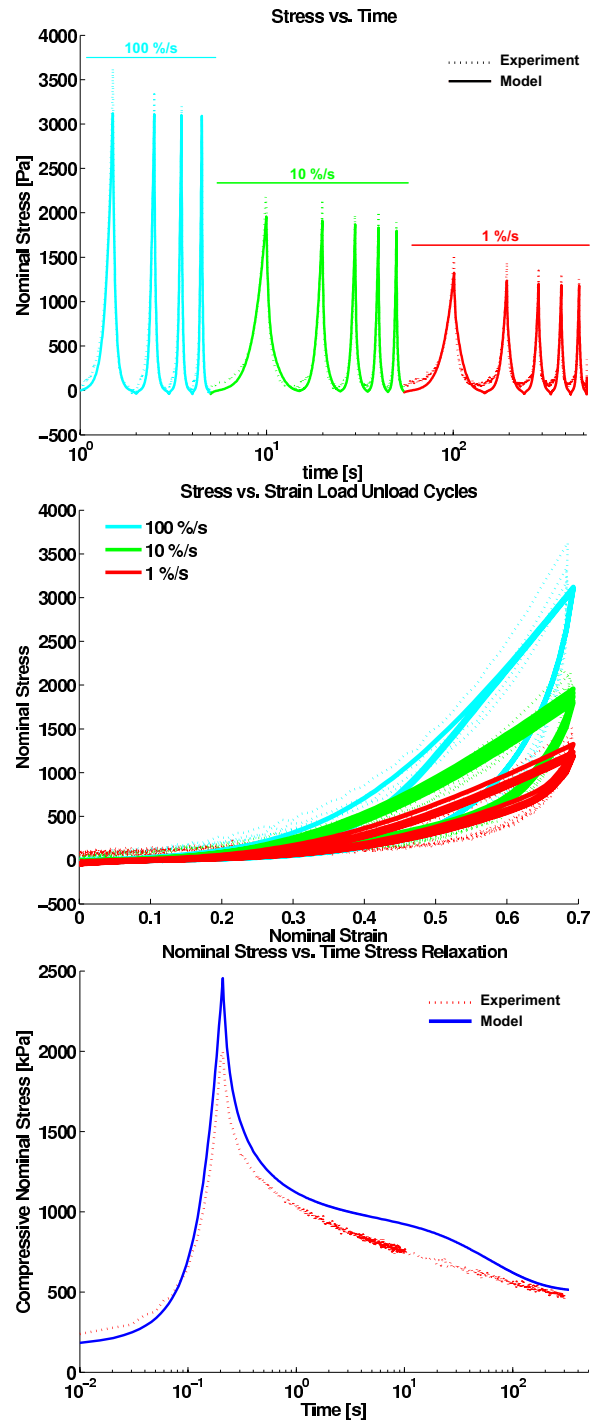


Figure 2.8: . Brain tissue in compression (8 material parameters): exponential elastic element in 3A, nonlinear viscous power law dashpot with reptation-limited flow (3C), and time-dependent back stress in SLS arrangement (3B, 3D, 3E). Material parameters shown in Table 2.4.

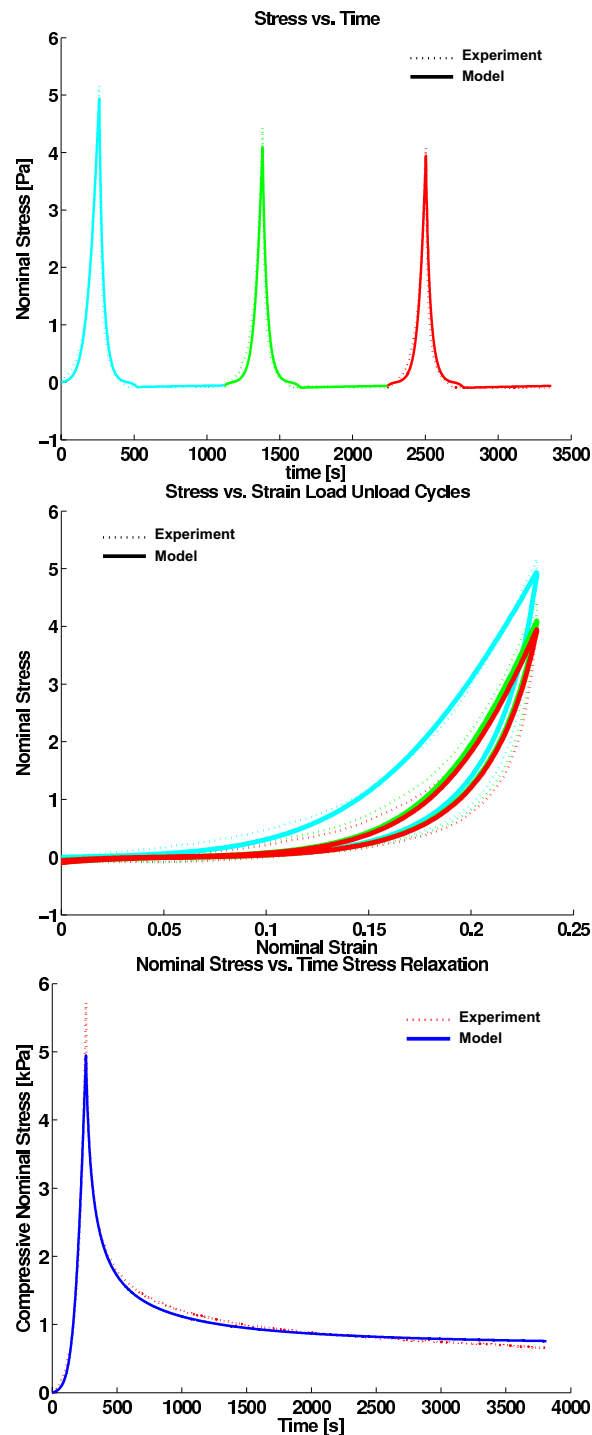


Figure 2.9: . Cervical tissue in compression 3 (6 material parameters): exponential elastic element in 2A, linear back stress elastic element (2B), nonlinear viscous power law dashpot with reptation-limited flow (2C). Material parameters shown in Table 2.4.

Table 2.4: Model fits to brain tissue and cervical tissue in compression: material parameters and the associated objective function values.

| Tissue Sample | Element A | Element B | Element C | Element D | Element E | Φ |
|--------------------|-------------------------------|---------------|--|---------------|----------------------|--------|
| Cervix (Network 2) | $A = 514.53Pa$ $b = 31.47$ | $E = 6.08kPa$ | $S_0 = 29.56kPa$ $n = 1.35$ $\alpha = 0.00033$ | - | - | 0.0242 |
| Brain (Network 3) | $A = 196.80Pa$ $b = 9.84$ | $E = 5.55kPa$ | $S_0 = 74.76kPa$ $n = 2.01$ $\alpha = 0.00029$ | $E = 1.91kPa$ | $\eta = 322.91kPa.s$ | 0.0121 |

Chapter 3

Estimating Experimental Tissue Deformation

3.1 Introduction

Mechanically accurate nonrigid registration of volumetric medical image data is an increasingly important aspect of guiding surgical procedures involving deformations of solid organs. Image-guided tasks, such as MRI tumor localization during brain shift, needle biopsy, prostate brachytherapy and others require a close interplay of computational biomechanical models with preoperative and intra-operative imaging. Soft tissue procedures often involve large strains, instrument-tissue contact, and fracture (i.e. cutting) of tissues. This necessitates the use of sophisticated mechanical modeling techniques that far exceed the capabilities of the custom-written linear finite element models typically used for these applications. Complex constitutive laws that accurately capture the large-strain, viscoelastic, and highly nonlinear response of soft tissue are also required. These materials models must then be validated and parameterized by experimental testing protocols appropriate for unique identification of the material constants. Additionally, the observed patient-to-patient mechanical variability of soft tissues requires patient-specific (personalized) models, which must be generated and parameterized with clinically feasible testing protocols.

A wide array of methods has been presented for mechanically constrained non-rigid registration of brain deformations, cardiac motion, breast deformation during mammography, as well as applications for prostate and other organ systems. In general, these methods are limited to linear elastic and, in some cases, relatively simple nonlinear and viscoelastic material constitutive laws. At the moment, the use of state-of-the-art biomechanical organ models in nonrigid image registration is hindered by the requirement of custom finite-element solvers, mandated by the inherent coupling between the image-domain components of the algorithm and the biomechanical computational methods.

In this chapter we present a nonrigid image registration framework for 3D ultrasound, and demonstrate its applicability to soft tissue material parameter identification. The registration algorithm uses a mechanical finite-element model as a regularizer of the estimated deformation field. By coupling image-based motion estimates to a mechanical model through springs connected at the nodal locations, the image-based deformation estimation process is partitioned from the mechanical model. This contrasts with most current mechanical regularization schemes, where the image information is directly incorporated into the mechanical model solver. The proposed approach thus permits the use of sophisticated off-the-shelf mechanical modeling software that incorporates nonlinearities and complex material properties. This method therefore promises greatest benefit in applications with large-deformation tissue interactions and complex constitutive models.

The proposed registration technique is particularly advantageous for image-based material property estimation. Traditionally, solid nonload-bearing organs (e.g. liver, spleen, kidney, brain) are characterized using one-dimensional force versus displacement information gathered from a single mode of deformation (e.g. indentation, rotational shear, grasping, aspiration). Due to simplicity of the tool, low risk of injury, and the necessity to measure material properties *in vivo*, as *in vitro* measurements often differ significantly [48, 91, 93, 53, 90, 71], indentation is the most popular method for solid organ testing. The single force-displacement history obtained during an indentation experiment provides only limited information about tissue mechanics. For example, it combines the mechanical response of the whole material domain, including near-field (large strain) and far-field (low strain) contributions, and it fails to distinguish much of the information related to the interplay between shear and bulk compliance in the complex deformation field beneath the indenter. Therefore, supplemental experimental methods, such as secondary indentation sensors [11], tissue surface tracking [41, 42], or independent tests of bulk compliance (i.e. in-vitro confined tissue compression) are necessary for well-conditioned parameter identification. Image-based methods can address these limitations by measuring the deformation field throughout an entire volume of the tissue as it is deformed, separating inhomogeneous regions, differentiating areas of large and small strain, and permitting direct measurement of volumetric changes.

3.2 Relation to Existing Work

Relating Linear Elastic Mechanical Regularization to Horn & Schunck Optical Flow

The traditional differential optical flow techniques, such as Horn and Schunck [61] and Lucas-Kanade [84] rely on two fundamental assumptions: frame-to-frame intensity constancy and local intensity gradient constancy. Under these assumptions the motion of each voxel may be expressed by the optical flow constraint equation

$$\frac{\partial I}{\partial x}u_x + \frac{\partial I}{\partial y}u_y + \frac{\partial I}{\partial z}u_z + \frac{\partial I}{\partial t} = 0, \quad (3.1)$$

where $I(x, y, z, t)$ is the voxel intensity and $\{u_x, u_y, u_z\}$ are vector components of the corresponding voxel motion. Detailed performance and accuracy evaluation of the commonly used optical flow techniques can be found in Barron et al. [13].

Since enforcement of the optical flow constraint (Eq. 3.1) at each image voxel results in an under-constrained system of linear equations, further regularization is required to make the problem well-posed. The available regularization techniques range from homogeneous first-order smoothing to formulations reflecting true material mechanics. Tikhonov-like regularizers, such as the original Horn & Schunck algorithm, are at the core of most image-driven approaches, including recent variational methods [102]. A thorough summary of image-driven regularization operators is provided by Weickert and Schnörr [128]. In the following sections, we will demonstrate that mechanical regularization provides a general, physically realistic, regularization framework and, under certain conditions, can be related to the common image-driven regularization operators.

Image-Driven Regularizers The traditional optical flow technique formulated by Horn and Schunck regularizes the solution by enforcing a first-order smoothness of the resulting displacement field, minimizing the functional

$$\Psi(\mathbf{u}_x, \mathbf{u}_y, \mathbf{u}_z) = \int \int \int (E_f + \alpha^2 E_s) dx dy dz. \quad (3.2)$$

While the E_f term is the deviation from the optical flow constraint (Eq. 3.12), Horn and Schunck propose two different definitions of the smoothness constraint E_s . The more widely used (and the one carried through in the original paper) is

$$E_s = \sum_k \left(\frac{\partial \mathbf{u}_x}{\partial k} \right)^2 + \sum_k \left(\frac{\partial \mathbf{u}_y}{\partial k} \right)^2 + \sum_k \left(\frac{\partial \mathbf{u}_z}{\partial k} \right)^2, \quad (3.3)$$

where $k = \{x, y, z\}$. The second formulation of the smoothness constraint,

$$E_s = (\nabla^2 \mathbf{u}_x)^2 + (\nabla^2 \mathbf{u}_y)^2 + (\nabla^2 \mathbf{u}_z)^2, \quad (3.4)$$

is more interesting because it enforces Laplacian smoothness and can be closely related to a continuum mechanics interpretation. As \mathbf{u}_x , \mathbf{u}_y , and \mathbf{u}_z are vector components of displacement field \mathbf{u} , minimization of $\alpha^2 (\nabla^2 \mathbf{u})^2 + E_f$ is analogous to the solution of Poisson's equation ($\nabla^2 \mathbf{u}(x, y, z) - \mathbf{F}(x, y, z) = 0$) over the image domain.

In contrast, for local optical flow techniques, such as the Lucas-Kanade or the Singh [115] methods, the smoothness constraint cannot be explicitly related to mechanical regularization. Since these methods rely on local assumptions of smoothness

(either constant or affine transformation within local neighborhood), the only parameter that determines the deformation field smoothness is the size of the local neighborhood. In implementations where the local neighborhood is sampled by Gaussian weighting functions, the standard deviation of the sampling kernel may be considered as a measure of smoothness.

Linear Elastic Regularizer A general, physically motivated, regularization approach can be derived from the fundamental field equations formulated by the theory of continuum mechanics. In general, static problems in three-dimensional linear, isotropic elasticity require the solution of 15 scalar fields that satisfy 15 field equations. These field equations consist of 6 strain-displacement equations (Eq. 3.5), 3 equilibrium equations (Eq. 3.6), and 6 constitutive law equations (Eq. 3.7),

$$\boldsymbol{\epsilon} = \frac{1}{2}(\nabla \mathbf{u} + (\nabla \mathbf{u})^T), \quad (3.5)$$

$$\nabla \cdot \boldsymbol{\sigma}^T + \mathbf{f} = 0, \quad (3.6)$$

$$\boldsymbol{\sigma} = 2\mu\boldsymbol{\epsilon} + \lambda(\text{tr } \boldsymbol{\epsilon})\mathbf{I}, \quad (3.7)$$

where \mathbf{u} is the displacement vector field, $\boldsymbol{\epsilon}$ is the strain tensor field, $\boldsymbol{\sigma}$ is the stress tensor field, μ and λ are the Lamé material constants, and \mathbf{f} is the field of body force per unit volume.

The field equations of linearized elasticity can be combined in various ways to eliminate unknowns and thus arrive at forms of the field equations, involving a reduced number of equations and unknowns. The problem of finding solutions to the equations of elasticity can be restated in terms of either finding a displacement field \mathbf{u} that satisfies the Lamé-Navier equations or finding a stress field $\boldsymbol{\sigma}$ that satisfies the equations of equilibrium and the Beltrami-Michell compatibility equations [117]. The Lamé-Navier equations may be written as

$$(\lambda + \mu)\nabla(\nabla \cdot \mathbf{u}) + \mu\nabla^2\mathbf{u} + \mathbf{f} = 0. \quad (3.8)$$

The Lamé constants may be related to a material's Young's modulus E and Poisson's ratio ν as $\lambda = \frac{E\nu}{(1+\nu)(1-2\nu)}$ and $\mu = \frac{E}{2(1+\nu)}$. Rewriting the Lamé-Navier equations in terms of E and ν results in

$$\frac{E}{(1+\nu)(1-2\nu)}\nabla(\nabla \cdot \mathbf{u}) + \frac{E}{2(1+\nu)}\nabla^2\mathbf{u} + \mathbf{f} = 0. \quad (3.9)$$

It is important to note that boundary conditions may only be stated in terms of displacements in this formulation and, therefore, the deformation field \mathbf{u} is governed by its boundary values (if specified) and the imposed body force \mathbf{f} .

Under the assumption of an incompressible material ($\nu = \frac{1}{2}$ and $\nabla \cdot \mathbf{u} = 0$), the Lamé-Navier equations reduce to the Poisson's equation

$$\frac{E}{3}\nabla^2\mathbf{u} + \mathbf{f} = 0. \quad (3.10)$$

Therefore, the Laplacian-smooth regularization suggested by Horn and Schunck (Eq. 3.4) is closely related to mechanical regularization with an assumption of incompressible linear isotropic (independent of direction) material. This observation is of interest in light of recent publications [105, 18] suggesting the importance of the incompressibility constraints for nonrigid registration of certain tissues, such as the myocardium and the breast.

3.2.1 Nonrigid Image Registration Algorithms

The success of image-based mechanical characterization methods is dependent on an accurate and robust estimation of visual motion. Estimation of volumetric tissue deformation during indentation experiments may be posed as a nonrigid registration problem. Nonrigid registration methods may be broadly classified by their formulation of the image correspondence constraint as being geometric (feature-based) or iconic (intensity-based). While geometric techniques rely on locally estimated motion of sparse features or anatomical landmarks, iconic methods estimate transformations which maximize image similarity across the full image domain. For this reason iconic methods are closely related to traditional optical flow methods, such as the Horn and Schunck (1981) [61] and Lucas and Kanade (1981) [84] algorithms. While there is an extensive body of prior work on nonrigid registration, including recent methods specific to 3D ultrasound [78, 47, 80, 83], this chapter addresses the area of regularization and image-mechanics coupling, which will be the focus of the following literature review. This approach of using physically realistic constraints has demonstrated the ability to provide accurate deformations in many applications, including pre-operative to intra-operative brain shift [21, 28, 32, 55, 75, 44, 104, 116, 29], intra-operative liver deformation [26], anatomical atlas brain registration [9], cardiac cycle [101, 113], breast deformation during mammography [111, 110, 106], prostate deformation during brachytherapy [40, 5], as well as muscular tissue deformation [134].

The nonrigid registration problem can be posed either as an interpolation or an approximation problem. When mechanics are used as an interpolator, a sparse set of volumetric or surface motion estimates (usually processed by an outlier-rejection scheme) is used as a boundary condition constraint and the dense deformation field is recovered by solving the mechanical finite-element model. The methods of Miga et al. (2003) [87] and Audette et al. (2003) [8] rely on mechanical finite-element models as interpolators of cortical surface motion obtained from laser range scanners in order to obtain the displacement of deeper cortical structures. Skinjar et al. (2002) [116]

and Sun et al. (2003) [120] used a similar approach by tracking the cortical surface with stereo vision systems.

When the nonrigid registration is posed as an approximation problem, the dense deformation field is obtained by minimizing an energy functional consisting of an image-similarity term and a mechanical regularization term. Yeung et al. (1998) [134] used a deforming 2D mesh constrained by a plane-strain linear elastic model to regularize motion of sparsely estimated textural speckle features. Hata et al. (1998) [56] used linear elastic energy as a regularization of locally estimated motion based on mutual information between preoperative and intra-operative images of the brain. Papademetris et al. (2002) [101] used a sophisticated nonlinear finite-element model of the beating heart, which was precomputed offline and subsequently used in a Bayesian blending framework with sparsely estimated motion vectors from ultrasound to obtain mechanically regularized motion estimates. Ferrant et al. (2001) [44] and Rexilius et al. (2001) [104] perform elastic matching of preoperative and intra-operative brain shift images using a finite-element regularization scheme minimizing the functional

$$E = \int_{\Omega} \boldsymbol{\sigma}^t \boldsymbol{\epsilon} d\Omega + \int_{\Omega} (I_1(x + u(x)) - I_2(x))^2 d\Omega, \quad (3.11)$$

where the first term is the elastic strain energy term ($\boldsymbol{\epsilon}$ is the strain tensor and $\boldsymbol{\sigma}$ is the stress tensor) and the second term is the sum of squared differences between a warped reference image I_1 and subsequent image I_2 over the image domain Ω . This image-mechanics coupling mechanism is an appealing regularization scheme, as it is analogous to the Tikhonov regularization methods in optical flow [61, 102] and allows the final solution to be computed through the finite-element method. The relationship between mechanical regularization methods and optical flow regularization was addressed in further detail in the previous sections. One of the shortcomings of this method is the fact that the mechanical model is deformed by an image force (dependent on the chosen regularization parameter), rather than the true mechanical boundary conditions and applied external forces. Unless boundary conditions associated with the mechanical model are specified, methods based on minimization of data and elastic energy terms result in underestimation of the true deformation field. This can be explained by the fact that the elastic term forces solutions towards the minimal elastic energy of the body, which, in the absence of boundary conditions and external loads, corresponds to zero displacement throughout the body. Clatz et al. (2005) [29] addressed this limitation by proposing and demonstrating the convergence of a minimization approach, which evolves the deformation field from an approximation to an interpolation solution, minimizing the least square error of an image-similarity term along with an iterative outlier rejection scheme.

All of the discussed techniques exploit the knowledge of material properties (and boundary conditions in some cases) to provide better estimates of underlying motion. The scope of the physics-based regularizers is generally limited to a specific choice of constitutive mechanical behavior. With the ongoing progress in mechanical

characterization of biological tissues beyond the standard linear viscoelastic models, regularizers capable of incorporating nonlinear material mechanics are needed. Creating appropriate regularizers specific to tissue type and fundamental mechanical behavior, however, is difficult due to the complexity of the underlying mechanics and the need for custom finite-element solvers.

3.2.2 Framework for Image-Mechanics Coupling

To solve this problem, this work presents a general framework for the solution of volumetric motion estimation under nonlinear continuum mechanics constraints. In this framework, the model geometry, boundary conditions, and material behavior can be modified independently, which provides the ability to include state-of-the-art material constitutive models used in the solid mechanics, material science, and biomechanics communities. This is accomplished by leveraging existing finite element solvers and by coupling image intensity information to a finite element model in a natural way. The only parameter of the resulting system is a single scalar value that balances the contribution of the intensity data and the mechanics of the material. We enforce image-driven local motion estimates as concentrated forces applied at mesh nodes of an underlying mechanical model. The concentrated forces are generated by regularization springs, connected to the mesh nodes, when their free ends are displaced according to local motion estimates. The choice of each regularization spring stiffness reflects local textural quality and associated local motion confidence. Due to the image-mechanics coupling through concentrated forces applied throughout the interior of the body, solution of the mechanics problem does not require complete knowledge of boundary conditions.

One of the key benefits of this approach is the flexibility in choosing individual components. Because the image-based deformations are coupled as spring forces, the approach allows the use of any mechanics package. This is particularly advantageous for complex mechanical interactions, where sophisticated modeling packages from mechanics research groups or commercial enterprises can accurately model such nonlinearities as large deformations, contact problems, and fracture. This avoids the substantial burden of developing custom mechanical modeling code, which for these situations is a far greater challenge than development of the linear solvers that have been traditionally used in image-driven regularization. This modularity also enables selecting mechanics packages that are best suited for each tissue type without the necessity of altering other components of the system. In terms of mechanics, not only can any material constitutive law be used, but also any (potential) knowledge of boundary conditions can be directly incorporated.

For determining deformation fields from images, the image similarity measure, local matching algorithm, and motion confidence metric can each be independently and intuitively controlled. The method is formulated as an iconic (intensity-based) approach, however it combines the benefits of feature-based methods by assigning

texture/feature dependent confidence values to local motion estimates. Additionally, it does not require explicit computation of the nodal deformation forces. The deformation forces are handled implicitly by the displaced ends of regularization springs in the mechanical finite-element model. This technique is suitable for large-deformation tracking not only because of the finite-deformation formulation of the finite-element method, but also due to the fact that the stress state is propagated from frame to frame by the mechanical model. This approach helps to eliminate multi-frame accumulation of error and also provides proper mechanical response over time for time/rate dependent viscoelastic materials, unlike memoryless mechanical regularizers.

Additionally, the regularization energy corresponding to the potential energy stored in regularization springs is minimized when the mechanical response of the regularization model matches the mechanical response of the organ. We demonstrate that this property can be used to identify the material parameters of the deforming tissue through an iterative minimization scheme. Therefore, the general mechanical regularization framework presented in this chapter is suitable for both classical nonrigid image registration problems and for image-based identification of material parameters.

The remainder of this chapter is organized as follows. We present the algorithm and general methodology in Section III. Quantitative motion estimation evaluations on synthetic and experimentally obtained 3D ultrasound sequences, including performance analysis under noise, are presented and discussed in Section IV. Additionally, Section IV includes an example application of this method to parameter identification of a nonlinear poroelastic liver model, using a synthetically generated ground-truth 3D ultrasound indentation sequence. The benefits and implications of this work are discussed in Section V. Finally, we address the relationship between linear elastic regularization methods and image-based optical flow regularization schemes in the appendix.

3.3 Methodology

3.3.1 Mechanical Regularization Framework

Our general regularization framework (Fig. 4.3) links local image motion to a mechanical model to provide a global and mechanically accurate dense motion field. We propose to deform a mechanical model by applying concentrated forces, at nodal locations, which can be interpreted as lumped values for a corresponding body force field \mathbf{f} . Three regularization springs attached to each node of the model apply body forces in the three orthogonal coordinate directions. The free-end regularization springs displacements \mathbf{u}^{OF} are obtained from a local motion estimate, which is derived, in our implementation, from the Lucas-Kanade optical flow method. The spring stiffness is adjusted to reflect local nodal stiffness of the mechanical model and the motion

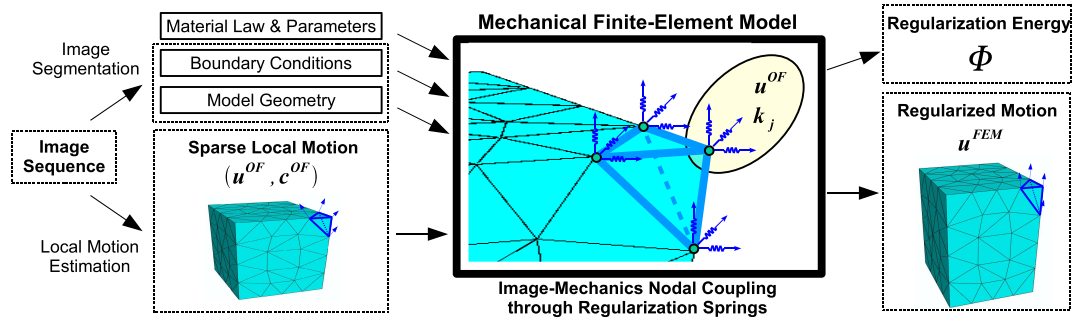


Figure 3.1: In the proposed mechanical regularization framework, sparse local motion estimates are coupled to a mechanical finite-element model as lumped body forces applied by displaced regularization springs. This results in a mechanically constrained deformation field \mathbf{u}^{FEM} and regularization energy Φ .

estimate confidence \mathbf{c}^{OF} , which reflects the textural content in the neighborhood. The choice of mapping between local motion and spring stiffness is discussed in detail in the following sections. The mechanically regularized optical flow \mathbf{u}^{FEM} is the displacement field obtained from the solution of the mechanically deformed finite-element model. Finally, dense motion fields providing per-voxel displacements \mathbf{u} can be obtained by interpolation of the nodal displacements \mathbf{u}^{FEM} with the model's elemental shape functions.

3.3.2 Meshing

Meshing is an important component of the regularization algorithm. There is a vast array of literature regarding optimal meshing methods, given the required

```

Input: 3DUS sequence, mechanical FEM model & material parameters,
         regularization coefficient
Output: Volumetric displacement field, regularization energy  $\Phi$ 

Register 3DUS and FEM coordinate systems;
foreach 3DUS frame at time  $t_{current}$  do
  Compute spatio-temporal image derivatives;
  foreach FEM mesh node do
    // local image motion estimation
    Estimate local motion (modified Lucas-Kanade approach);
    Estimate local motion confidence (textural quality);
    // image-mechanics coupling
    Compute regularization springs stiffness and displacement;
    Connect regularization springs & update spring end displacement;
  end
  Solve FEM for  $t = t_{current}..(t_{current} + dt)$ ;
end
Interpolate nodal displacements to obtain a per-voxel displacement field;

```

Figure 3.2: Algorithmic description of the registration framework.

application. In some cases, meshes and nodal locations are optimized based on textural properties [134], to maintain nodal locations corresponding to prominent texture features. Such texture-driven mesh density may be optimal for local image motion estimation, but in our application the mechanical aspects must be considered.

In mechanical modeling, the mesh density and biasing are generally a function of the expected deformation and stress field distribution. For this reason, we follow the approach of generating meshes which are primarily intended for the mechanical model. The use of texture-quality dependent regularization springs mostly alleviates the need for nodal location dependence on textural features. Therefore, our method is an appealing solution to the meshing problem, considering both the computational mechanics as well as local image motion estimation requirements.

3.3.3 Local Optical Flow Estimation

In this modular architecture, any algorithm can be used to estimate the local optical flow \mathbf{u}^{OF} . As an example, we use a modified Lucas-Kanade algorithm. The traditional differential optical flow techniques, such as the Lucas-Kanade method, rely on two fundamental assumptions: frame-to-frame intensity constancy and local intensity gradient constancy. Under these assumptions the motion of each voxel is constrained by the optical flow equation

$$\frac{\partial I}{\partial x}u_x + \frac{\partial I}{\partial y}u_y + \frac{\partial I}{\partial z}u_z + \frac{\partial I}{\partial t} = 0, \quad (3.12)$$

where $I(x, y, z, t)$ is the voxel intensity and $\{u_x, u_y, u_z\}$ are vector components of the voxel velocity. Since the optical flow constraint for a single voxel is ill-posed, the solution of the Lucas-Kanade algorithm relies on additional motion assumptions within the local neighborhood. In our case we sample the neighborhood of each mesh node (all neighboring tetrahedra) and assemble a system of equations

$$N_i \frac{\partial I_i}{\partial x} u_x^{OF} + N_i \frac{\partial I_i}{\partial y} u_y^{OF} + N_i \frac{\partial I_i}{\partial z} u_z^{OF} = -N_i \frac{\partial I_i}{\partial t} \quad (3.13)$$

weighted by the linear tetrahedral shape functions (see e.g. Zienkiewicz (1977) [136] for details) defined as

$$N_i = \frac{1}{6V} (a_i + b_i x_i + c_i y_i + d_i z_i), \quad (3.14)$$

where

$$6V = \det \begin{bmatrix} 1 & x_k & y_k & z_k \\ 1 & x_l & y_l & z_l \\ 1 & x_m & y_m & z_m \\ 1 & x_n & y_n & z_n \end{bmatrix} \quad (3.15)$$

$$a_i = \det \begin{bmatrix} x_l & y_l & z_l \\ x_m & y_m & z_m \\ x_n & y_n & z_n \end{bmatrix} \quad (3.16)$$

$$b_i = \det \begin{bmatrix} 1 & y_l & z_l \\ 1 & y_m & z_m \\ 1 & y_n & z_n \end{bmatrix} \quad (3.17)$$

$$c_i = \det \begin{bmatrix} x_l & 1 & z_l \\ x_m & 1 & z_m \\ x_n & 1 & z_n \end{bmatrix} \quad (3.18)$$

$$d_i = \det \begin{bmatrix} x_l & y_l & 1 \\ x_m & y_m & 1 \\ x_n & y_n & 1 \end{bmatrix} \quad (3.19)$$

are defined in terms of the coordinates $\{x_i, y_i, z_i\}$ of the voxel i and the coordinates of the vertices of the tetrahedron $klmn$.

Using the linear tetrahedral shape function as the nodal neighborhood weighting functions, the local system of optical flow equations can be rewritten as

$$\mathbf{A}u^{OF} = \mathbf{b}, \quad \mathbf{A}_{ij} = N_i \frac{\partial I_i}{\partial j}, \quad \mathbf{b}_i = -N_i \frac{\partial I_i}{\partial t}, \quad (3.20)$$

where i is the voxel index and $j = \{x, y, z\}$. The nodal displacement can be recovered as the least-squares solution to this linear system. Local motion \mathbf{u}^{OF} is computed at each mesh node, providing a globally unconstrained set of local motion estimates. Each nodal motion estimate has an associated confidence \mathbf{c}^{OF} . Traditionally, this confidence is computed from the three eigenvectors (direction of confidence) and eigenvalues (level of confidence) of the square $\mathbf{A}^T \mathbf{A}$ matrix. However, to account for the variability of local neighborhood size throughout the mesh, we follow an alternative approach in which we compute the texture-dependent confidence by summing the absolute values of image gradients in the nodal neighborhood, such that

$$c_j^{OF} = \sum_{i=1}^n N_i \left| \frac{\partial I_i}{\partial j} \right|, \quad (3.21)$$

where $i = \{1, \dots, n\}$ are all voxels contained in elements surrounding the node of interest and $j = \{x, y, z\}$. The value of c_j^{OF} is subsequently normalized by the largest value contained in the image volume, such that $c_j^{OF} \in [0, 1]$.

3.3.4 Mechanically Regularized Deformation

Once the local motion estimates and the associated confidence levels are computed, the mechanical model is deformed by the forces applied through regularization springs with one end attached to the nodes of the mechanical mesh, and one end constrained to match the displacement corresponding to local image motion. To provide a conceptual interpretation of this registration approach, the deformation of a simple one-dimensional continuum mechanics model (beam) is described in Fig. 3.3. We address two types of problems: the class of problems where boundary conditions are unknown (shown in Fig. 3.3, left) and well-posed boundary value problems with fully specified boundary conditions (Fig. 3.3, right).

The displacement field \mathbf{u}^{FEM} is the equilibrium field computed by the finite-element solver, minimizing the total potential energy of the system, which includes the strain energy stored in the continuum model and the potential energy in the regularization springs. Noisy \mathbf{u}^{FEM} fields are penalized by the strain energy associated with the high local displacement gradients of the continuum model (beam) and excessively smoothed \mathbf{u}^{FEM} fields are penalized by the increased potential energy of the regularization springs defined as

$$U_S = \sum_{i=1}^N \sum_j \left(\frac{1}{2} \mathbf{k}_j^i (\mathbf{d}_j^i)^2 \right), \quad (3.22)$$

where $j = \{x, y, z\}$, N is the number of attached regularization springs, \mathbf{k}_j^i is the spring stiffness, and the spring distension \mathbf{d}_j^i is defined as $\mathbf{d}_j^i = \mathbf{u}^{OF} - \mathbf{u}^{FEM}$. In order to relate the image-based confidence values to physically relevant springs stiffnesses, each stiffness is obtained not only as a function of local image texture, but also of the local nodal stiffness of the mechanical model. Therefore, the stiffness of each regularization spring is computed as

$$\mathbf{k}_j^i = \beta \mathbf{K}_j^i \mathbf{c}_{ij}^{OF}, \quad (3.23)$$

where i is the node index, β is the regularization coefficient, and \mathbf{K}_j^i is the nodal stiffness of the mechanical model. Nodal stiffness values are the diagonal members of the global stiffness matrix, assembled from contributions of individual elemental stiffness matrices (see [136] for details). The time-evolving global stiffness matrix is computed by the finite-element solver and is available and updated at every solution increment.

The balance between image-based and mechanics-based contributions of the final regularized displacement is governed by the stiffness of the attached regularization springs. As shown in Eq. 4.2, the spring stiffness contains a scaling parameter β . A judicious choice of the parameter β ensures that an optimal balance between the

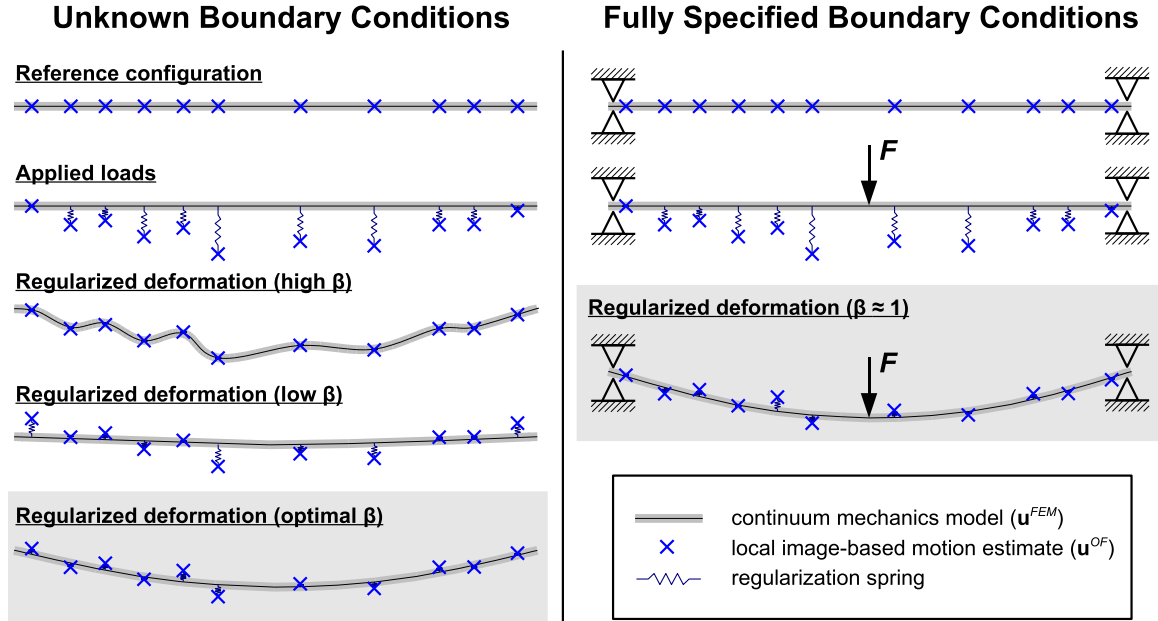


Figure 3.3: Deformation of a continuum mechanics model (beam) with image-based forces in the form of elongated regularization springs. The class of problems where boundary conditions are unknown is shown on the left. A well-posed boundary value problem with fully specified boundary conditions is shown on the right.

continuum body strain energy and spring potential energy costs is achieved. For problems in which the optical field data is the only available information, the parameter β must be sufficiently high to impose the deformation on the body. Conceptually, for the schematic in Fig. 3.3, if the deformation of the beam is only driven by the displacement of the free ends of the springs, excessive compliance of the springs will result in underestimation of the deformation. For well-posed boundary value problems (BVPs), in which either traction or displacements are known over the entire boundary, the deformation of the continuum (finite-element) model could be driven entirely by these boundary conditions.

We consider two applications of the proposed framework, where 3DUS imaging can be combined with surface (boundary) information to provide (1) accurate reconstruction of organ inner field deformation and (2) enhanced measurement of the constitutive response of an organ. For inner field reconstruction, the boundary conditions drive the global deformation, while the regularization springs impose local constraints. The spring stiffness does not need to exceed the model stiffness, therefore values of $\beta \approx 1$ are more appropriate. When measuring the constitutive response of an organ, the normalized potential energy in the springs, defined as

$$\Phi(\mathbf{p}_n) = \sum_{i=1}^N \sum_j \left(\frac{\frac{1}{2} \mathbf{k}_j^i (\mathbf{d}_j^i)^2}{\frac{1}{2} \beta \mathbf{K}_j^i} \right) = \sum_{i=1}^N \sum_j \mathbf{c}_{ij}^{OF} (\mathbf{u}_{ij}^{OF} - \mathbf{u}_{ij}^{FEM})^2 \quad (3.24)$$

is a measure of model-experiment agreement. The energy is normalized by model stiffness to prevent artificial bias towards compliant models. Additionally, the spring energy is normalized by the regularization coefficient β . This parameter determines the image-mechanics coupling balance in the conventional image registration applications. When modeling the constitutive response of an organ, we seek to identify mechanical models which are consistent with the local unregularized motion estimates \mathbf{u}^{OF} . Therefore, the choice of parameter β does not affect the model-experiment fitting. Using the objective function $\Phi(\mathbf{p}_n)$ defined in Eq. 5.26, imperfect models are associated with higher levels of regularization energy. In principle, if the model were perfect, the regularization energy would be a measure only of the noise in the optical flow. The magnitude of the regularization energy, therefore, can be considered a measure of the accuracy of a constitutive formulation, and minimization algorithms can be used for optimal parameter selection.

3.4 Evaluation and Results

In the following sections we evaluate the registration framework in three image registration experiments and one material parameter identification study. These studies are summarized in Table 3.1 and are intended to validate and evaluate the performance of the method in both of its intended application scenarios.

Table 3.1: Summary of evaluation studies presented.

| Study Description | Type | Material Law | BCs |
|---------------------------|--------------|-----------------------|------------|
| Synth. Cube (Compression) | registration | linear elastic | unknown |
| Synth. Cube (Torsion) | registration | nonlinear elastic | unknown |
| Liver Indentation | registration | nonlinear elastic | specified |
| Synth. Liver Indentation | par. ID | nonlinear poroelastic | specified |

In the first study we evaluate the accuracy of the estimated deformation field using a two frame synthetic deformation of textured unit cube. The unit cube is deformed in unconfined uniaxial compression and we assume linear elastic constitutive law and unknown boundary conditions. The accuracy is evaluated against a ground-truth deformation field and compared to traditional optical flow methods with image-based regularization. Performance under noise is also evaluated. This study demonstrates the benefits of the mechanically regularized registration method over a relatively large range of the regularization coefficient β .

In the second study we demonstrate the effects of nonlinear material response and boundary conditions on registration accuracy using a two frame synthetic deformation of textured unit cube in torsion. In this case β is assumed to be well-chosen and constant, while the normalized boundary force is varied. We demonstrate that an appropriate nonlinear regularizer offers improved accuracy over a linear elastic regularizer even when boundary conditions are unknown, and also show that the best registration accuracy is achieved when boundary force is known exactly.

The third study evaluates the performance of the registration algorithm on an experimentally obtained indentation of perfused porcine liver using manually tracked anatomical markers. To use a nonlinear regularizer with realistic mechanical response, we assume nonlinear hyperelastic constitutive material law and estimate its parameters with a traditional inverse modeling of the force-displacement response at the tip of the indenter. Using this well-chosen regularizer, we demonstrate the utility of the registration framework for estimation of accurate inner field deformation of an organ (such as surface deformation driven brain shift estimation, liver tumor localization, etc.). In this study, the boundary conditions are assumed to be known, regularization coefficient $\beta = 1$, and the deformation is tracked continuously over 240 volumetric frames. We demonstrate that an appropriately chosen nonlinear regularizer offers an improved accuracy of estimated inner field deformation compared to a linear elastic regularizer and an unregularized local optical flow.

As demonstrated by Balakrishnan et al. (2007) [11], unique identification of material bulk and shear response in indentation requires additional sensor information (i.e. secondary indenters, image-based surface deformation tracking, volumetric deformation tracking, etc.). In the fourth study we demonstrate the utility of the frame-

work in material parameter estimation scenarios. We use experimentally obtained boundary conditions to drive the model deformation and evaluate the volumetric model-experiment agreement by the level of potential energy contained in the regularization springs. Using a synthetically generated sequence of 100 3DUS frames, we demonstrate that the method converges to ground-truth parameters of a nonlinear poroelastic constitutive law initialized from three distinct locations in the parameter space, suggesting the existence of a unique global minimum.

3.4.1 Synthetic Unit Cube: Unconfined Uniaxial Compression

To obtain ground truth motion field for performance evaluation, we generate a synthetic deformation sequence (Fig. 3.4) by unconstrained compression (nominal $\epsilon_z = 0.05$) of volumetric texture ($30 \times 30 \times 30$ voxels) obtained by imaging liver parenchyma with 3D ultrasound (SONOS 7500, Philips Medical Systems, Andover, MA, USA). We register the image volume to a mechanical finite-element model with corresponding geometry ($1.1 \times 1.4 \times 0.9$ cm) and linearized material properties (elastic modulus, $E = 1.0 \text{ kPa}$ [133], and Poisson's ratio, $\nu = 0.25$, reflecting high local compressibility). Warping the volumetric texture with the deformation field obtained from the mechanical model provides a synthetic image sequence and a ground-truth motion field, which we use in subsequent performance evaluations.

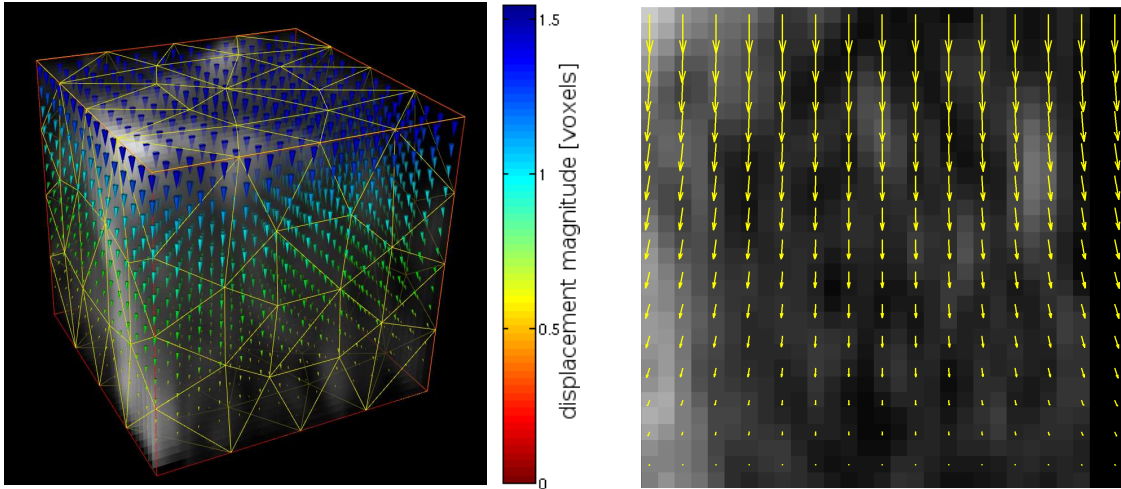


Figure 3.4: Left: Ground-truth uniaxial compression deformation field, depicted with oriented cones (size and color proportional to magnitude), and the finite-element regularization model. Right: 2D slice through the deformation field ($y=15$).

The accuracy of the recovered deformation field is evaluated in terms of mean mag-

nitude error (MME) and mean angular error (MAE) for four regularization schemes: the mechanics-based regularization, gradient-smooth Horn & Schunck optical flow regularization, Laplacian-smooth regularization [63], and local Lucas-Kanade optical flow. MME and MAE are mean error measures between the ground-truth optical flow \mathbf{u}^{true} and the estimated optical flow \mathbf{u} defined as

$$MME = \frac{1}{N} \sum_{\Omega} |\mathbf{u}^{true}(x, y, z) - \mathbf{u}(x, y, z)| \quad (3.25)$$

and

$$MAE = \frac{1}{N} \sum_{\Omega} |\angle \mathbf{u}^{true}(x, y, z) - \angle \mathbf{u}(x, y, z)| \quad (3.26)$$

over the volume domain Ω containing N voxels.

In this synthetic study, the evaluation of MME as a function of β (Fig. 3.5, left) shows that the optimal regularization point is achieved at $\beta = 5.72$. Lower values produce smoother motion fields and higher values preserve more high-frequency content, including noise. The simulation results demonstrate that for our chosen geometry, mechanical properties, and imaging characteristics, the mechanics-based regularizer is superior to Horn & Schunck and Lucas-Kanade (Table 3.2) in the range of $\beta = \langle 1.179, 187.4 \rangle$ (Fig. 3.5). For the purposes of this comparison the choice of an optimal regularization parameter α in the first-order smooth and Laplacian smooth Horn & Schunck implementation is made such that the mean magnitude error (MME) is minimized.

To gain a sense of the effect of noise on the performance of the algorithm, we perform noise analysis of the linear elastic deformation estimates by injecting varying levels

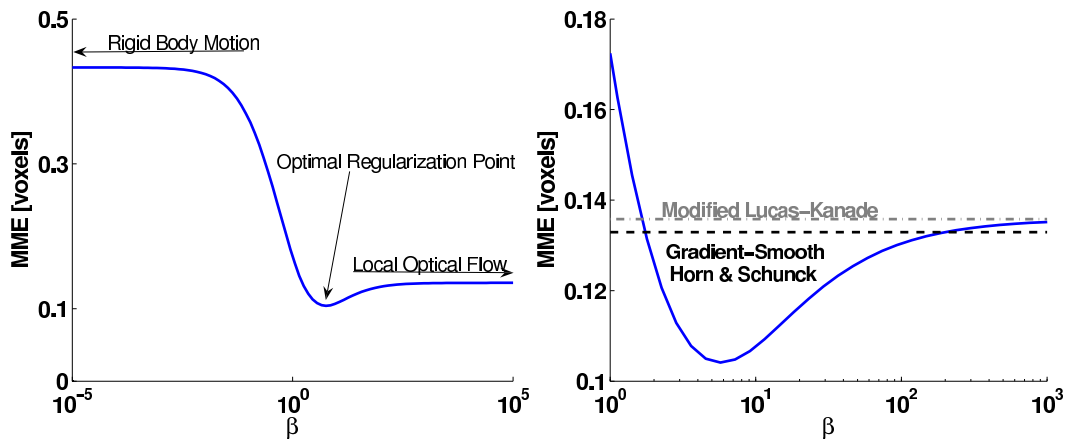


Figure 3.5: The effects of the regularization parameter β on registration accuracy (left), and a subsection of the same graph (right) showing the range of parameter β for which the mechanical regularizer performs better than traditional regularizers.

Table 3.2: Mean magnitude error (MME) and mean angular error (MAE) of common optical flow techniques compared to the mechanically regularized approach.

| Method | MME [voxels] | MAE [deg] |
|--|-----------------|--------------|
| Mechanics ($\beta = 5.72$, $\nu = 0.25$) | 0.1041 | 3.6941 |
| ∇u Horn & Schunck ($\alpha = 16.0$) | 0.1329 | 4.7162 |
| $\nabla^2 u$ Horn & Schunck ($\alpha = 6.0$) | 0.1391 | 9.0781 |
| Local Lucas-Kanade | 0.1358 | 4.8191 |

of multiplicative Gaussian noise into the local motion estimates (Fig. 3.6). The level of noise varies from noise-free local motion (corresponding to the ground-truth motion field) to Gaussian distributed with standard deviation $\sigma_N = 0.8$ voxels. These simulations demonstrate that as the level of noise increases, mechanical regularization (β near optimal regularization point) provides increasing benefit over local methods ($\beta \rightarrow \infty$).

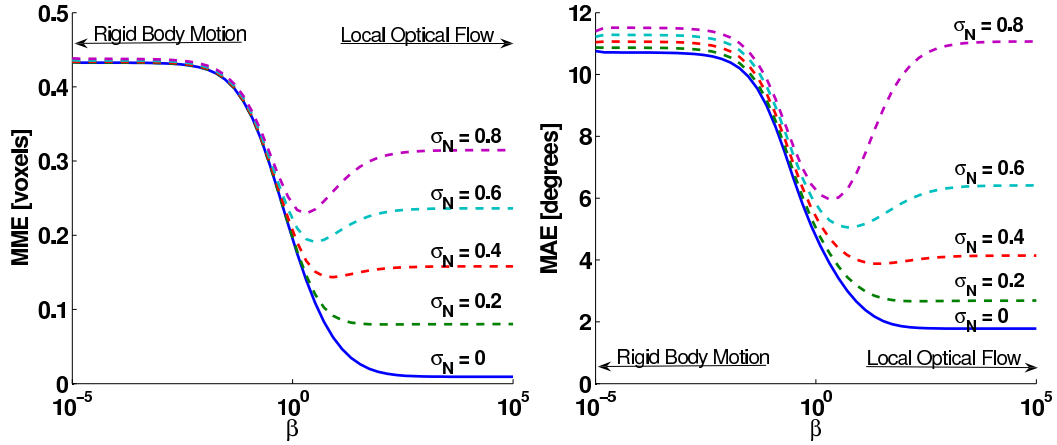


Figure 3.6: Mean magnitude error (left) and mean angular error (right) with varying levels of local optical flow error (multiplicative, Gaussian-distributed noise with variance σ_N injected into ground-truth local optical flow).

3.4.2 Synthetic Unit Cube: Torsion

While linear elasticity is an adequate approximation of material mechanics in the small-deformation regime, most materials (especially biological) exhibit a nonlinear stress-strain relationship in the large-deformation regime. We demonstrate these effects by selecting two common material laws (linear elastic and 2^{nd} -order reduced

polynomial hyperelastic) and parameters, whose uniaxial loading stress-strain characteristics coincide at low strains (less than 1%) and diverge at higher strains in both shear and bulk material response. The goal of this synthetic study is to demonstrate that a nonlinear regularizer can be easily implemented in this framework and to evaluate the performance benefits over the linear elastic regularizer.

We generate the ground-truth nonlinear torsional displacement field (shown in Fig. 3.7) by constraining the bottom surface of the previously described material cube and applying a torsional moment of $7.0 \times 10^{-7} N \cdot m$ to the rigid top. The 2nd-order reduced polynomial strain energy formulation of the reduced polynomial form [60, 1] is defined as

$$U = C_1 (I_1 - 3) + C_2 (I_1 - 3)^2 + \frac{1}{D_1} (J_{el} - 1)^2 \quad (3.27)$$

where C_1 , C_2 , and D_1 are the material parameters, I_1 is the 1st stretch invariant, and J_{el} is the elastic volumetric stretch. The selected material parameters ($C_1 = 0.2 \times 10^3$, $C_2 = 0.5 \times 10^4$, $D_1 = 1.5 \times 10^{-3}$) are reasonable choices for a biological material, such as porcine liver parenchyma in the large deformation mode (see experimental liver tracking section below for details on liver-specific parameters). The linear elastic material used in the previous synthetic study ($E = 1.0 kPa, \nu = 0.25$) may be rewritten as a 1st-order reduced polynomial with the coefficients $C_1 = 0.2 \times 10^3$ and $D_1 = 1.5 \times 10^{-3}$ and serves as a small-deformation approximation of the 2nd-order material.

In this study we evaluate the nonrigid registration accuracy as a function of the normalized boundary force applied to the regularization model and a constant regularization coefficient ($\beta = 1.0$). In experimental scenarios where boundary forces and displacements may be directly measured or controlled, the knowledge of these constraints further improves registration accuracy. The results of this study demonstrate that even partially known boundary conditions can greatly improve the motion estimates. The improvement gained by the knowledge of boundary conditions is demonstrated in Fig. 3.8 as a dependence of MME on the applied normalized boundary force ($F_N = 1$ corresponds to the ground-truth boundary force). These results suggest that while a linear elastic regularizer with no knowledge of the boundary force ($F_N = 0$) can provide better accuracy than image-driven regularizers (gradient-smooth Horn & Schunck algorithm shown in red dashed line in Fig. 3.8), the knowledge of nonlinear mechanics and boundary conditions ($F_N = 1$) can further improve the deformation estimates. It is important to note that this example is meant to demonstrate a trend of improvement in a single frame-to-frame deformation and results in an incremental benefit in long-time, large-deformation, multiple-frame registration scenarios. In these situations, nonlinear mechanics become even more important and the knowledge/control of boundary conditions provides a constraint on accumulation errors, which are a well documented [79] and significant source of error in multiple-frame motion estimation.

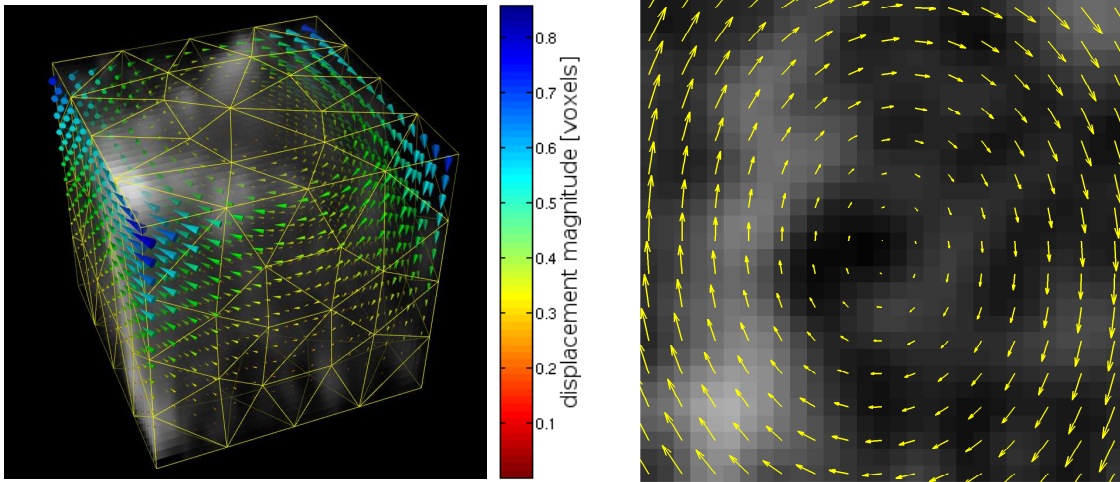


Figure 3.7: Left: Ground-truth torsional deformation field, depicted with oriented cones (size and color proportional to magnitude), and the nonlinear finite-element regularization model. Right: 2D slice through the deformation field ($z=15$).

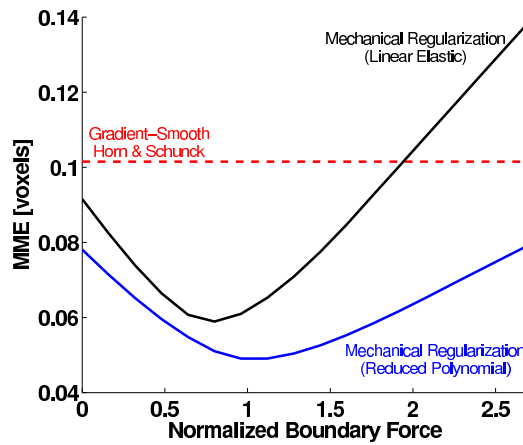


Figure 3.8: The nonlinear 2^{nd} -order reduced polynomial regularizer (lower line) outperforms the linear elastic regularizer (black line) and gradient-smooth Horn & Schunck optical flow (red dashed line) both in the presence and absence of known boundary conditions. The registration error improvement is most significant when the exact ground-truth boundary force ($F_N = 1$) is applied to the regularization model.

3.4.3 Liver Indentation: Inner Field Estimation

To demonstrate the ability of the registration algorithm to estimate large-displacements over multiple frames in an experimental setting, we evaluated its registration accuracy

against manually segmented motion of three anatomical tissue markers in a perfused porcine liver indentation experiment (Fig. 4.1, left). Following the experimental protocol described in [71] and [69], the liver was indented with a cylindrical indenter (12 mm diameter, 10 mm total displacement) actuated by material testing system (Electroforce ELF 3200, Bose Corporation, Eden Prairie, MN, USA), while the volumetric deformation was acquired with 3D ultrasound probe (SONOS 7500, Philips Medical Systems, Andover, MA, USA) placed below the tissue sample, as shown in Fig. 3.10. The 3DUS volume was registered to a simplified cylindrical liver model (10 cm diameter, 3 cm height). To obtain tissue specific material parameters, we fit the indentation force-displacement response to a finite-element model with 2^{nd} -order reduced polynomial hyperelastic constitutive law through an iterative inverse FEM approach [70]. We make the assumption of compressibility, $\nu = 0.3$ (ν is not directly observable in indentation experiments), and obtain the material parameters ($C_1 = 236.6$, $C_2 = 520.9$, $D_1 = 9.75 \times 10^{-4}$), reflecting the fit to the loading portion of the indentation response (Fig. 4.1, right).

The trajectories of three tissue markers (shown in Fig. 3.10) were obtained by manually tracking their displacements in a 3DUS sequence consisting of 240 frames acquired at 25Hz. The marker displacement histories serve as the ground-truth motion for this evaluation. The accuracy of our method, using a linear elastic regularizer, nonlinear hyperelastic regularizer, and no regularization, is summarized in Fig. 3.11 and demonstrates the feasibility of this approach in the presence of considerable imaging noise associated with 3DUS data. The marker trajectories in Fig. 3.10 (right) show good agreement between the manually segmented and estimated displacements along the vertical axis.

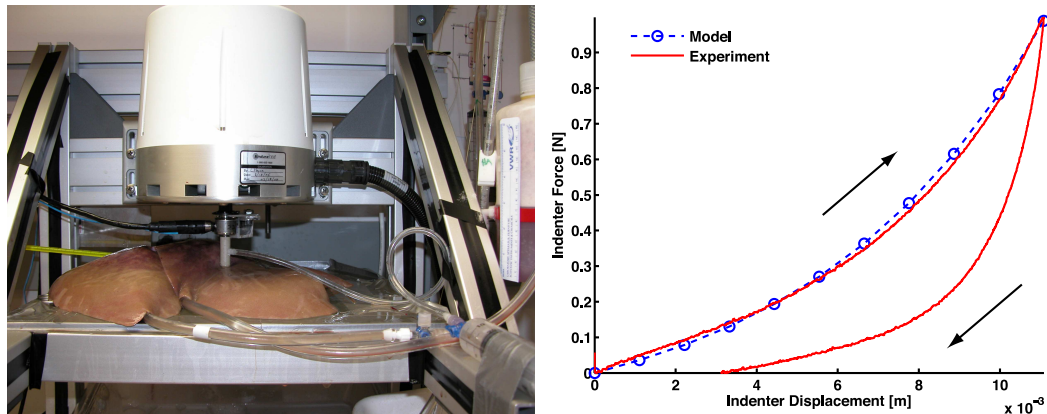


Figure 3.9: Left: The perfused porcine liver is indented with a cylindrical indenter actuated by Bose Electroforce ELF 3200 material testing system. Right: Experimental force-displacement indentation response (red) obtained from a 0.2Hz load/unload cycle and a 2^{nd} -order reduced polynomial model fit (blue).

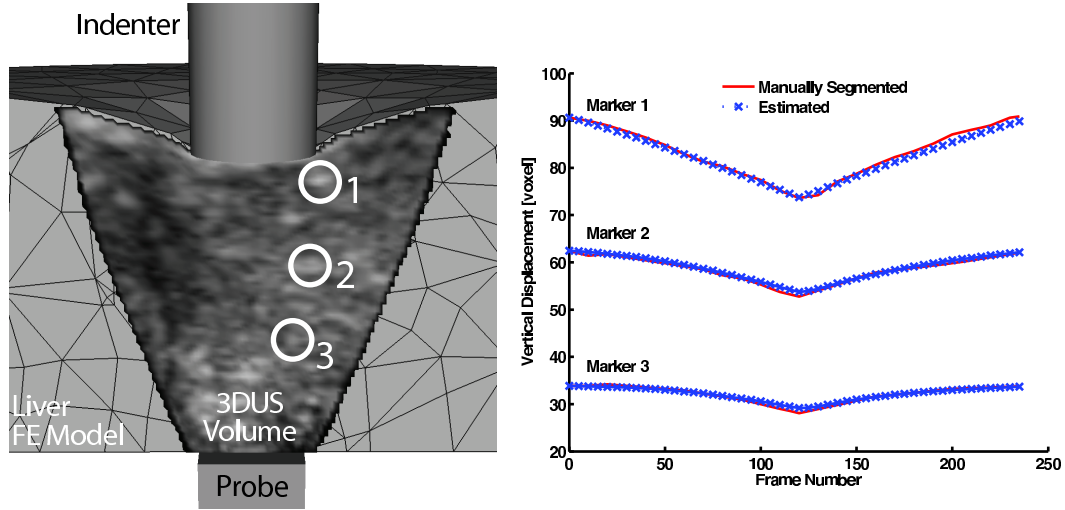


Figure 3.10: Left: Experimental configuration, showing a cut through the deforming finite-element model, the 3DUS volume, and three tissue markers used for evaluation. Right: Vertical trajectories of the markers estimated by nonrigid registration algorithm with 5-frame incremental registration steps, using 2nd-order reduced polynomial constitutive law, evaluated against manually segmented marker trajectories.

Due to the small frame-to-frame displacement requirements of the optical flow constraint used in the local Lucas-Kanade motion estimates, the accuracy of the local motion estimates degrades with increasing indenter velocity. This trend is captured in Fig. 3.11, demonstrating the performance benefits of a mechanical regularizer ($\beta = 1$ assumed in all studies). These results suggest that for properly chosen material parameters, a nonlinear hyperelastic regularizer provides better accuracy than a linear elastic regularizer ($E = 1.0 \text{ kPa}$, $\nu = 0.3$) and the unregularized local optical flow.

3.5 Discussion

We have presented a nonrigid registration algorithm regularized by a mechanical finite-element model suitable for applications in 3D ultrasound tissue tracking and material parameter estimation. One of the key contribution of this method is the image-mechanics coupling approach, which uses regularization springs attached at nodal locations to impose image-based motion estimates. This approach avoids the need for direct computation of image forces and provides an intuitive assignment of image-based motion confidence, reflecting the spatial variations in texture quality.

A key advantage of this framework is its modular structure, under which the choices of image similarity measure, local search algorithm, image-mechanics confidence mapping, and most importantly, the mechanical model's material law and

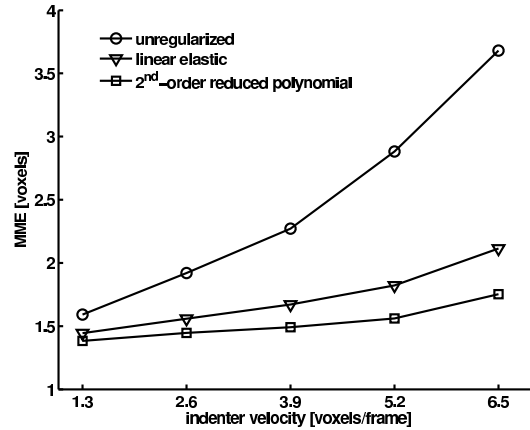


Figure 3.11: Performance of the nonrigid registration algorithm with increasing indenter velocity, demonstrating the benefits of a properly chosen nonlinear regularization model over the linear elastic regularizer and the unregularized local optical flow.

solver, are completely independent. This ability to leverage state-of-the-art mechanical modeling packages is of key importance, as it enables the use of nonlinear, viscoelastic material models of arbitrary complexity in nonlinear interactions, such as large strains and variable contact conditions, without the need for a reliable custom-made FEM solver. This flexibility becomes increasingly important with the ongoing progress and increasing complexity of constitutive mechanical models formulated specifically for large-strain behavior of biological tissues. Additionally, the proposed framework also allows for incorporation of information from other sensor modalities (Doppler ultrasound, tissue sono-crystals, electromagnetic trackers, ultrasound RF strain estimates, etc.) through additional regularization spring elements.

Through synthetic and real-world evaluations, we demonstrated the benefits of the nonrigid registration algorithm over traditional regularizers in image-based optical flow methods. Additionally, we have shown the extensibility of the framework by incorporating nonlinear and rate-dependent tissue constitutive laws into the regularization model. Our results suggest that, in the large deformation mode, there are significant benefits to using nonlinear, tissue-specific constitutive laws for mechanically constrained nonrigid registration even in the presence of unknown boundary conditions. As expected, the knowledge of boundary conditions significantly improves the registration accuracy and reduces the underestimation bias of the approximation solution schemes.

Finally, the proposed registration framework is suitable for applications in mechanical parameter identification and provides good accuracy and sensitivity to the bulk and shear components of the material response. This ability is of high importance to future characterization of complex constitutive laws and is appealing for *in*

in vivo applications, where tissue and organ boundaries cannot be directly controlled. Boundaries can instead be imaged and accounted for in the inverse modeling process. While the evaluations in this chapter were performed on synthetic and well-controlled *ex vivo* tissues, the methodology is independent of the imaging modality and mechanical tissue model used, showing its promise for future investigation of patient-specific tissue modeling and parameter identification.

Chapter 4

Image-Based Mechanical Characterization of Soft Tissues

4.1 Introduction

Computational models of organ and tissue mechanical response are beginning to play a significant role in modern computerized medicine and have become integral components of image-guided surgery and interventions [25, 29, 37, 5, 26, 6]. Such image-guided tasks require close interplay of computational biomechanical models with preoperative and intraoperative imaging. The development of appropriate models is challenging for two reasons: a) formulation of suitable constitutive laws capable of capturing the large-strain, nonlinear, viscoelastic response of soft tissue and b) development of experimental testing protocols appropriate for unique identification of the material parameters. In addition, the significant subject-to-subject variability contributes to a strong need for patient-specific (personalized) models, which may be generated and parameterized with clinically feasible testing protocols.

Material properties of soft tissues vary significantly between *in vivo* and *in vitro* settings [48, 91, 93, 53, 90, 71]. Current *in vivo* soft tissue testing is dominated by indentation due to the limited access requirements, simplicity of the tool configuration, and low-risk of injury associated with the procedure [11]. The single force-displacement history obtained during conventional indentation experiments is governed by the mechanical response of the whole material domain, combining near-field (large strain) and far-field (low strain) contributions. Much of the information related to the interplay between shear and bulk compliance in the complex deformation field beneath the indenter is lost when capturing this single output. Therefore, supplemental experimental methods, such as secondary indentation sensors [11], tissue surface tracking [41, 42], or independent tests of bulk compliance (i.e. confined tissue compression) are necessary for well-conditioned parameter identification. Image-based characterization methods are a promising solution, as they provide the

means for noninvasive, *in vivo* estimation of material parameters and offer improved sensitivity and uniqueness of recovered parameters.

A general inverse finite-element modeling framework is presented for applications in constitutive modeling and parameter estimation of soft tissues using full-field volumetric deformation data obtained from 3D ultrasound. We validate the parameter estimation method on synthetically generated data and perform constitutive model selection for perfused porcine liver in indentation. While we limit our investigation to an experimental protocol, which involves a single indenter displacement rate, the volumetric imaging captures local tissue strain rates in the range from zero to the maximum rate beneath the indenter. Considering the image-based agreement with the internal tissue displacement field, we determine an appropriate constitutive law and material parameters, which capture the time-dependent of the tissue.

4.2 Methods

In this chapter we describe a liver indentation experimental system and an inverse finite-element modeling framework, which takes advantage of concurrent image data obtained from 3D ultrasound imaging. While the liver is an inhomogeneous organ with complex anatomical structure, our model approximates it as a homogeneous and isotropic material. The characteristic length of the hepatic lobules, the functional units of the organ, is on the order of 1 mm. Therefore, the concept of homogenizing the tissue is justifiable for deformation fields applied over longer length scales (approximately 1cm). In this work we also neglect the effects of the liver capsule and minimize the contributions from vasculature by examining the parenchyma with 3DUS and avoiding the placement of the indenter over large vessels. The proposed approach relies on the following components: experimental indentation and liver perfusion apparatus, volumetric imaging system, a nonrigid registration algorithm for deformation field estimation, and a nonlinear parameter optimization algorithm. The design considerations and performance of each component are described in the following sections. In addition, we present a validation study and an application of this framework to constitutive modeling of perfused porcine liver in indentation.

4.2.1 Experimental Setup

Liver Perfusion Apparatus

Due to changes in the liver's mechanical properties *ex vivo* [69, 96], it is important to measure the organ response in its physiological conditions. Measurement of boundary conditions and instrument access are often the limiting factors in *in vivo* testing. To address these challenges, we used an *ex vivo* perfusion system, described by [69] and depicted in Figure 4.1. This system allowed us to perform organ tests with control of boundary conditions and near *in vivo* tissue state. The whole porcine liver

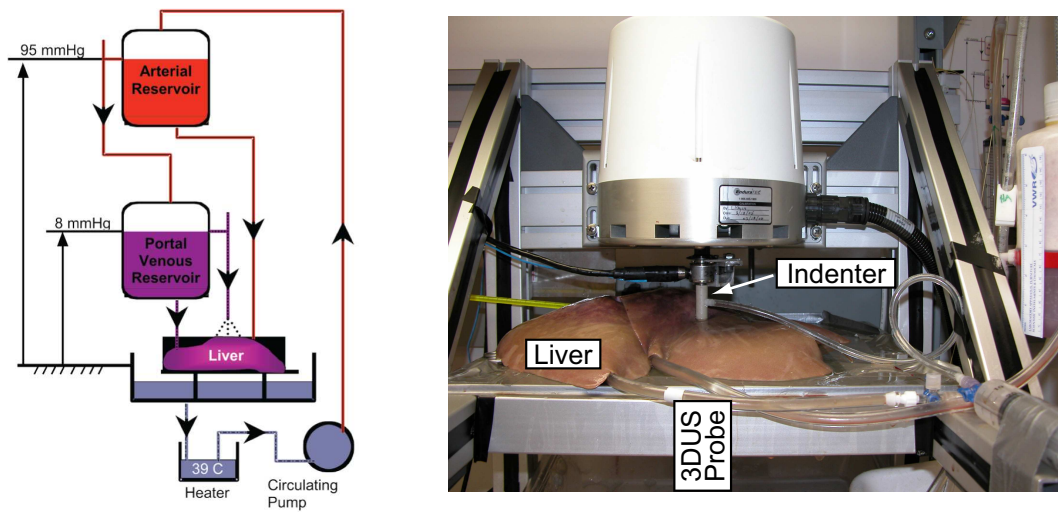


Figure 4.1: Left: liver perfusion system. Right: the experimental arrangement showing the indenter at the top surface of the organ and the 3DUS probe beneath the organ.

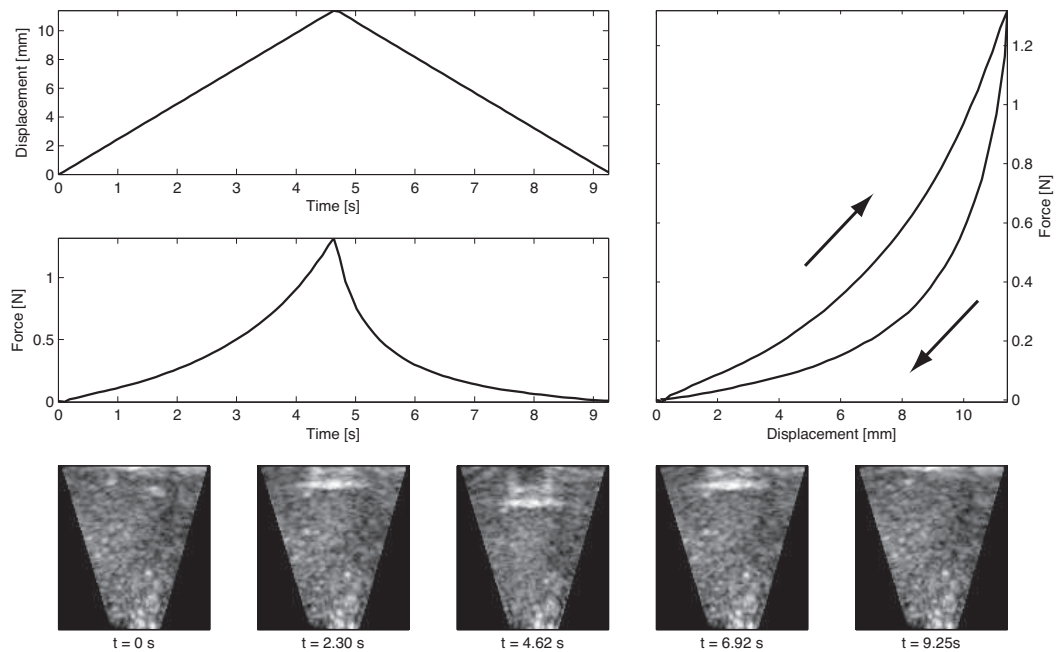


Figure 4.2: The indenter force and displacement histories and force-displacement indentation response, acquired during $2 \text{ mm}\cdot\text{s}^{-1}$ load/unload cycle. The associated 2D slices through the 3DUS sequence are shown at the bottom.

was perfused with a heated perfusate (five liters of Dextrose 5% Lactated Ringers Solution (D5RL) and one liter of 6% Hetastarch (Henry Schein, Melville, NY)) under physiologic pressures, with a mean portal venous pressure of 7.98 mmHg, a mean hepatic arterial pressure of 94.77 mmHg, and at a mean temperature of 33°C.

Following the experimental protocol described in [71] and [69], the liver was indented with a 12mm diameter, flat, cylindrical indenter actuated by Bose Electroforce ELF 3200 material testing system (Bose Corporation EnduraTEC Systems Group, Minnetonka, MN). The system measures displacement using a linear variable differential transformer (Schaevitz MHR-250 from Measurement Specialties, Hampton, VA) with 6.3 mm travel (0.559 μm RMS alone, 3.9 μm RMS with controller), force using a 22 N submersible load cell (0.49 mN RMS alone, 13 mN RMS with controller) (Honeywell Sensotec Sensors Model 31, Columbus Ohio), and acceleration using a 50 g accelerometer (0.024 V RMS alone, 0.204V RMS with controller) (Kistler, Amherst NY).

Volumetric Imaging

The volumetric deformation was imaged with the 3D ultrasound probe (SONOS 7500, Philips Medical Systems, Andover, MA, USA) placed below the tissue sample, as shown in Fig. 4.1. The 2-4MHz probe acquires data at the rate of 26 frames per second, which is subsequently streamed over an Ethernet connection to a PC workstation for storage and processing. The transducer was operated at a 7cm depth of focus to provide sufficient field of view, which contains the organ surface, parenchyma, and the probe stand-off pad. The resulting volumetric frames were rasterized at 128x48x204 voxels, corresponding to an axial resolution of approximately 0.3 mm/voxel and a lateral resolution of 0.5 mm/voxel. Two-dimensional image slices of the volumetric sequence and the associated indenter force and displacement histories, acquired during a 2 mm.s⁻¹ load/unload cycle, are shown in Figure 4.2.

4.2.2 Nonrigid Image Registration and Constitutive Modeling

We use a nonrigid registration scheme (Fig. 4.3), described in further detail in [65], to estimate the deformation field captured by the concurrent 3DUS imaging. The volumetric image data obtained during organ indentation contains relatively slow deformations (maximum tissue displacement is less than 0.3 voxels per frame) and the liver parenchyma produces rich textural content under 3DUS (see Figure 4.2). Given these conditions, the algorithm achieves good accuracy and robustness. In Jordan et al. (2008) [65] we demonstrate the accuracy against manually tracked tissue landmarks (mean magnitude error of less than 0.6mm) in *ex vivo* liver indentation and present a quantitative error analysis using synthetic deformation sequences.

In the proposed nonrigid image registration scheme, sparse image-based local motion estimates \mathbf{u}^{OF} and associated confidence \mathbf{c}^{OF} are estimated with an adapted implementation of the [84] optical flow algorithm described in Appendix A. These local motion estimates are enforced as concentrated forces applied at the nodes of a deformable finite-element organ model, enforcing physically admissible deformations. The concentrated forces are generated by regularization springs, connected to the mesh nodes, as their free ends are displaced according to local motion estimates. The choice of each regularization spring stiffness reflects local textural quality and associated local motion confidence. This approach not only provides regularized estimate of organ deformation field (\mathbf{u}^{FEM}) but also offers a measure of model/experiment agreement in the form of normalized potential energy (Φ) contained in regularization springs. The displacement field \mathbf{u}^{FEM} is the equilibrium field computed by the finite-element solver, minimizing the total potential energy of the system, which includes the strain energy stored in the continuum model and the potential energy in the regularization springs. Consequently, noisy \mathbf{u}^{FEM} fields are penalized by the strain energy associated with the high local displacement gradients of the continuum model and excessively smoothed \mathbf{u}^{FEM} fields are penalized by the increased potential energy of the regularization springs defined as

$$U_S = \sum_{i=1}^N \left(\frac{1}{2} \mathbf{k}_j^i (\mathbf{d}_j^i)^2 \right), \quad (4.1)$$

where $j = \{x, y, z\}$, N is the number of attached regularization springs, \mathbf{k}_j^i is the spring stiffness, and the spring distension \mathbf{d}_j^i is defined as $\mathbf{d}_j^i = \mathbf{u}^{OF} - \mathbf{u}^{FEM}$. In order to relate the image-based confidence values to physically relevant springs stiffnesses, each stiffness is obtained not only as a function of local image texture, but also of the local nodal stiffness of the mechanical model. Therefore, the stiffness of each regularization spring is computed as

$$\mathbf{k}_j^i = \beta \mathbf{K}_j^i \mathbf{c}_{ij}^{OF}, \quad (4.2)$$

where i is the node index, β is the regularization coefficient, and \mathbf{K}_j^i is the global stiffness of node i in direction j (obtained from the diagonal members of the global stiffness matrix).

The image registration framework is suitable for two types of fundamentally different applications. In the first category of applications, the framework may be used to obtain a mechanically admissible image registration, such as between preoperative and intraoperative images. In these applications the biomechanical model and the image similarity term are coupled via the regularization springs to provide mechanically consistent inner organ deformations. Examples of such applications include the intraoperative brain shift, tumor localization, mammogram registration, etc. The second category consists of applications in constitutive organ response characterization. When external forces and boundary conditions are known or experimentally

measured, the registration framework may be used to optimize the consistency between the chosen biomechanical model and the experimental images. When measuring the constitutive response of an organ, an objective function $\Phi(\mathbf{p}_n)$ derived from the springs potential energy U_S , may be defined as

$$\Phi(\mathbf{p}_n) = \sum_{i=1}^N \sum_j \left(\frac{\frac{1}{2} \mathbf{k}_j^i (\mathbf{d}_j^i)^2}{\frac{1}{2} \beta \mathbf{K}_j^i} \right) = \sum_{i=1}^N \mathbf{c}_i^{OF} (\mathbf{u}_i^{OF} - \mathbf{u}_i^{FEM})^2 \quad (4.3)$$

and serves as an appropriate measure of model-experiment agreement. The energy is normalized by model stiffness to prevent artificial bias towards compliant models. Additionally, the spring energy is normalized by the regularization coefficient β . This parameter determines the image-mechanics coupling balance in the conventional image registration applications. When modeling the constitutive response of an organ, we seek to identify mechanical models which are consistent with the local unregularized motion estimates \mathbf{u}^{OF} . Therefore, the choice of parameter β does not affect the model-experiment fitting¹. Using the objective function $\Phi(\mathbf{p}_n)$ defined in Eq. 5.26, imperfect models are associated with higher levels of regularization energy. The magnitude of the regularization energy, therefore, can be considered a measure of the accuracy of a constitutive formulation, and minimization algorithms can be used to determine optimal material parameters.

In our experimental configuration, the force and displacement histories at the tip of the indenter are acquired with higher accuracy and lower noise in comparison to the optical flow measurements. To incorporate these sensor measurements into the optimization framework, we define an objective function $\dot{\Phi}$, which is the sum of a volumetric error term $\dot{\Phi}_{vol}$ and an indenter error term $\dot{\Phi}_{ind}$ defined as

$$\dot{\Phi}_{vol}(\mathbf{p}_n) = \frac{1}{NT} \int_0^T \sum_{i=1}^N \mathbf{c}_i^{OF}(t) (\dot{\mathbf{u}}_i^{OF}(t) - \dot{\mathbf{u}}_i^{FEM}(t))^2 dt \quad (4.4)$$

and

$$\dot{\Phi}_{ind}(\mathbf{p}_n) = \frac{1}{T} \int_0^T (\dot{\mathbf{u}}_z^{exp}(t) - \dot{\mathbf{u}}_z^{model}(t))^2 dt. \quad (4.5)$$

The volumetric error term $\dot{\Phi}_{vol}$ is the mean squared difference between the optical flow and the model velocity fields over the time period T normalized by the number of regularization springs N . The indenter error term $\dot{\Phi}_{ind}$ is the mean squared difference between the vertical indenter velocity $\dot{\mathbf{u}}_z^{exp}(t)$ and the modeled indenter velocity

¹The role of the regularization parameter (and corresponding spring stiffness) is significant in scenarios where the framework is used for estimation of the inner organ deformation fields (i.e. brain shift problems, liver tumor localization, etc.). Details regarding these applications may be found in chapter 3

$\dot{\mathbf{u}}_z^{model}(t)$. Such definition of the objective function scales the two error components to comparable magnitudes and aids in obtaining model fits consistent with experimental tissue displacement field as well as the indenter force-displacement history.

Throughout this paper, we chose to use indenter and nodal velocity histories as the measure of model-experiment agreement. Objective functions based on velocity-based or displacement-based model-experiment agreement are both suitable choices for model optimization. The differential optical flow estimates are frame-to-frame displacement estimates (not absolute). Therefore, small estimation errors may contribute to more significant accumulation error when integrated over long periods of time [79]. For this reason, we determined the velocity fields as the more appropriate choice and were able to confirm their improved convergence properties.

Liver Finite-Element Model

The perfused *ex vivo* liver is modeled with a finite-element model implemented in a commercial FE solver (ABAQUS 6.7, Simulia, Providence, RI, USA). The model has a simplified cylindrical geometry (10cm diameter, 3cm height) shown in Fig. 4.4, as most of the contributions to the indentation response are assumed to be local and not significantly dependent on the whole organ geometry. The mesh is generated automatically with increased density beneath the indenter and consists of 1424 nodes and 804 quadratic tetrahedral elements. The bottom surface of the organ is fully constrained, while the upper and side surfaces are assumed to be stress-free boundaries. The force at the tip of the indenter is prescribed to match the indentation force history obtained experimentally.

4.2.3 Method Validation: Synthetic Volumetric Data

To evaluate the sensitivity of the testing method to material parameters, accuracy of the parameters recovered, and to assess the convergence characteristics of the optimization scheme, we conducted a parameter identification study on a synthetically generated 3DUS sequence. We computed a ground-truth deformation field from a "forward" finite-element model of the indentation experiment with assumed constitutive law and material parameters. We used a high density mesh (4281 nodes, 2706 quadratic tetrahedral elements) in the forward model to minimize field discretization artifacts. The boundary conditions of the forward model were prescribed to match the boundary conditions of the real experimental procedure. The displacement and force histories at the tip of the indenter were recorded to mimic the measurements obtained during the *ex vivo* experimental procedure. The resulting deformation field was used to warp a reference 3DUS volume, generating a sequence of 100 volumes. The reference 3DUS volume is a single frame acquired by imaging perfused *ex vivo* liver. Consequently, the generated volumetric sequence preserves the true texture and intensity distribution of liver parenchyma under 3DUS. This synthetic study,

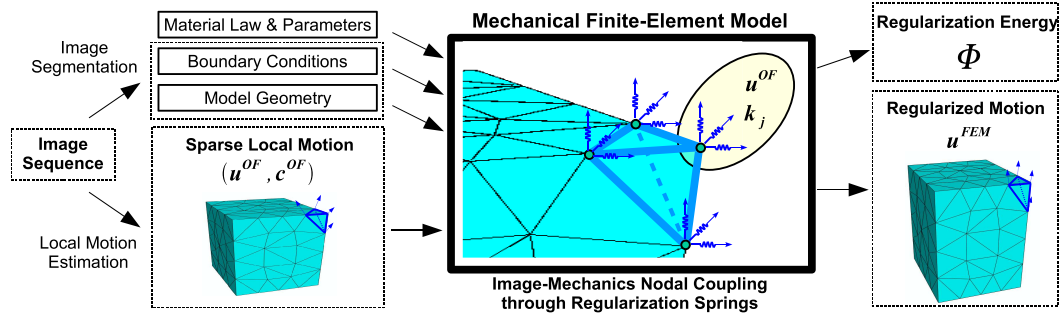


Figure 4.3: In the nonrigid image registration framework, sparse local motion estimates \mathbf{u}^{OF} are coupled to a mechanical finite-element model as lumped body forces applied by displaced regularization springs. This results in a mechanically constrained deformation field \mathbf{u}^{FEM} and regularization energy Φ .

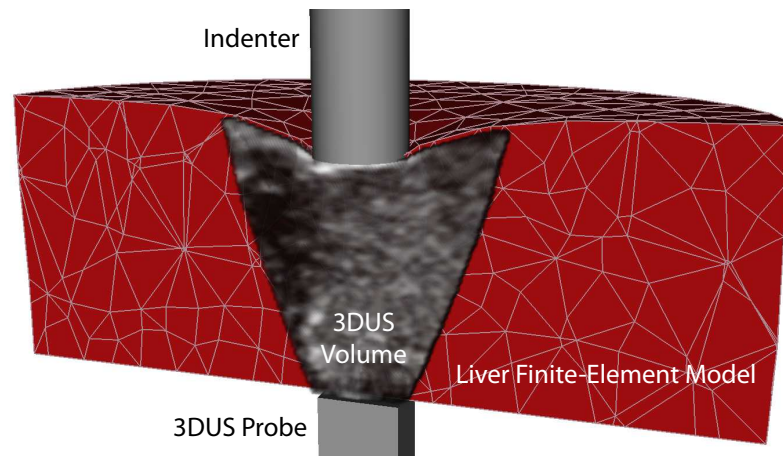


Figure 4.4: The deforming finite-element liver model with simplified cylindrical geometry, experimentally measured boundary conditions, and a coregistered 3DUS sequence.

however, excludes image artifacts and noise contributions from the imaging sensor.

Biphasic Poroelastic Constitutive Law

To mimic the nonlinear viscoelastic response of the perfused porcine liver, we use a biphasic (mixture theory) constitutive model [119, 135]. Biphasic models account for viscous material effects through momentum exchange effects between the solid and fluid phases. The solid phase is formulated through the 2^{nd} -order reduced polynomial strain-energy defined as

$$U = C_1 (I_1 - 3) + C_2 (I_1 - 3)^2 + \frac{1}{D_1} (J_{el} - 1)^2 \quad (4.6)$$

where C_1 , C_2 , and D_1 are the material parameters, I_1 is the 1^{st} stretch invariant, and J_{el} is the elastic volumetric stretch. The flux of the fluid phase is governed by Darcy's law expressed as

$$\mathbf{q} = \kappa \nabla \mathbf{P}, \quad (4.7)$$

where \mathbf{q} is the flux, κ is the permeability coefficient, and $\nabla \mathbf{P}$ is the fluid pressure gradient.

Using the synthetic 3DUS sequence and force-displacement indentation histories, we perform material parameter estimation in a way that is identical to the approach used with true experimental liver measurements. The geometry and boundary conditions of the FE model used in this inverse process reflect the assumed experimental conditions. The indentation force $F(t)$ is applied at the tip of the indenter, and the bottom surface of the organ is fully constrained. We initialize material parameters with feasible parameter estimates and use a nonlinear optimization algorithm, a bounded downhill simplex method [76], to iteratively evolve the material parameters (C_1, C_2, D_1, κ) and minimize the objective function $\Phi(\mathbf{p}_n)$.

Quasilinear viscoelastic Constitutive Law

In the second synthetic parameter recovery study we perform parameter identification using an alternative constitutive material law, a 2^{nd} -order reduced form polynomial hyperelastic law with a Prony series relaxation of the shear modulus [60, 57]. The hyperelastic strain energy of this constitutive law defined in Eq. 4.6 and the relaxation of the shear modulus $G(t)$ is captured by a 1^{st} -order Prony series

$$G(t) = G_0 (g_\infty + g_1 e^{-t/\tau_{g1}}), \quad (4.8)$$

where G_0 is the instantaneous shear strain modulus (computed from Eq. 4.6), $G_0 g_\infty$ is the equilibrium shear strain modulus, $g_1 = 1 - g_\infty$ is the relative amplitude of the relaxation, and τ_{g1} is the relaxation time constant. The biphasic poroelastic constitutive law governing the response of the synthetic deformation is known to exhibit bulk

relaxation. We evaluate the volumetric agreement with a shear relaxation constitutive law to demonstrate the ability to distinguish between materials with inherently different modes of relaxation. We also evaluate the method's ability to consistently converge to the best possible fit under the given assumptions.

4.2.4 Perfused Porcine Liver Constitutive Modeling

We perform constitutive modeling of perfused porcine liver in indentation (2 mm.s⁻¹ load/unload cycle) using the proposed inverse modeling framework. We constrain our attention to the 2nd-order reduced polynomial hyperelastic form

$$U = C_1 (I_1 - 3) + C_2 (I_1 - 3)^2 + \frac{1}{D_1} (J_{el} - 1)^2 + \frac{1}{D_2} (J_{el} - 1)^4 \quad (4.9)$$

and shear and bulk relaxation components

$$G(t) = G_0 (g_\infty + g_1 e^{-t/\tau_{g1}}) \quad (4.10)$$

$$K(t) = K_0 (k_\infty + k_1 e^{-t/\tau_{k1}}). \quad (4.11)$$

Under this general form, we explore 5 constitutive laws. In the shear relaxation variant (SR), the relaxation of the tissue is assumed to be captured by the relaxation of the instantaneous shear modulus. The bulk compliance is assumed to be linear ($D_2 = 0$) and no bulk relaxation is permitted ($k_1 = 0$). In the subsets SR_{low} and SR_{high} we enforce low ($D_1 = 1.0 \times 10^{-4}$) and high ($D_1 = 3.0 \times 10^{-3}$) bulk compliance, respectively, to investigate the effects of bulk compliance on the full-field deformation fields.

To investigate the role of bulk relaxation we consider two additional constitutive laws. First, we consider a bulk relaxation (BR) model with 2nd- order bulk compliance and no shear relaxation ($g_1 = 0$). Second, we considered the full constitutive law (SBR) with relaxation of both bulk and shear moduli.

4.3 Results

4.3.1 Method Validation: Synthetically Generated Volumetric Data

Biphasic Poroelastic Constitutive Law

Using the synthetically generated deformation sequence governed by biphasic poroelastic constitutive law, the parameter estimation framework consistently converges to the ground-truth parameter values. The evolution of the objective function during the optimization processes seeded from 3 distinct points in the parameter space

is shown in Fig. 4.5, left. The convergence of the material parameters for all 3 seeds is shown in Fig. 4.5, right. These results are summarized in Table 4.1 and demonstrate that in the absence of imaging noise (a consequence of synthetic data) the method converges consistently and recovers both bulk and shear response parameters with good sensitivity.

Quasilinear Viscoelastic Constitutive Law

The parameter estimation of the quasilinear viscoelastic constitutive law using the deformation sequence with assumed biphasic poroelastic response is summarized Fig. 4.6 and Table 4.2. These results suggest that the method converges consistently for all 3 seed points and is able to obtain excellent indenter response agreement with the ground-truth data (see Fig. 4.7). However, when comparing the magnitudes of the volumetric error, this form of constitutive law offers lesser volumetric agreement with the data. This point is further illustrated by comparing the nodal velocities of the poroelastic (PE), viscoelastic (VE), and optical flow data in Fig. 4.8. Since the PE model corresponds to the ground-truth deformation, Fig. 4.8 demonstrates the volumetric disparity of the VE model. In addition, the good agreement of the optical flow estimates with the PE model serves as a validation of the motion estimation scheme (in the absence of imaging system noise). In addition, it serves as a basis for measuring the noise floor of the motion estimation system. Minor oscillations in the optical flow estimates may be observed at some nodes due to voxel-to-element correspondence effects near the model boundary.

4.3.2 Perfused Porcine Liver Constitutive Modeling

The results of the constitutive modeling of perfused porcine liver are summarized in Table 5.3 and Fig. 4.9. Several observations should be noted regarding the methods ability to characterize the material response and its contributions in the constitutive law selection process.

The results of the quasilinear viscoelastic constitutive law with shear modulus relaxation (SR) demonstrate that the proposed parameter identification method is capable of recovering the linear bulk compliance parameter D_1 , which is not observable in conventional indentation tests. While the indentation response (Fig. 4.9 top middle) is nearly identical for all three SR models, the volumetric nodal velocities differ significantly. This disparity is captured by comparing the SR model's volumetric error term ($\dot{\Phi}_{vol} = 2.15 \times 10^{-5}$) to the SR_{low} ($\dot{\Phi}_{vol} = 3.52 \times 10^{-5}$) and SR_{high} ($\dot{\Phi}_{vol} = 2.25 \times 10^{-5}$) models with assumed low and high bulk compliance D_1 , respectively. These findings indicate that estimating the bulk compliance parameter D_1 from the full-field deformation data maximizes the volumetric model/experiment agreement.

The parameter identification results using the BR and SBR models suggest that

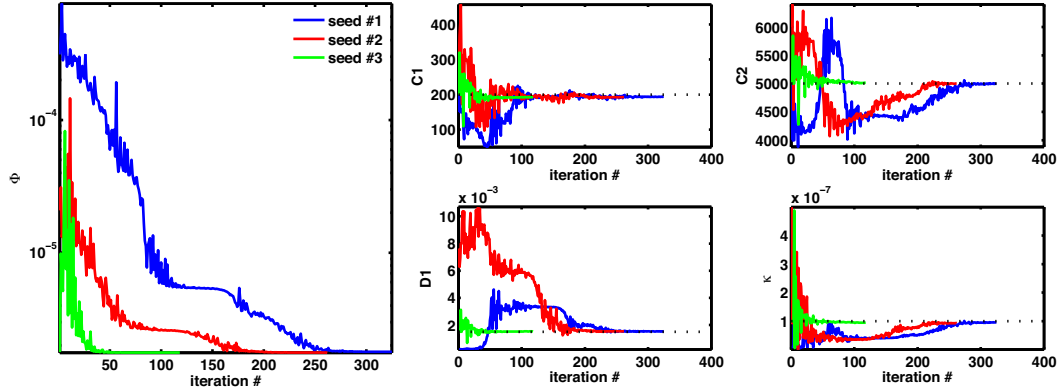


Figure 4.5: Biphase poroelastic CL: regularization energy evolution (left) and material parameter evolution (right) during material parameter identification seeded from 3 different locations in the parameter space.

Table 4.1: Biphase poroelastic CL: recovered material parameters and associated regularization energy obtained from 3 independent parameter seed points (initial parameter values shown in parentheses). Ground-truth values: $C_1 = 200$, $C_2 = 5000$, $D_1 = 1.5 \times 10^{-4}$, $\kappa = 1.0 \times 10^{-7}$

| Parameter | Seed 1 | Seed 2 | Seed 3 |
|--------------------|---|---|---|
| C_1 | 193.6 (150) | 192.4 (300) | 192.7 (200) |
| C_2 | 4,998 (4,000) | 4,999 (6,000) | 5,014 (5,000) |
| D_1 | 1.53×10^{-3} (2.0×10^{-4}) | 1.53×10^{-3} (5.0×10^{-3}) | 1.53×10^{-3} (1.5×10^{-3}) |
| κ | 0.96×10^{-7} (1.0×10^{-8}) | 0.93×10^{-7} (5.0×10^{-7}) | 0.95×10^{-7} (1.0×10^{-7}) |
| $\dot{\Phi}$ | 2.63×10^{-6} (6.39×10^{-6}) | 2.63×10^{-6} (9.10×10^{-6}) | 2.63×10^{-6} (2.65×10^{-6}) |
| $\dot{\Phi}_{ind}$ | 1.08×10^{-8} (2.54×10^{-6}) | 1.23×10^{-8} (5.12×10^{-6}) | 1.22×10^{-8} (1.70×10^{-8}) |
| $\dot{\Phi}_{vol}$ | 2.62×10^{-6} (3.85×10^{-6}) | 2.62×10^{-6} (3.98×10^{-6}) | 2.62×10^{-6} (2.63×10^{-6}) |

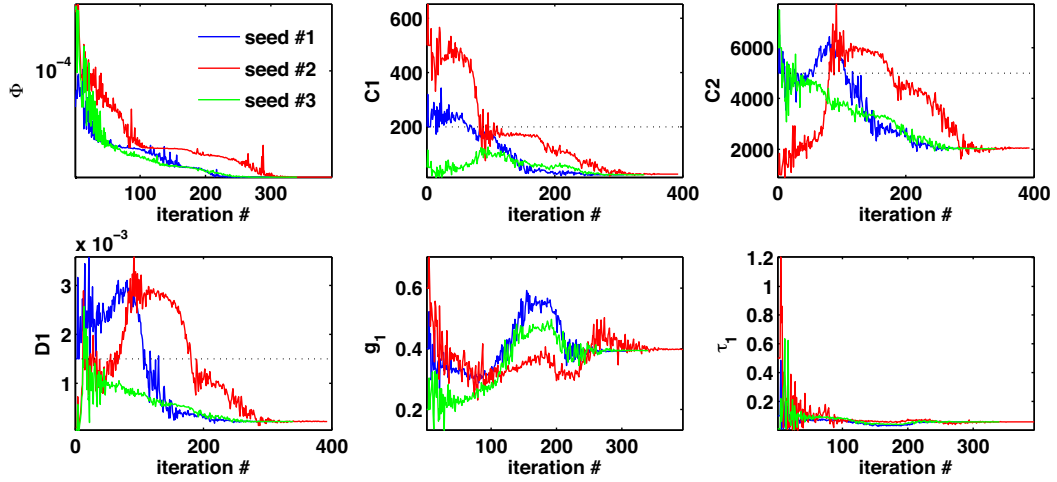


Figure 4.6: Quasilinear viscoelastic CL: regularization energy evolution (top left) and material parameter evolution during material parameter identification seeded from 3 different locations in the parameter space.

Table 4.2: Viscoelastic CL - recovered material parameters and associated regularization energy obtained from 3 independent parameter seed points (initial parameter values shown in parentheses).

| Parameter | Seed 1 | Seed 2 | Seed 3 |
|--------------------|---|---|---|
| C_1 | 23.1 (200) | 24.9 (500) | 23.1 (50) |
| C_2 | 2,039 (5,000) | 2,048 (1,000) | 2,030 (6,000) |
| D_1 | 2.25×10^{-4} (1.5×10^{-3}) | 2.27×10^{-4} (1.0×10^{-4}) | 2.24×10^{-4} (5.0×10^{-5}) |
| g_1 | 0.392 (0.400) | 0.398 (0.600) | 0.394 (0.200) |
| τ_1 | 0.059 (0.100) | 0.058 (0.500) | 0.059 (0.010) |
| $\dot{\Phi}$ | 1.57×10^{-5} (1.90×10^{-5}) | 1.51×10^{-5} (1.07×10^{-4}) | 1.56×10^{-5} (6.01×10^{-5}) |
| $\dot{\Phi}_{ind}$ | 9.32×10^{-6} (1.13×10^{-5}) | 8.82×10^{-6} (9.87×10^{-5}) | 9.18×10^{-6} (5.54×10^{-5}) |
| $\dot{\Phi}_{vol}$ | 6.39×10^{-6} (7.79×10^{-6}) | 6.32×10^{-6} (7.79×10^{-6}) | 6.38×10^{-6} (4.69×10^{-6}) |

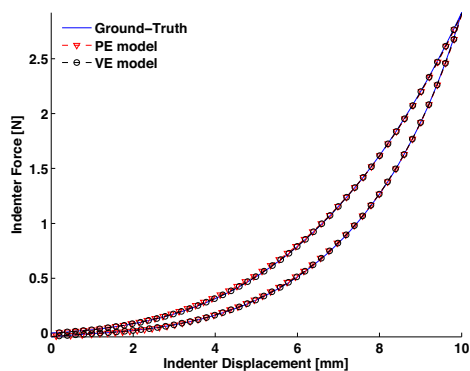


Figure 4.7: The force-displacement indentation response of the poroelastic model (PE) and viscoelastic model (VE) showing excellent agreement with ground-truth data.

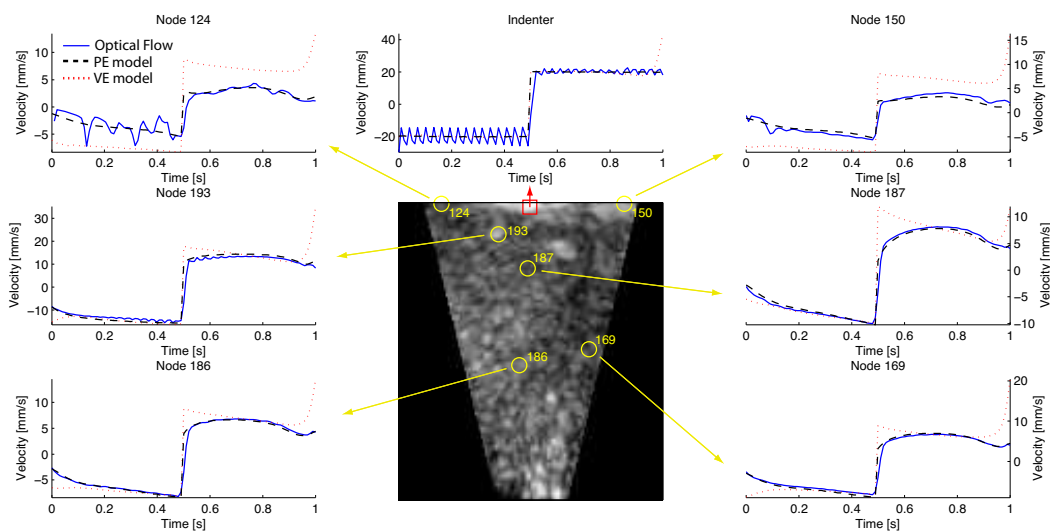


Figure 4.8: Ground-truth deformation sequence: mesh node velocity histories of the poroelastic (PE) and viscoelastic (VE) models compared to optical flow estimates. Only the vertical component of velocity is shown. The selected nodes are within 10mm of the center plane shown.

bulk modulus relaxation does not significantly improve the model fit ($\dot{\Phi}_{vol} = 3.8 \times 10^{-5}$ for BR, $\dot{\Phi}_{vol} = 2.20 \times 10^{-5}$ for SBR). For this mode and rate of deformation the simple SR constitutive form is able to account for the material response both at the indenter as well as volumetrically (within the precision of the imaging and deformation tracking systems).

The agreement between the model and the experiment was also quantified in terms of the root mean squared (RMS) error of the indenter and of the nodal displacement histories. While nodal velocity mean squared error (MSE) was found to be the more appropriate objective function choice for model optimization, the nodal displacement RMS errors provide an intuitive measure of the model-experiment agreement. Under this metric, the SR model offers good indenter displacement agreement (0.19 mm RMS error) and volumetric deformation agreement (0.97 mm axial RMS error).

4.4 Conclusions and Discussion

In this chapter a method for constitutive model selection and parameter identification using real-time 3DUS volumetric imaging was presented and validated. This approach enriches the traditional force-displacement indentation response with the measurement of volumetric deformation and provides good sensitivity to parameters governing the bulk response of the material. These parameters are otherwise not observable in conventional indentation. The ability to decouple the bulk and shear components of the deformation is of high importance and we demonstrated that we can reconstruct the parameters with high precision and repeatability in a validation study. Furthermore, the measurement of full volumetric deformation histories offers the ability to observe material response over a range of strain rates. While the indenter is driven at a chosen displacement rate, the local material strain rates throughout the tissue sample vary from zero in the far-field to the maximum levels beneath the indenter. The method is independent of imaging modality and constitutive law, suggesting potential applications for other tissues and scales (i.e. nanoindentation, confocal microscopy, etc.).

The proposed approach is a useful tool for constitutive model selection, as suggested in our porcine liver indentation modeling. The best experimental fits were attained with a quasilinear viscoelastic model with 2nd-order reduced polynomial instantaneous response and a Prony series relaxation of the bulk and shear moduli. Using the full-field measurements, we demonstrated that a simpler constitutive form with shear relaxation provides comparable model-experiment agreement. This observation suggests that shear relaxation is the dominant mode of relaxation for liver in indentation and that the SR model is appropriate (considering the reduced number of parameters).

One of the advantages of the proposed method is the ease of application in *in vivo* settings. The knowledge/observation of boundary condition is one of the chief

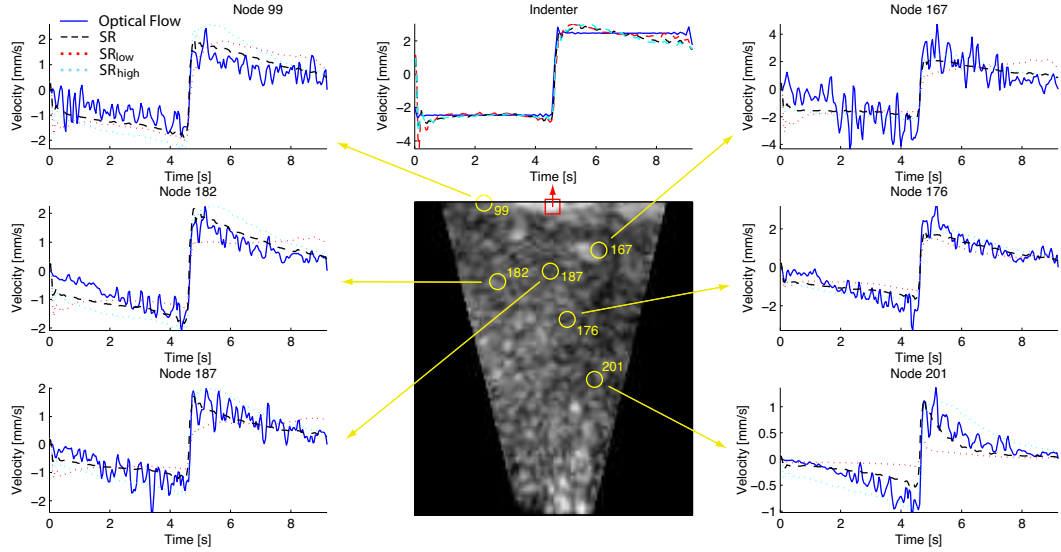


Figure 4.9: Perfused liver sequence: indentation histories (top, middle) are virtually identical between SR , SR_{low} , and SR_{high} . The SR model provides significantly improved volumetric agreement illustrated with vertical node velocity histories.

Table 4.3: Perfused porcine liver: estimated material parameters for the 5 constitutive laws considered.

| Parameter | SR_{low} | SR_{high} | SR | BR | SBR |
|--------------------|-----------------------|-----------------------|-----------------------|-----------------------|-----------------------|
| C_1 | 4.3 | 185.4 | 79.2 | 83.9 | 71.6 |
| C_2 | 47.0 | 612.6 | 257 | 40.9 | 218.3 |
| D_1 | 1.0×10^{-4} | 3.0×10^{-3} | 4.38×10^{-4} | 4.71×10^{-4} | 3.65×10^{-4} |
| D_2 | - | - | - | 2.22×10^{-5} | 6.7×10^{-3} |
| g_1 | 0.967 | 0.779 | 0.832 | - | 0.794 |
| τ_{g1} | 0.585 | 0.168 | 0.150 | - | 0.203 |
| k_1 | - | - | - | 0.890 | 0.032 |
| τ_{k1} | - | - | - | 0.134 | 0.176 |
| $\dot{\Phi}$ | 3.52×10^{-5} | 2.25×10^{-5} | 2.15×10^{-5} | 3.08×10^{-5} | 2.20×10^{-5} |
| $\dot{\Phi}_{ind}$ | 1.52×10^{-7} | 1.69×10^{-7} | 1.31×10^{-7} | 1.58×10^{-7} | 1.35×10^{-7} |
| $\dot{\Phi}_{vol}$ | 3.51×10^{-5} | 2.24×10^{-5} | 2.14×10^{-5} | 3.06×10^{-5} | 2.19×10^{-5} |

motivating factors for *ex vivo* testing. Imaging the organ during indentation testing, however, offers the ability to observe the *in vivo* boundary conditions and account for them during the inverse modeling process. Direct *in vivo* indentation tests of the liver can be performed in the operating room due to the relatively easy access to the organ within the abdominal cavity. The method may also find suitable applications in noninvasive (percutaneous) organ characterization. Such applications will require proper image segmentation and mechanical models, which incorporate the tissue inhomogeneities, layers, and organ boundaries.

In our future work, we intend to incorporate constitutive laws with higher complexity [71, 85], which are capable of capturing the liver response across the DC-2Hz frequency range characteristic of surgical manipulation.

Chapter 5

Viscoelastic Characterization of Perfused Porcine Liver

5.1 Introduction

The liver is a frequently manipulated organ in abdominal procedures, therefore a thorough characterization of the nonlinear, visco-elastic mechanical response in the modes of deformation representative of surgical manipulation is crucial for emerging image-guided technologies, robotic procedures, and surgical simulation. The liver has a complex internal structure consisting of vascular, structural, and cellular elements (blood, bile, lymph, collagen, hepatocytes, endothelial cells), giving rise to its nonlinear rate-dependent mechanical response. Because the liver is a highly perfused organ, its observed mechanical properties are strongly dependent on the physiological conditions (i.e. temperature, arterial pressure, and venous pressure). Unlike most organs however, the liver's internal structure is relatively homogeneous (on the scale of 1 cm and above) and does not have a dominant directional dependence, suggesting that isotropic constitutive law formulations may be capable of capturing its three-dimensional response.

Much of the experimental data on the mechanical response of soft tissues is acquired in *ex vivo* conditions. Such data, however, is often inappropriate for accurate modeling and characterization, as the material properties of soft tissues vary significantly between *in vivo* and *in vitro* settings [48, 91, 93, 53, 90, 71]. Kerdok et al. [71] have demonstrated that near *in vivo* mechanical behavior may be achieved by using physiologic perfusion conditions in an *ex vivo* setting, while providing testing conditions amenable to extensive characterization of the organ's visco-elastic response and well-controlled experimental boundary conditions. A recent study by Nava et al. [96] has demonstrated the use of an aspiration testing device to measure the mechanical properties of human liver *in vivo*. The material properties were identified via an inverse finite-element modeling approach and suggest that a quasi-linear visco-elastic

constitutive law can capture the liver response within the applied loading history and relative small deformation of the organ (considering the scale of deformations during surgical procedures). Another study by Carter et al. [24] reported on the measurements of intra-operative *in vivo* mechanical properties of human and porcine liver using indentation and fitted the experimental data to a simple exponential analytical model. Numerous other studies [23, 97, 100, 108, 112, 125] have performed *in vivo* mechanical tests in porcine and bovine animal models.

This chapter presents a comprehensive visco-elastic characterization of perfused porcine liver using conventional indentation testing and image-based material characterization proposed in chapter 4. A physically-based nonlinear visco-elastic constitutive model of the liver is fitted to data from porcine livers using iterative inverse finite-element modeling. This study examines a broad set of loading histories, including consecutive cyclic loading tests with indenter displacement rates spanning two orders of magnitude (0.2 mm/s to 40 mm/s) and stress relaxation tests. The order of the cyclic loading experiments is randomized across the three animal subjects tested and alternative loading histories are used to evaluate the model predictive capability.

5.2 Materials and methods

5.2.1 Design of experiments

Data for this study was acquired by Kerdok as described in detail in [69]. Three porcine livers from freshly sacrificed animals (60 kg mean mass) were harvested, transported from the operating room to the laboratory in an ice bath, and were perfused and tested within 1 hour after harvest. This protocol has been shown to preserve the *in vivo* response of the organ [71], while offering unrestricted access and well controlled boundary conditions. The livers were tested in an orientation consistent with the supine subject position, while the perfusate was infused continuously with a mean portal venous pressure of 7.98 mmHg (± 1.44 standard deviation), a mean hepatic arterial pressure of 94.77 mmHg (± 1.75), and at a mean temperature of 33°C (± 4.34). Temperature and pressure were continuously monitored throughout the tests to ensure proper perfusion of the liver. The 3D ultrasound probe was placed beneath the organ to capture the internal organ deformation during indentation. The complete experimental setup was described in section 4.2.1 and illustrated in Figure 4.1.

To characterize the tissue over the strain rates relevant to surgical manipulation and to capture the preconditioning effects of this heavily tissue, we subject the organs to consecutive, constant strain rate cyclic loading (indenter displacement velocity spans the range of 0.2 mm/s to 40 mm/s). Each specimen is indented three consecutive times at four loading rates (0.2 mm/s, 2 mm/s, 20 mm/s, and 20 mm/s). The order of the three cycle blocks is varied for each test. The cyclic indentation

experiments are summarized in Table 5.1. The loading history consists of triangular pulse sequences, rather than sinusoidal trajectories, which results in a richer spectral profile of each indentation. Within the small displacement approximation, sinusoidal loading histories examine the tissue response at a single discrete frequency. Triangular sequences, however have a richer spectral profile and include higher frequency components. The time-displacement histories and power spectra of the four triangular load/unload cycles considered in this study are summarized in Figure 5.1, demonstrating the range of the frequency range tested.

In addition to cyclic consecutive loading, each specimen was tested by applying fast step indentation to a constant strain (over 30%) to observe the stress relaxation of the tissue over long periods (over 1200 seconds). The stress relaxation experiments test the tissue response on significantly different time scales and approximate both the instantaneous and equilibrium response. A summary of the experiments is provided in Table 5.2.

5.2.2 Finite-element model

The results of the indentation experiments showed that the response of the tissue is strongly nonlinear and demonstrated rate-dependence in cyclic loading tests, as well as long-time relaxation in stress relaxation experiments. When appropriate organ perfusion is provided, the tests revealed that the tissue fully recovers within 20 minutes after testing [71, 69]. To capture this behavior we developed a nine-parameter visco-elastic constitutive model, which was implemented as a FORTRAN user-defined subroutine (UMAT) in ABAQUS (Simulia, Providence, RI, USA) finite-element analysis package.

Material Constitutive Law

Considering the large deformation requirements of soft tissue models, we develop a constitutive material law within the finite-strain continuum mechanics theory. The deformation gradient \mathbf{F} is defined in terms of the deformed (\mathbf{x}) and reference (\mathbf{X}) coordinates of a material particle in the body undergoing deformation as

$$\mathbf{F} = \frac{\partial \mathbf{x}}{\partial \mathbf{X}}. \quad (5.1)$$

The material deformation gradient (\mathbf{F}) may be decomposed into its deviatoric (\mathbf{F}_d) and hydrostatic (\mathbf{F}_h) components according to

$$\mathbf{F} = \mathbf{F}_h \mathbf{F}_d = J^{\frac{1}{3}} \mathbf{I} \mathbf{F}_d, \quad (5.2)$$

where J is the scalar volumetric strain (defined as $\det(\mathbf{F})$ or the ratio of the current volume V and the initial volume V_0) and \mathbf{I} is the identity matrix. The total

Table 5.1: Summary of cyclic loading indentation tests performed on three perfused porcine liver specimens.

| specimen | thickness [mm] | nominal strain | loading history |
|----------|----------------|----------------|--|
| Liver 1 | 31 | 0.35 | sequence 1: 3×0.2 mm/s, 3×20 mm/s, 3×40 mm/s, 3×2 mm/s sequence 2: 3×2 mm/s, 3×40 mm/s, 3×0.2 mm/s, 3×20 mm/s |
| Liver 2 | 32 | 0.36 | sequence 1: 3×40 mm/s, 3×20 mm/s, 3×2 mm/s, 3×0.2 mm/s sequence 2: 3×0.2 mm/s, 3×2 mm/s, 3×20 mm/s, 3×40 mm/s |
| Liver 3 | 26 | 0.36 | sequence 1: 3×40 mm/s, 3×0.2 mm/s, 3×20 mm/s, 3×2 mm/s sequence 2: 3×2 mm/s, 3×20 mm/s, 2×0.2 mm/s, 3×40 mm/s |

Table 5.2: Summary of stress relaxation indentation tests performed on 3 perfused porcine liver specimens.

| specimen | thickness [mm] | nominal strain | loading history |
|-----------------|-----------------------|-----------------------|----------------------------|
| Liver 1 | 31.34 | 0.35 | 200 mm/s load, 1800 s hold |
| Liver 2 | 32.18 | 0.34 | 200 mm/s load, 1800 s hold |
| Liver 3 | 26.12 | 0.35 | 200 mm/s load, 1200 s hold |

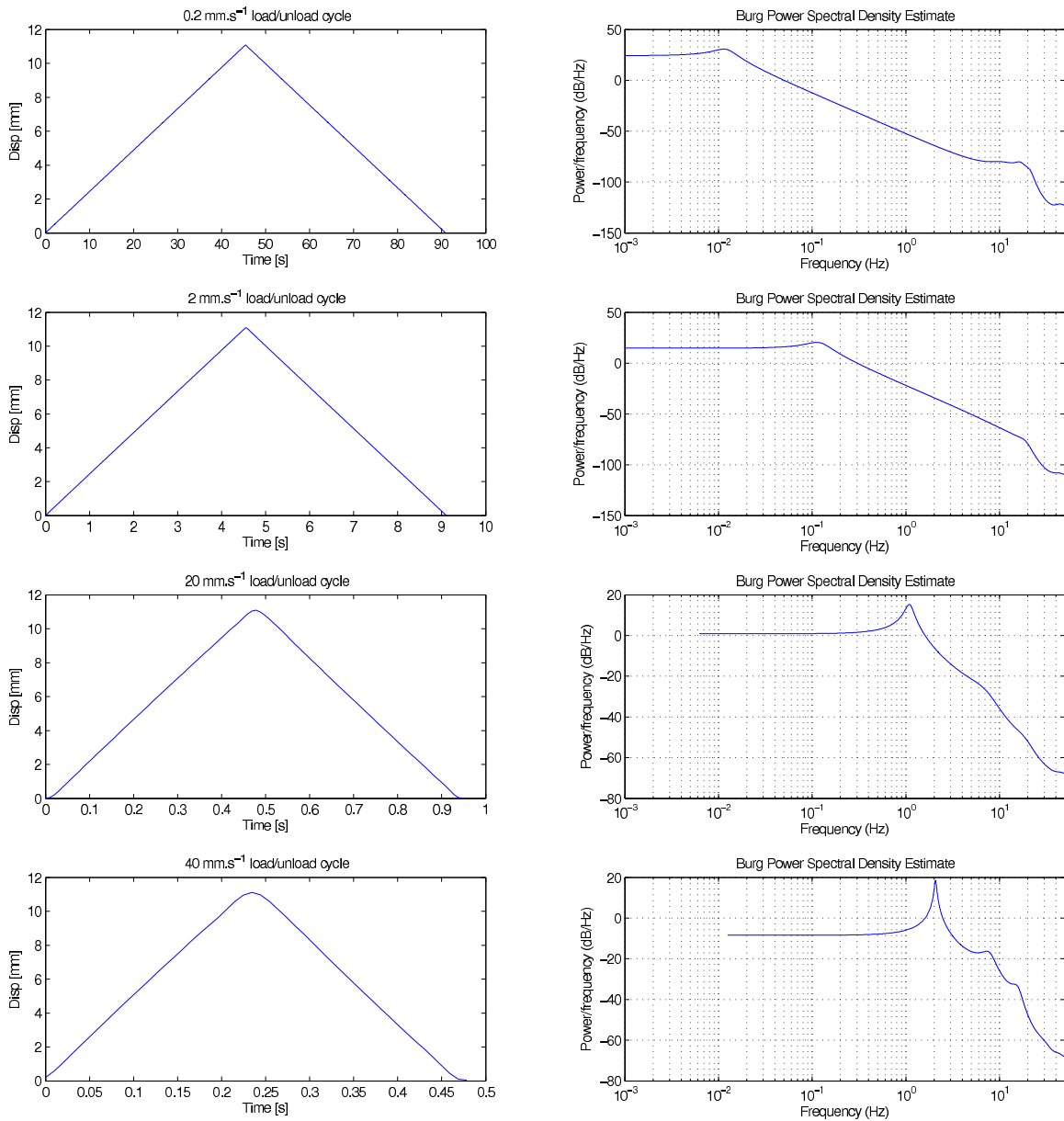


Figure 5.1: Indentation loading histories, consisting of load/unload ramps at 0.2 mm/s, 2 mm/s, 20 mm/s, and 40 mm/s, are shown in the left column and the corresponding power spectra are shown in the right column.

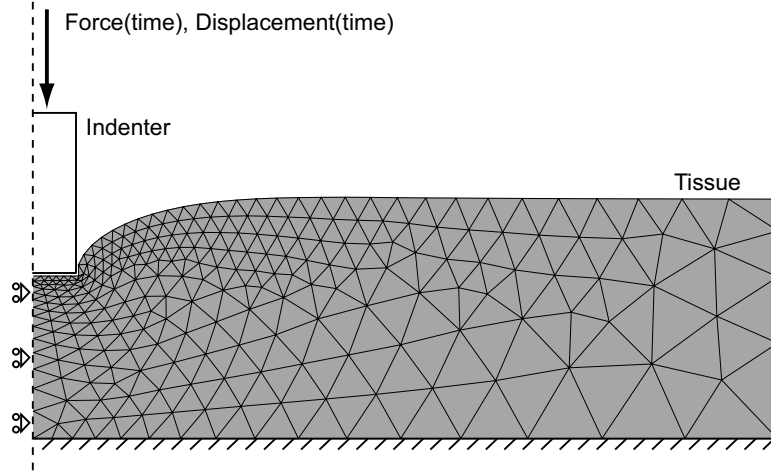


Figure 5.2: A representative axisymmetric finite-element model of the liver in indentation using quadratic triangular meshing, simplified cylindrical geometry, and experimentally observed boundary conditions.

Cauchy stress in the tissue is computed as the sum of the deviatoric and hydrostatic components

$$\mathbf{T}(\mathbf{F}) = \mathbf{T}_d(\mathbf{F}_d) + \mathbf{T}_h(\mathbf{F}_h). \quad (5.3)$$

The hydrostatic component of the Cauchy stress tensor \mathbf{T}_h is captured by a single linear elastic element responding to the volumetric component of the deformation gradient \mathbf{F}_h . A rheological network representing the response of the model to the isochoric (deviatoric) component of the deformation gradient \mathbf{F}_d is shown in Figure 5.3. The network consists of a nonlinear elastic element (A) representing the instantaneous response of the collagen network and a visco-elastic dissipative network (elements B, C, D, and E) representing the response of the cellular and fluid components of the liver parenchyma. Therefore, we divide the total deviatoric deformation gradient into its components representing the contributions from the collagen network (\mathbf{F}_c) and the parenchyma (\mathbf{F}_p).

The visco-elastic arrangement of the parenchyma component is intended to accommodate both the short-time viscous effects (associated time constant $\tau < 2$ s) of the tissue and the long-time relaxation effects ($\tau > 20$ s) observed during stress-relaxation experiments. The short-time dissipative effects are captured with a nonlinear reptation-based viscous element C, while the long-time relaxation is represented with a network configuration in the form of the standard linear solid (elements B, D, and E).

The response of the model is constrained by compatibility equations, the equilibrium equations, and the constitutive equations representing the characteristic re-

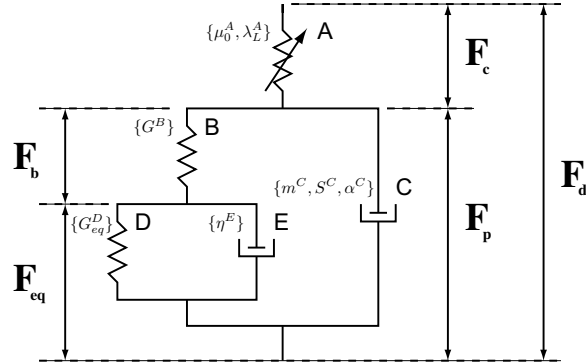


Figure 5.3: Rheological arrangement of the deviatoric component of the nonlinear viscoelastic constitutive model.

sponse of individual elastic and viscous elements. The compatibility equations may be written as

$$\mathbf{F}_d = \mathbf{F}_c \mathbf{F}_p \quad (5.4)$$

$$\mathbf{F}_p = \mathbf{F}_b \mathbf{F}_{eq} \quad (5.5)$$

and the equilibrium equations are

$$\mathbf{T}^A(\mathbf{F}_c) = \mathbf{T}^B(\mathbf{F}_b) + \mathbf{T}^C(\dot{\mathbf{F}}_p, \mathbf{F}_p) \quad (5.6)$$

$$\mathbf{T}^B(\mathbf{F}_b) = \mathbf{T}^D(\mathbf{F}_{eq}) + \mathbf{T}^E(\dot{\mathbf{F}}_{eq}, \mathbf{F}_{eq}). \quad (5.7)$$

Response of the Collagen Matrix

The response of the collagenous component of the tissue is captured by a freely jointed 8-chain model [7, 118]. In this formulation, the force-stretch relationship for an individual collagen fibril is

$$f = \frac{K_i}{b} \mathcal{L}^{-1} \left(\frac{\lambda_f}{\lambda_L} \right), \quad (5.8)$$

where K_i is the reference stiffness, b is the persistence length for the fibril, λ_f is the fibril stretch, λ_L is the limiting fibril stretch parameter, and \mathcal{L}^{-1} is the inverse Langevin function defined by

$$\beta = \mathcal{L}^{-1} \left(\frac{\lambda_f}{\lambda_L} \right) \quad (5.9)$$

$$\frac{\lambda_f}{\lambda_L} = \mathcal{L}(\beta) = \coth \beta - \frac{1}{\beta}. \quad (5.10)$$

The three-dimensional representation of the single collagen fibril model follows the representation proposed by Arruda and Boyce, using a cubic unit cell with eight individual chains connected at the center of the cell. As the cell deforms along the principal stretch directions $\{\lambda_1, \lambda_2, \lambda_3\}$, the chains rotate towards the direction of the highest stretch component, while the symmetry of the 8-chain arrangement guarantees that the junction point remains in the center of the unit cell. Consequently, all eight chains experience the same level of stretch defined by

$$\lambda = \sqrt{\frac{\lambda_1^2 + \lambda_2^2 + \lambda_3^2}{3}}. \quad (5.11)$$

The full three-dimensional stress-strain constitutive behavior of the eight chain-model is described in terms of a hyperelastic strain energy density W , which is differentiated with respect to the deformation gradient to obtain the associated Cauchy stress

$$\mathbf{T}^A = \frac{1}{J} \mu_0 \frac{\lambda_L}{\lambda} \beta (\mathbf{B}_c - \lambda^2 \mathbf{I}), \quad (5.12)$$

where μ_0 is the initial shear modulus and \mathbf{B}_c is the left Cauchy-Green stretch tensor defined as $\mathbf{B}_c = \mathbf{F}_c \mathbf{F}_c^T$.

Response of the Parenchyma

The response of the liver parenchyma is governed by the visco-elastic network (elements B, C, D, and E) under the deformation gradient \mathbf{F}_p . Given the arrangement of the constitutive elements of the rheological model, the numerical solution consists of satisfying the equations of equilibrium, the compatibility equations, and the individual constitutive relationships for each element. Here we provide the constitutive description of the individual elements governing the response of the parenchyma.

The short-time response of the parenchyma is governed by the reptation-based nonlinear viscous element C. The deviatoric stress \mathbf{T}^C driving the viscous element C is obtained from

$$\mathbf{T}^C = \mathbf{T}^A - \mathbf{T}^B. \quad (5.13)$$

$$\mathbf{T}^C = \mathbf{T}^C - \frac{1}{3} (\text{tr } \mathbf{T}^C) \mathbf{I}. \quad (5.14)$$

The viscous rate of stretch \mathbf{D}^C is prescribed to be proportional to the direction of the viscous stress deviator. The direction (\mathbf{N}^C) and magnitude (τ^C) of the deviatoric viscous stress are defined as

$$\mathbf{N}^C = \frac{\mathbf{T}'^C}{\sqrt{2}\tau^C} \quad (5.15)$$

$$\tau^C = \sqrt{\frac{1}{2}\mathbf{T}'^C : \mathbf{T}'^C}. \quad (5.16)$$

The viscous rate stretch is then expressed through a viscous strain-rate coefficient $\dot{\gamma}^v$

$$\mathbf{D}^C = \dot{\gamma}^v \mathbf{N}^C. \quad (5.17)$$

where the coefficient $\dot{\gamma}^v$ describes the reptation-based viscous shear strain-rate in a form adapted from Bergstrom and Boyce [14]

$$\dot{\gamma}^v = \dot{\gamma}_0^v \frac{\alpha^C}{\|\mathbf{F}_p\|_2 + \alpha^C} \left(\frac{\tau^C}{S^C} \right)^{m^C}, \quad (5.18)$$

where $\|\mathbf{F}_p\|_2$ is the magnitude (Frobenius norm) of the accumulated viscous deformation, α^C is the reptation coefficient controlling the flow-limiting behavior of the element, S^C is the shear strength modulus, m is the order of the viscous power law, and $\dot{\gamma}_0^v$ is the initial viscous strain-rate constant ($\dot{\gamma}_0^v = 0.01$) introduced for numerical stability reasons.

The response of the remaining elements (B, D, and E) is computed with an analogous approach. The Cauchy stress in the elastic element B is computed as

$$\mathbf{T}^B = 2G^B \mathbf{F}'_b. \quad (5.19)$$

where \mathbf{F}'_b is the deviatoric component of the deformation gradient $\mathbf{F}_b = \mathbf{F}_p (\mathbf{F}_{eq}^{-1})$ and G^B is the shear modulus. The Cauchy stress in the elastic element D is computed as

$$\mathbf{T}^D = 2G_{eq}^D \mathbf{F}'_{eq}, \quad (5.20)$$

where G_{eq}^D is the element's shear modulus and \mathbf{F}'_{eq} is the deviatoric component of $\mathbf{F}_{eq} = \mathbf{F}_p (\mathbf{F}_b^{-1})$. Finally, the linear viscous element capturing the long-time relaxation of the parenchyma is captured by the relationship between its viscous rate of stretch \mathbf{D}_{eq} and the direction of the viscous stress deviator \mathbf{N}^E

$$\mathbf{D}_{eq} = \eta^E \mathbf{N}^E, \quad (5.21)$$

where η^E is the linear viscosity coefficient and \mathbf{N}^E is computed analogously to the approach in eqn. 5.15.

Solution Approach

The response of the whole rheological network proposed in Figure 5.3 is obtained by numerical integration of the individual constitutive elements and their state variables. The time integration is initialized by assuming that the instantaneous response is entirely accommodated by the response of the collagen matrix. Therefore, the initial value conditions ($t = 0$) prescribe $\mathbf{F}_c = \mathbf{F}_d$. The deformation gradients associated with the viscous components of the model (\mathbf{F}_p and \mathbf{F}_{eq}) and their corresponding Cauchy stress (\mathbf{T}^C and \mathbf{T}^E) are assumed to have zero initial state and are subsequently integrated according to the evolution of the differential equations governing the response of the whole network. The time integration of the model response to the deviatoric component F_d of the prescribed deformation gradient may be summarized as

1. Compute $\mathbf{F}_c[t] = \mathbf{F}_d[t] (\mathbf{F}_p[t]^{-1})$
2. Compute $\mathbf{F}_b[t] = \mathbf{F}_p[t] (\mathbf{F}_{eq}[t]^{-1})$
3. Compute the elastic stress $\mathbf{T}^A[t]$ from the current deformation gradient $\mathbf{F}_c[t]$
4. Compute the back stress $\mathbf{T}^B[t]$ from the current deformation gradient $\mathbf{F}_b[t]$
5. Compute the long-term back stress $\mathbf{T}^D[t]$ from the current deformation gradient $\mathbf{F}_{eq}[t]$
6. Compute the plastic stress $\mathbf{T}^C[t] = \mathbf{T}^A[t] - \mathbf{T}^B[t]$
7. Compute the long-term plastic back stress $\mathbf{T}^E[t] = \mathbf{T}^B[t] - \mathbf{T}^D[t]$
8. Evolve $\mathbf{F}_p[t + \Delta t]$ by integrating $\mathbf{F}_p[t]$ according to the current Cauchy stress $\mathbf{T}^C[t]$ experienced by element C
9. Evolve $\mathbf{F}_{eq}[t + \Delta t]$ by integrating $\mathbf{F}_{eq}[t]$ according to the current Cauchy stress $\mathbf{T}^E[t]$ experienced by element E
10. The computed Cauchy stress in element A due to the deformation gradient $\mathbf{F}_c[t]$ is equivalent to the total stress state of the model at time t

5.2.3 Mesh Convergence

The accuracy of the numerical solution is dependent on various factors, such as the size of the time integration steps as well as the spatial discretization (meshing) of the model geometry. Figure 5.4 demonstrates three meshes with increasing density (173 elements, 719 elements, and 3250 elements) composed of axisymmetric quadratic triangular elements (CAX6). We evaluated the mesh convergence on a single 2 mm/s

indentation simulation (30 mm height, 10 mm indentation depth). The resulting forces vs. time output of the simulation is shown in Figure 5.5, demonstrating that meshes with density comparable to mesh #2 are appropriate for our application. While the difference between the numerical solutions produced by mesh #2 and mesh #3 are negligible, the computation run times were six times longer for mesh #3.

5.2.4 Internal Deformation Field Estimation

The estimation of the internal deformation field of the organ provides a valuable insight in the three-dimensional response of the tissue. As demonstrated in Chapter 4, the volumetric imaging approach offers means for estimation of material parameters which are not directly observable in conventional indentation. Most notably, the bulk modulus K can be properly constrained with volumetric data. Additionally, the volumetric data captures the tissue response at various local strain rates (strain rates diminish with distance from the indenter). Therefore, even a single indentation performed at one indenter displacement velocity can provide information about the strain-rate dependence of the material. This information is especially valuable for constitutive laws with nonlinear viscous components, such as the reptation-limited power law employed in this study.

To estimate the internal deformation fields of the organ during indentation testing, we follow the methods described in Chapter 3, relying on a modified implementation of the Lucas-Kanade [84, 10] optical flow algorithm. The discretization of the image space is performed by a tetrahedral mesh (shown in Figure 5.6), where the mesh elements and their elemental shape functions serve as the local image neighborhoods. The mesh is registered to the 3DUS volume by manually aligning the top surface of the liver parenchyma and the circular cross-section of the indenter. The displacement of individual mesh nodes is obtained by solving the least-squares solution of the optical flow equations for each voxel in the local neighborhood. The confidence of each local motion estimate is quantified by the local textural quality (local image gradient). Further details and performance evaluation of this method may be found in Chapter 3.

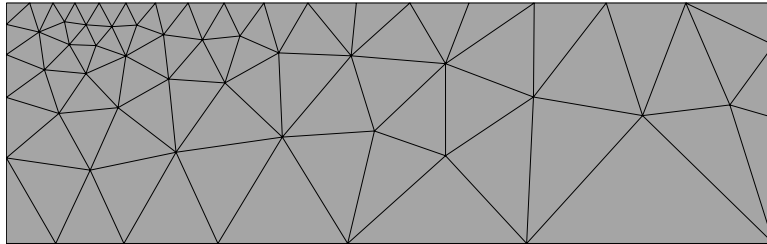
While the optical flow discretization relies on a three-dimensional tetrahedral mesh, the computational model is an axisymmetric implementation for computational efficiency. To relate the image-based internal displacements, the nodal velocity histories are mapped from cartesian $\{x, y, z\}$ space to the coordinate system of the axisymmetric model $\{r_{axi}, z_{axi}\}$ as

$$r_{axi} = \sqrt{x^2 + y^2} \quad (5.22)$$

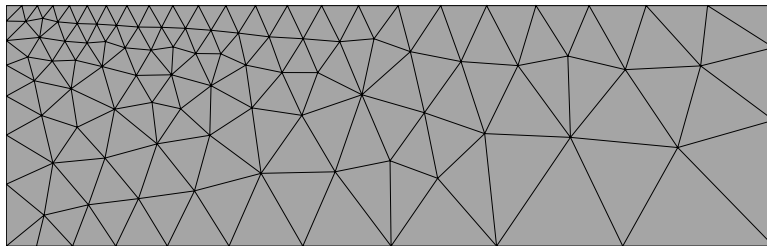
and

$$z_{axi} = z. \quad (5.23)$$

Mesh #1



Mesh #2



Mesh #3

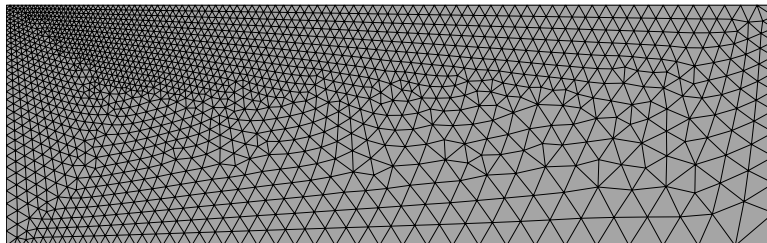


Figure 5.4: Three axisymmetric quadratic triangular (CAX6) meshes of increasing density (173 elements, 719 elements, and 3250 elements) used to evaluate the dependence of the solution accuracy on the mesh density.

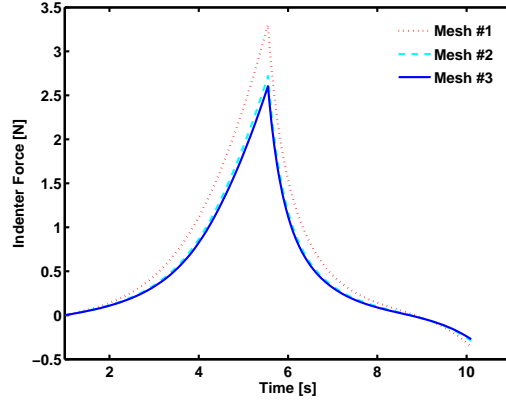


Figure 5.5: Mesh convergence study showing indentation force predicted by finite-element models using meshes #1, #2, and #3 (meshes shown in Figure 5.4).

The image-based velocities can then be directly compared to the simulated response of the organ model.

5.2.5 Material parameter estimation

We rely on iterative inverse modeling to identify the model material parameters. Using the bounded downhill simplex method [76], we iteratively adjust material parameters until the error between the experimental and model response is minimized. Given the number of measurement modalities involved in the experimental protocol, the total objective function is defined as a sum of the errors in indentation sequence block (Φ_{block}), the stress-relaxation response (Φ_{SR}), and the image-based volumetric tissue response during a 2 mm/s indentation (Φ_{im}). The components of the objective function relying on the time-displacement-force relationship of the indenter are defined as normalized mean-squared error (MSE) between the experimental ($F^{exp}(t)$) and modeled ($F^{model}(t)$) indentation force history. The model response is resampled using linear interpolation at time indices coinciding with the experimental force history. While initially obtained at 1000Hz, the experimental data is resampled offline to 100Hz. To maintain dimensional homogeneity between the three error terms (to maintain comparable importance of each term), we normalize the force history terms by the peak force and the internal deformation fields are normalized by the prescribed velocity of the indenter. The force history error measures (Φ_{block} and Φ_{SR}) are defined as

$$\Phi_{block}(p_n) = \frac{1}{\max(F_{block}^{exp})N} \sum_{i=1}^N (F_{block}^{exp}[i] - F_{block}^{model}[i])^2 \quad (5.24)$$

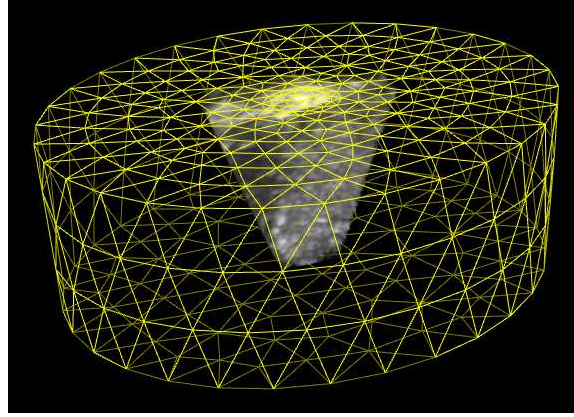


Figure 5.6: 3DUS sequence (gray) is registered to a tetrahedral three-dimensional mesh (yellow), which is used to discretize the image space for the local optical flow algorithm. The elemental shape functions are used as local neighborhood weights.

and

$$\Phi_{SR}(p_n) = \frac{1}{\max(F_{SR}^{exp})M} \sum_{i=1}^M (F_{SR}^{exp}[i] - F_{SR}^{model}[i])^2, \quad (5.25)$$

where N and M are the number of samples in the experimental force history signals. The image-based model agreement is expressed in terms of the MSE between the internal velocity fields of the model ($\dot{\mathbf{u}}^{model}$) and the experiment ($\dot{\mathbf{u}}^{exp}$) as

$$\Phi_{im}(p_n) = \frac{1}{v^{exp}LP} \sum_{k=1}^L \sum_{i=1}^P \sum_j \mathbf{c}_{j,k}[i] (\dot{\mathbf{u}}_{j,k}^{exp}[i] - \dot{\mathbf{u}}_{j,k}^{model}[i])^2, \quad (5.26)$$

where $j = \{x, y, z\}$, P is the number of experimental time frames (image data is acquired at 25 Hz), L is the number of local image motion estimates/neighborhoods, v^{exp} is the normalization factor corresponding to the prescribed velocity of the indenter (0.002 m/s), and \mathbf{c}_i is the confidence of the local optical flow estimate (see Chapter 3 for implementation details). The total error function is defined as

$$\Phi_{total}(p_n) = \alpha_1 \Phi_{block}(p_n) + \alpha_2 \Phi_{SR}(p_n) + \alpha_3 \Phi_{im}(p_n), \quad (5.27)$$

where parameters α_1 , α_2 , and α_3 determine the relative weights of the error function components. The choice of the weighting between the individual error terms is dependent on the amount of information contained in the specific experiments and the perceived importance of each experimental component. For example, considering the significant amount of information regarding the material response across multiple

strain rates contained in the indentation block data, its corresponding weight coefficient (α_1) may need to be relatively high to ensure close fits to this component of the experimental data. It is necessary to ensure that the choice of α_1 does not dominate the total error function and that satisfactory fits are maintained in the stress relaxation and volumetric response tests. Under these considerations, the weighting coefficients in this study were determined to be: $\alpha_1 = 2$, $\alpha_2 = 1$, and $\alpha_3 = 1$.

5.3 Results

Imaging the Internal Tissue Deformation

The volumetric data containing the internal tissue displacements was acquired during 2 mm/s indentation tests in each specimen. The indenter force-time and displacement-time signals are shown with two-dimensional cross-section through the corresponding 3DUS sequence. See Figures 5.7, 5.8, and 5.9 for the image-data synchronized with the conventional indentation outputs. The liver parenchyma produces rich textural pattern, which results in good tracking accuracy of the optical flow algorithm (see Chapter 3 for performance evaluation). In indentation sequences performed at the rate of 2 mm/s, the frame-to-frame tissue displacements are on the sub-voxel scale and do not suffer from the large displacement limitations of differential optical flow methods. The contact surfaces of the indenter can be clearly seen in the images, however in some instances local reverberation artifacts may be observed (see Figure 5.8).

Model Fitting

Tissue models reflecting experimental geometry and boundary conditions were fitted to three perfused porcine liver specimens, following the material parameter estimation method described in section 5.2.5. The model fits reflect the material parameters, which minimize the model-experiment error for the repeated indentation cycles, conventional stress-relaxation tests, as well as internal tissue displacement obtained with 3D ultrasound. Figures 5.10, 5.11, and 5.12 show the model fits to the repeated indentation cycles performed on liver specimens 1, 2, and 3, respectively. It may be observed that the model, in all three cases, provides excellent agreement with experimental data across the broad range of strain rates tested. Additionally, the model is capable of accommodating for the complex time-dependent pre-conditioning effects, which make the experimental data strongly dependent on the testing history. For instance, the experimental forces obtained from the 40 mm/s cycles in liver 1 have smaller magnitude than the magnitude of the response to the 20 mm/s cycles, which immediately precede the 40 mm/s cycles. This counter-intuitive response of the tissue can be explained by the pre-conditioning effects mediated by the displacement of the local fluid and relatively long time constant governing the refill and recovery

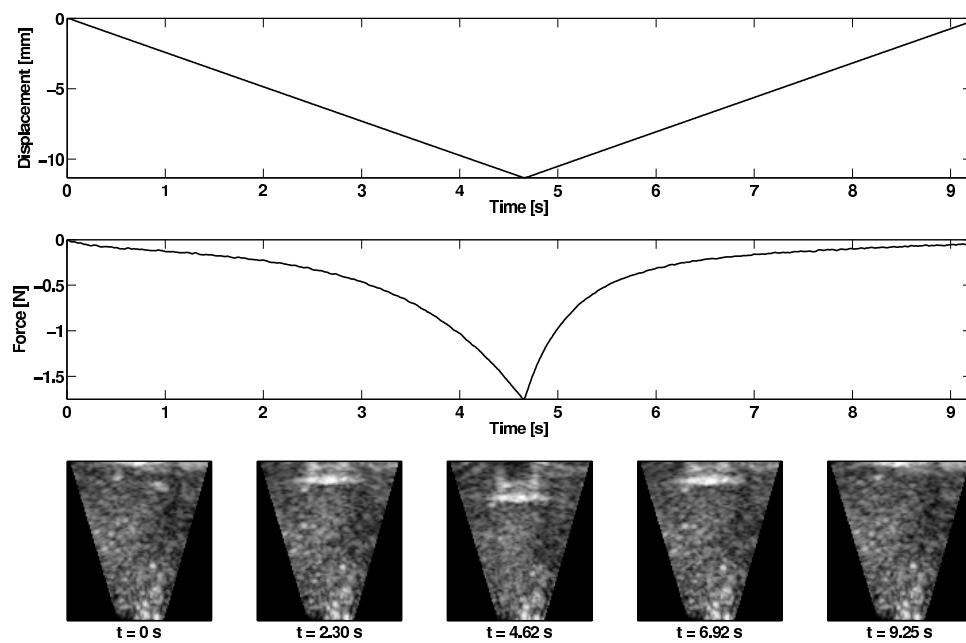


Figure 5.7: Liver 1: indentation displacement and force histories along with a 2D slice through the corresponding 3DUS sequence capturing internal organ deformation field.

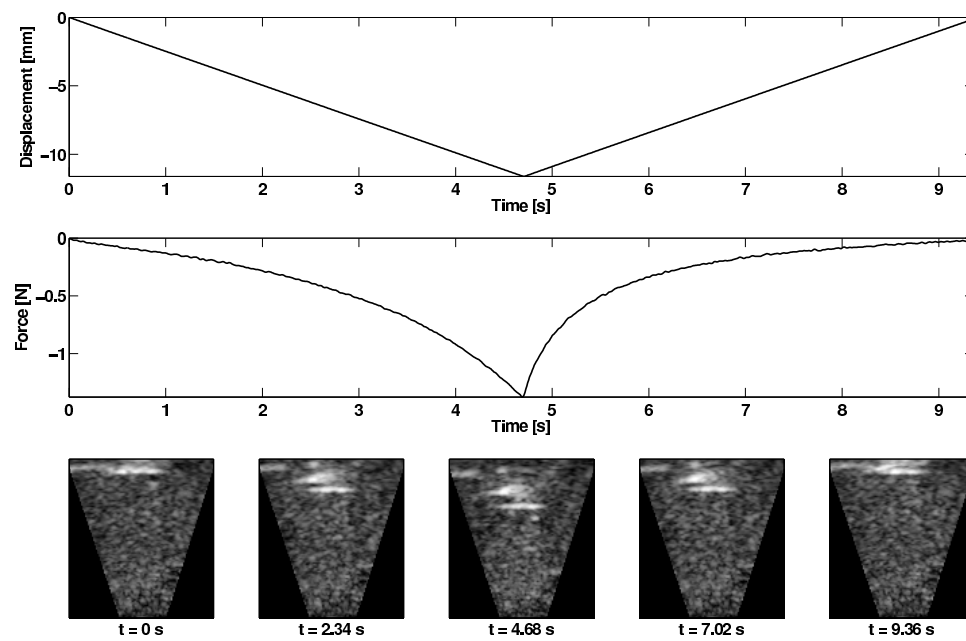


Figure 5.8: Liver 2: indentation displacement and force histories along with a 2D slice through the corresponding 3DUS sequence capturing internal organ deformation field.

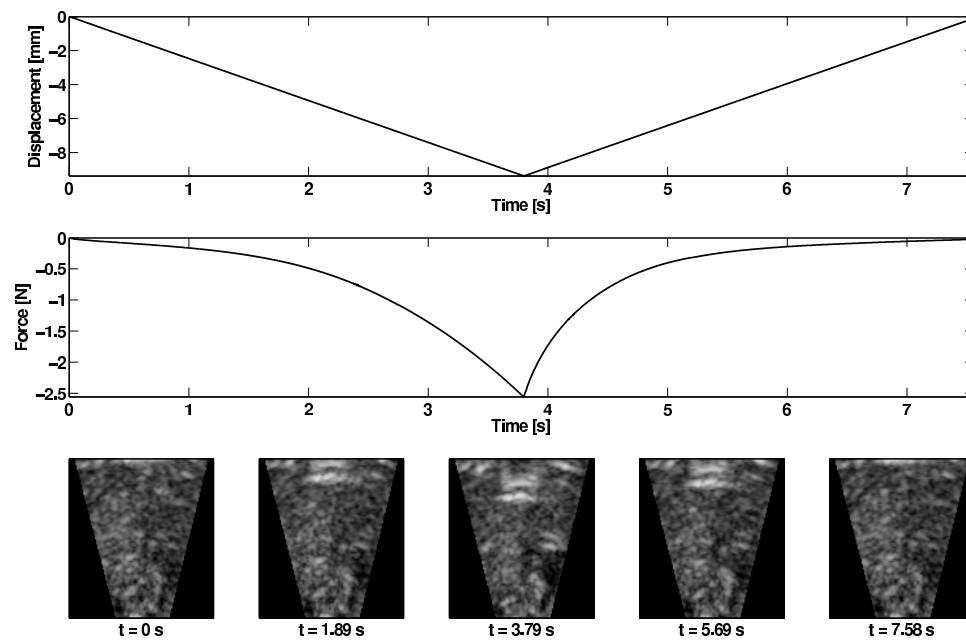


Figure 5.9: Liver 3: indentation displacement and force histories along with a 2D slice through the corresponding 3DUS sequence capturing internal organ deformation field.

of the tissue. The proposed model is capable of accounting for this effect through the reptation-limited nonlinear viscous element proposed by Bergstrom and Boyce (2001) [14].

The models were concurrently fitted to the stress relaxation experiments and show good agreement with this alternative loading history. The stress relaxation tests are fundamentally different from cyclic loading as they test both the response at the very short time-scale as well as the long-time equilibrium response.

The third experimental data source that the model is concurrently fitted to is the internal deformation field of the organ obtained by real-time 3D ultrasound imaging. This data offers rich information regarding the volumetric, time-dependent response of the organ. Most importantly, the measurement of the internal deformation field allows for overcoming the material parameter ambiguities due to the inherent coupling between the bulk and shear components of the material response. The benefits of image-based parameter identification were demonstrated in Chapter 4, where we have shown that material parameters that the bulk modulus, a parameter not directly observable in conventional indentation, can be accurately and reliably estimated with the proposed image-based inverse modeling approach.

The agreement between the internal velocity field of the liver specimens and their corresponding models is illustrated in Figures 5.19, 5.20, and 5.21, showing the vertical (dominant) component of the velocity field at various mesh node location throughout the organ volume. The results demonstrate that the models offer good agreement, within the measurement accuracy of the imaging method, throughout the field beneath the indenter.

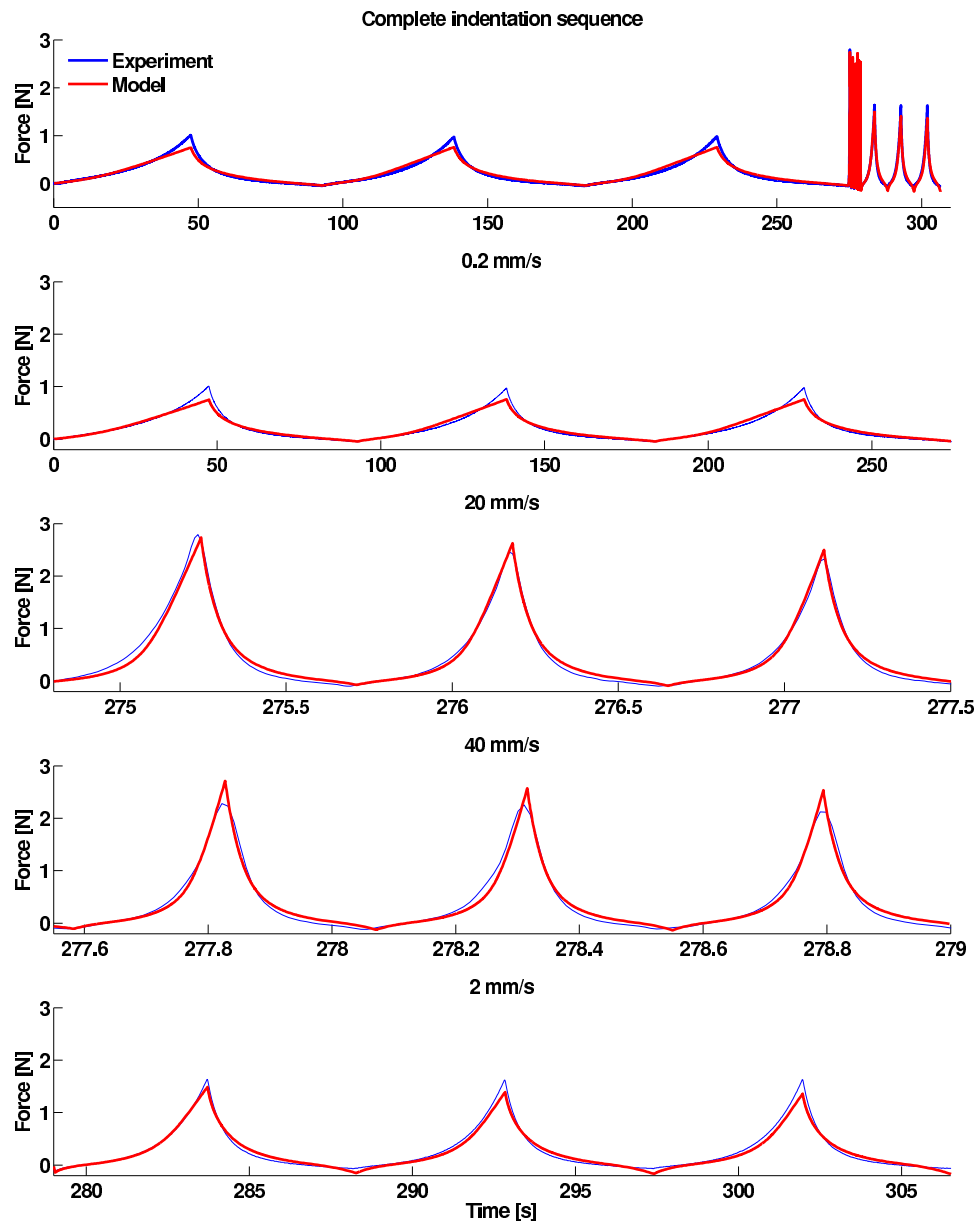


Figure 5.10: Liver 1: indentation sequence (3×0.2 mm/s, 3×20 mm/s, 3×40 mm/s, 3×2 mm/s) and the corresponding model fit. The full sequence is shown in the top plot. Subsections of the sequence separated by indentation rate are shown in the remaining plots.

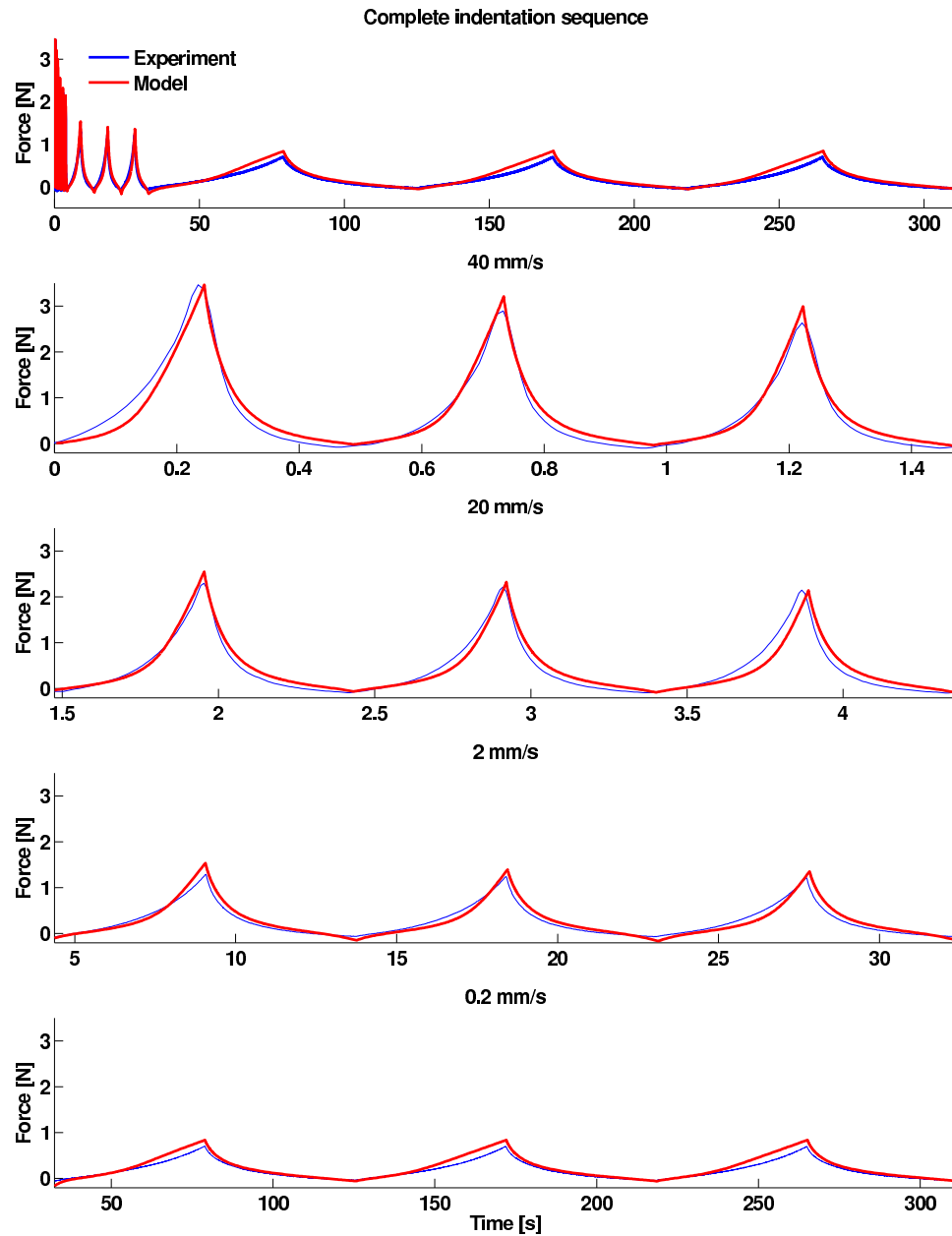


Figure 5.11: Liver 2: indentation sequence (3×40 mm/s, 3×20 mm/s, 3×2 mm/s, 3×0.2 mm/s) and the corresponding model fit. The full sequence is shown in the top plot. Subsections of the sequence separated by indentation rate are shown in the remaining plots.

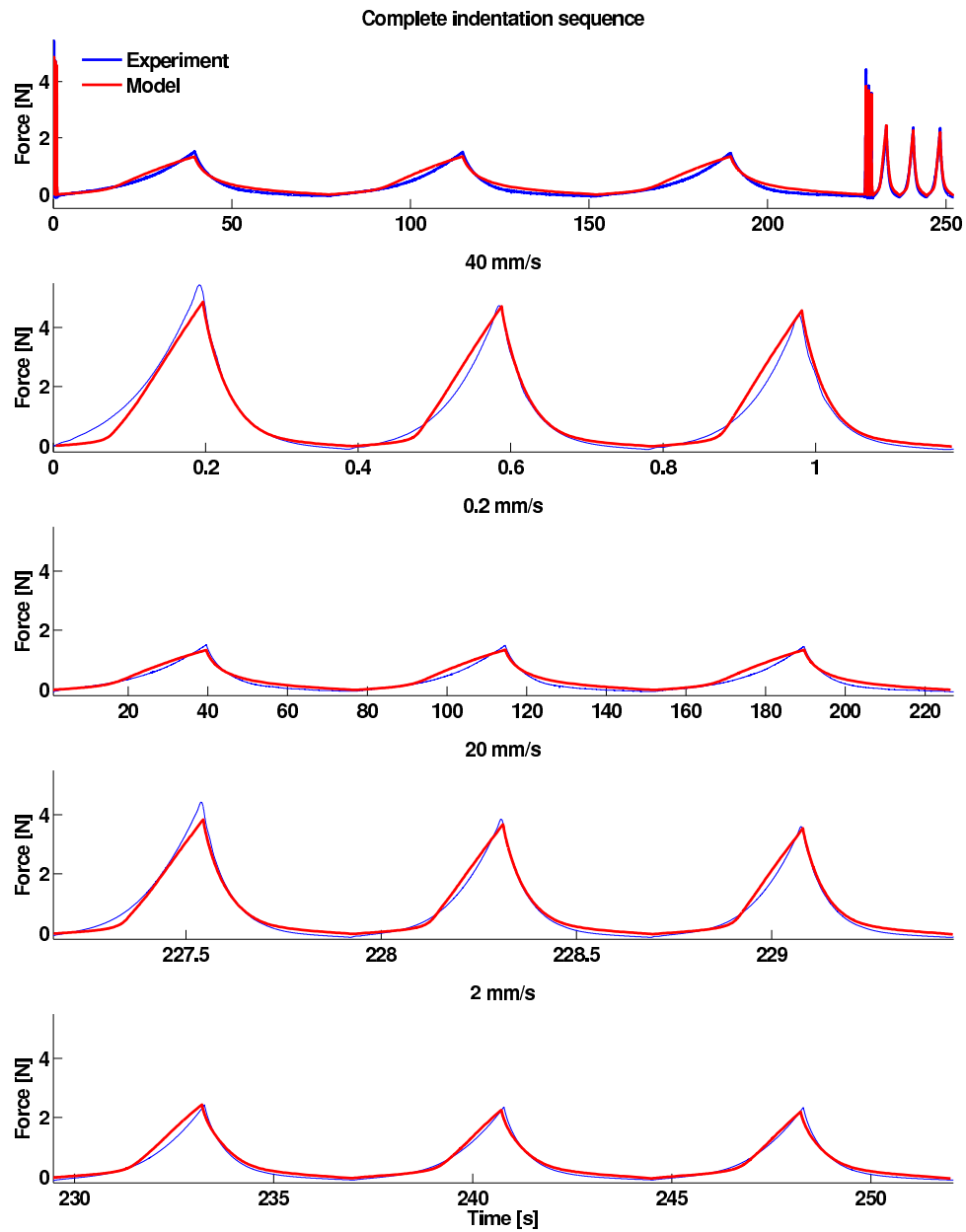


Figure 5.12: Liver 3: indentation sequence (3×40 mm/s, 3×0.2 mm/s, 3×20 mm/s, 3×2 mm/s) and the corresponding model fit. The full sequence is shown in the top plot. Subsections of the sequence separated by indentation rate are shown in the remaining plots.

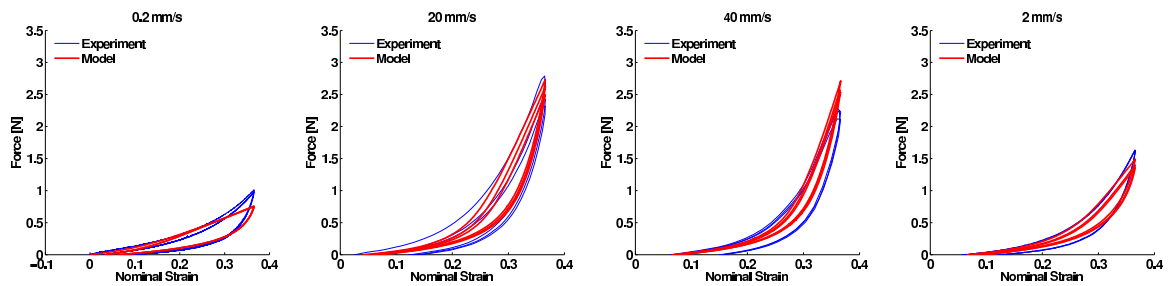


Figure 5.13: Liver 1: indentation sequence (experimental response and model prediction) separated into individual displacement rates plotted as nominal strain vs. indenter force.

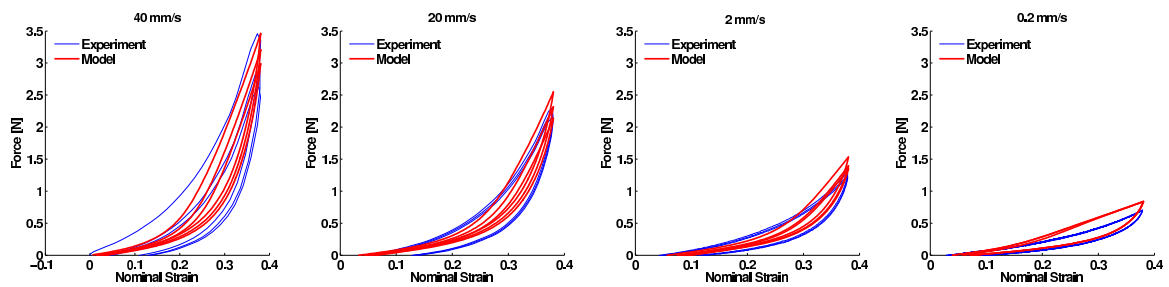


Figure 5.14: Liver 2: indentation sequence (experimental response and model prediction) separated into individual displacement rates plotted as nominal strain vs. indenter force.

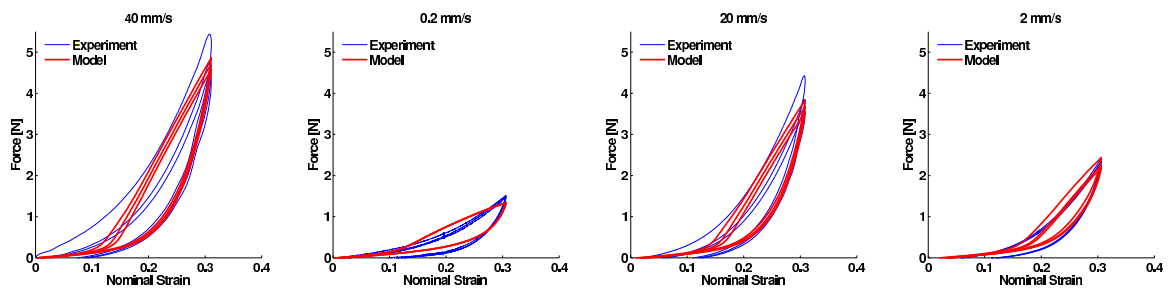


Figure 5.15: Liver 3: indentation sequence (experimental response and model prediction) separated into individual displacement rates plotted as nominal strain vs. indenter force.

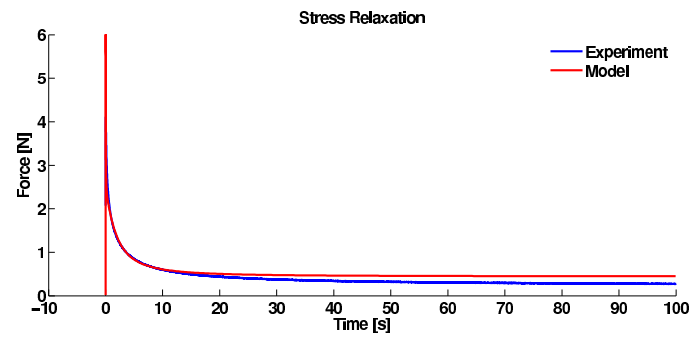


Figure 5.16: Liver 1: experimental stress relaxation and model fit.

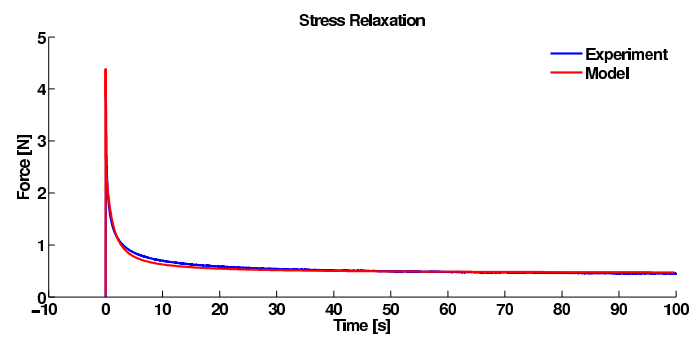


Figure 5.17: Liver 2: experimental stress relaxation and model fit.

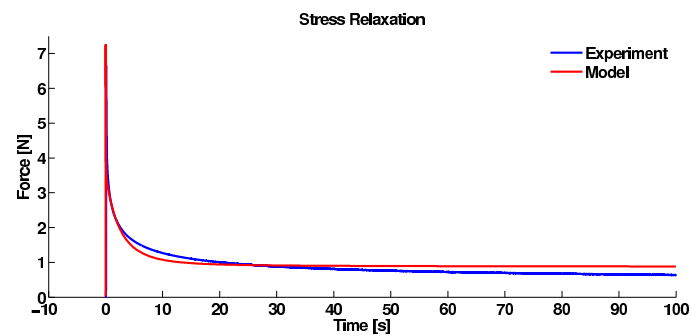


Figure 5.18: Liver 3: experimental stress relaxation and model fit.

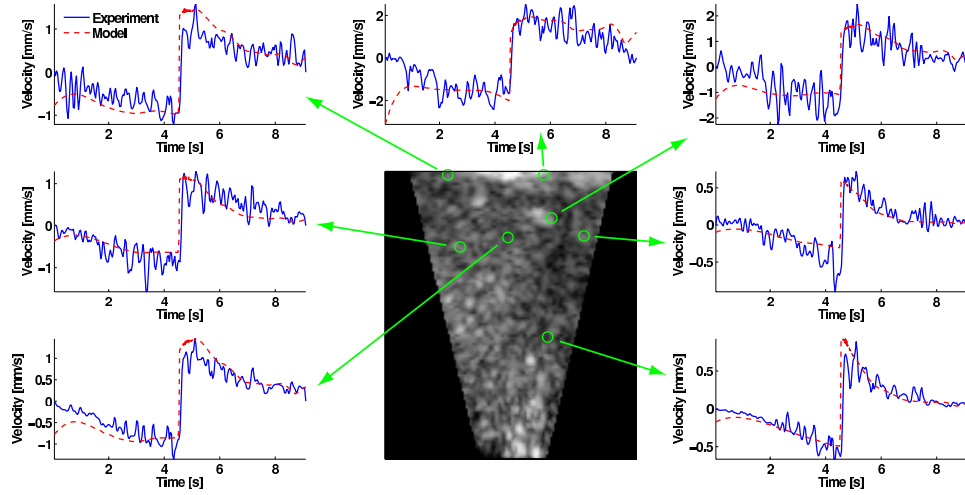


Figure 5.19: Liver 1: measured and predicted vertical component of the internal velocity field fit evaluated and various locations within the organ).

Table 5.3: Estimated material parameters for the three liver specimens.

| | μ_0^A [Pa] | λ_L^A | G^B [Pa] | m^C | S^C [Pa] | α^C | G_{eq}^D [Pa] | η^E [Pa.s] | K [Pa] |
|----------------|----------------|---------------|------------|-------|------------|------------|-----------------|-----------------|----------|
| Liver 1 | 8.93 | 1.023 | 16,275 | 1.197 | 28.92 | 0.100 | 1,056 | 31,673 | 26,569 |
| Liver 2 | 19.0 | 1.041 | 24,214 | 1.80 | 146.53 | 0.133 | 1,234 | 21,329 | 19,542 |
| Liver 3 | 16.76 | 1.043 | 29,472 | 1.62 | 105.47 | 0.089 | 4,636 | 83,950 | 28,001 |

5.3.1 Sensitivity Analysis

Given the high-dimensional nature of the parameter space, it is important to investigate the issues pertinent to understanding the properties of the objective function hypersurface. It is important to evaluate the optimization method's sensitivity to the individual material parameters. We evaluate the parameters sensitivity by local perturbation of the best fits of each liver specimen. While not fully comprehensive, this approach provides an insight into the local shape of the objective function and gauges the confidence in the estimated material parameters.

The sensitivity of each parameter (p_i) is measured as the curvature of a quadratic polynomial function,

$$\zeta(p_i) = ap_i^2 + bp_i + c, \quad (5.28)$$

fitted to the objective function surface along the parameter axis. See Figure 5.22 for

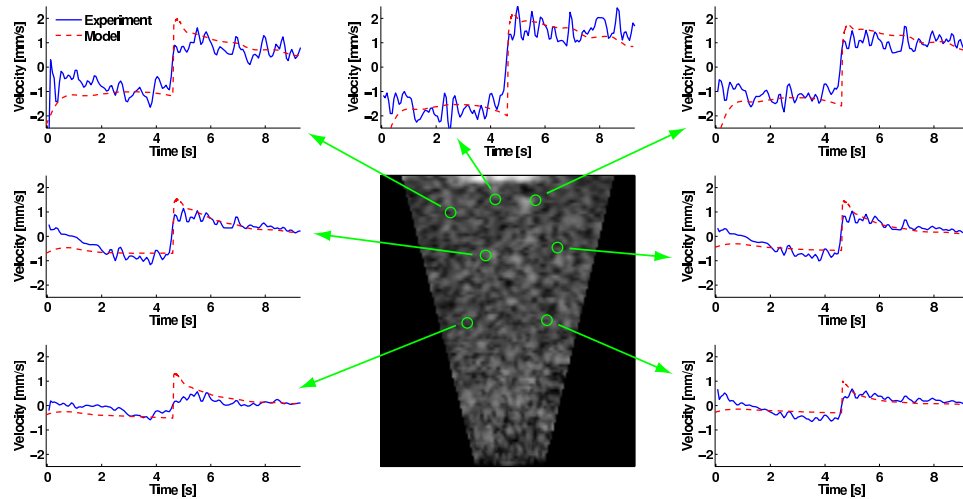


Figure 5.20: Liver 2: measured and predicted vertical component of the internal velocity field fit evaluated and various locations within the organ).

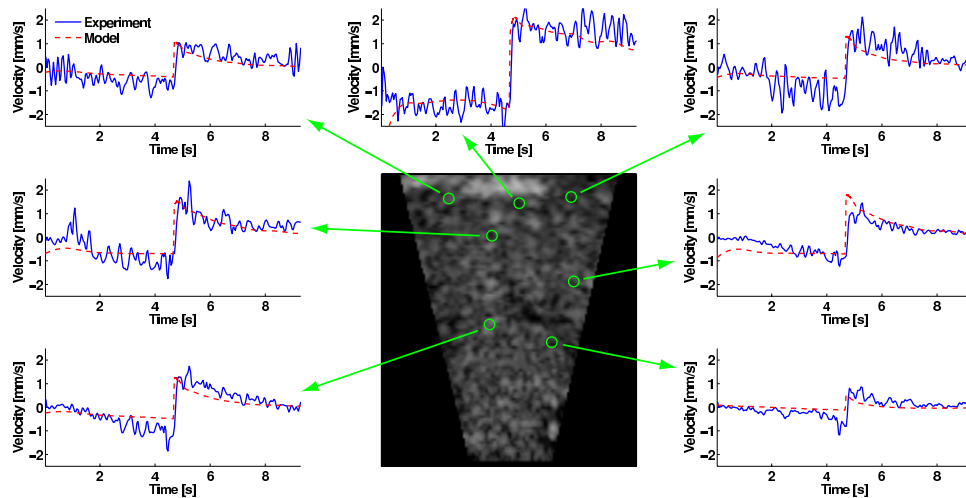


Figure 5.21: Liver 3: measured and predicted vertical component of the internal velocity field fit evaluated and various locations within the organ).

quadratic polynomial fits to the objective function surface for liver #1. The curvature of the polynomial is computed as

$$k(p_i) = \frac{\frac{\partial^2 \zeta}{\partial p_i^2}}{\left[1 + \left(\frac{\partial \zeta}{\partial p_i}\right)^2\right]^{3/2}} = \frac{2a}{(1 + (2ap_i + b)^2)^{3/2}}. \quad (5.29)$$

The sensitivity of the objective function to each parameter in the vicinity of the best model fit to each liver specimen is summarized in Table 5.4.

5.3.2 Validation

The model's predictive capability is evaluated in a validation study in which the model is subjected to alternative cyclic loading histories. The results predicted by the model are illustrated in Figure 5.23, 5.24, and 5.25. In all three simulations, the model demonstrates satisfactory agreement with the experimental data, although not as good as with the primary sequences that the model was fitted to. The discrepancies between the model prediction and the experimental data can most likely be attributed to the aforementioned complex preconditioning effects in consecutive cyclic loading tests and the long period of time (approximately 30 minutes) between the experimental sequences.

5.4 Discussion

The main objective of this work was to develop an accurate, physically motivated liver model, suitable for applications in surgical simulation and image-guided procedures. In these scenarios, the model must predict organ response across a wide range of frequencies. This was achieved by a nonlinear visco-elastic constitutive law, previously identified as the simplest configuration for the given application, as well as an extensive experimental testing protocol. The testing methods relied on conventional indentation testing, spanning strain-rates over two orders of magnitude, along with image-based measurement of the organ's internal deformations.

An earlier study by Nava et al. [96] identified parameters of human liver in small-displacement aspiration tests using single-rate repeated tests, using a 6-parameter quasilinear viscoelastic (QLV) model and a 14-parameter Rubin-Bodner model [109]. The study by Nava et al. [96] is unprecedented in the sense that it uses human *in vivo* liver data and determines material parameters via inverse finite-element modeling. In comparison, the work proposed in this work uses *ex vivo* perfused porcine liver, however the 9-parameter model and the tissue testing methodology offer the following benefits: (i) it accurately captures the large deformation response of the liver tissue (over 30% nominal strain); (ii) it uses concurrent full-field volumetric data to

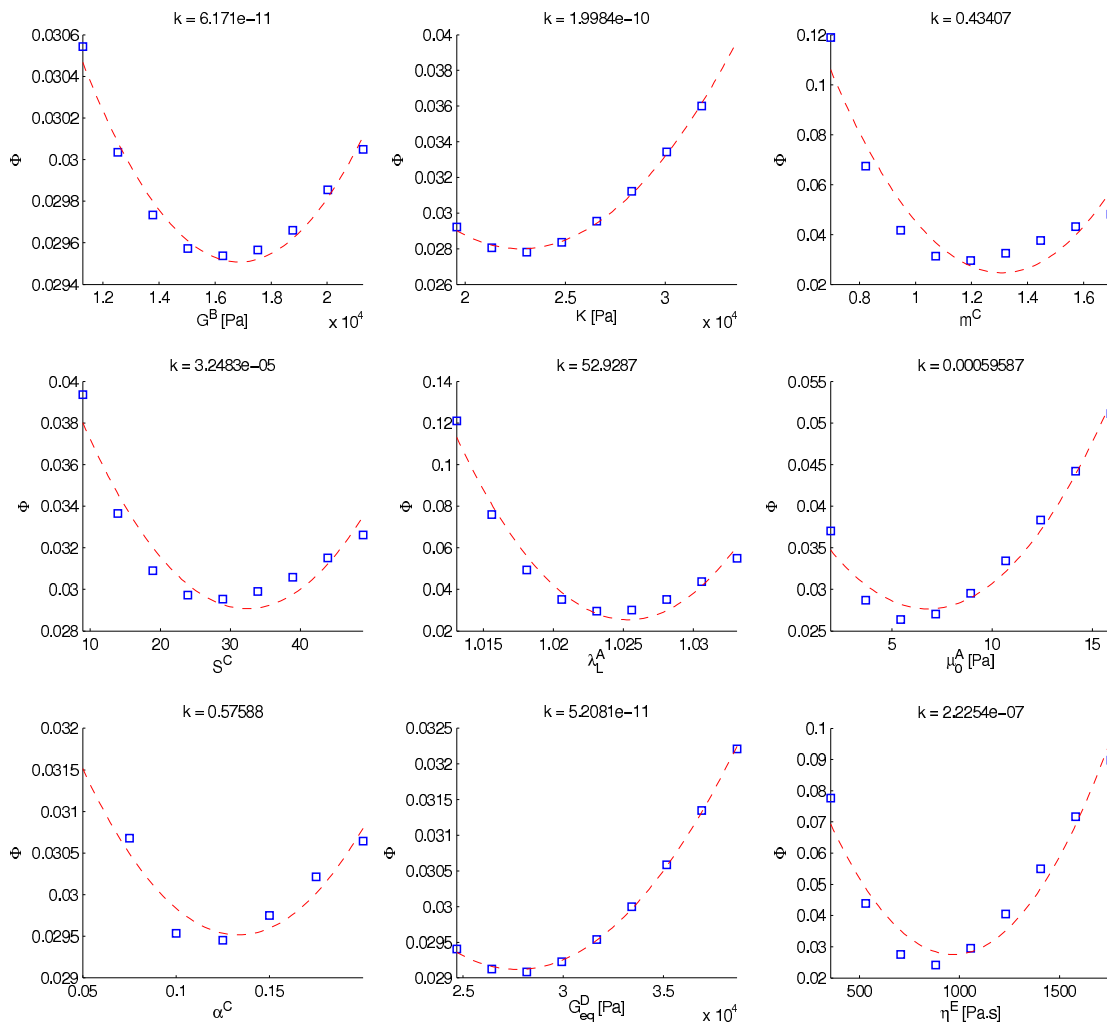


Figure 5.22: Liver 1: parameter sensitivity analysis measured as the curvature of a quadratic function fitted to a cut through the objective space along each parameter axis.

Table 5.4: Parameter sensitivity measured as the curvature of a quadratic function fitted to a cut through the objective space along each parameter axis.

| | μ_0^A | λ_L^A | G^B | m^C | S^C | α^C | G_{eq}^D | η^E | K |
|----------------|-----------------------|--------------------|------------------------|-----------------------|-----------------------|-----------------------|------------------------|-----------------------|------------------------|
| Liver 1 | 5.96×10^{-4} | 5.29×10^1 | 6.17×10^{-11} | 4.34×10^{-1} | 3.25×10^{-5} | 5.76×10^{-1} | 5.21×10^{-11} | 2.23×10^{-7} | 2.00×10^{-10} |
| Liver 2 | 1.78×10^{-3} | 3.02×10^3 | 4.50×10^{-10} | 2.32×10^0 | 1.08×10^{-5} | 2.80×10^1 | 8.27×10^{-10} | 1.63×10^{-7} | 4.09×10^{-9} |
| Liver 3 | 6.60×10^{-4} | 5.11×10^2 | 1.28×10^{-9} | 1.64×10^0 | 3.76×10^{-4} | 4.43×10^1 | 1.33×10^{-9} | 4.48×10^{-8} | 3.70×10^{-9} |

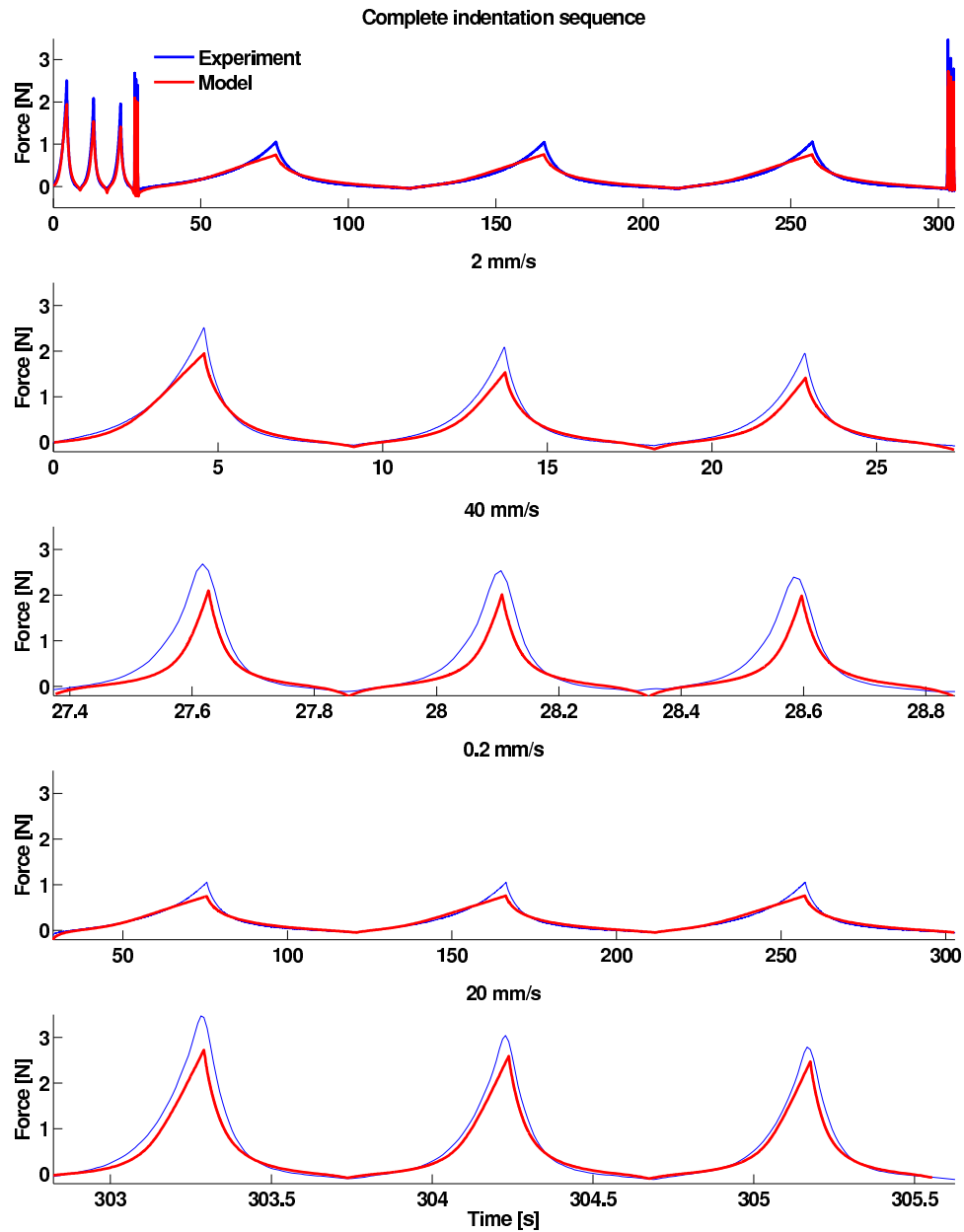


Figure 5.23: Liver 1: using the estimated material parameters, the predictive ability of the model is evaluated by comparing its response to an alternative loading history (3×2 mm/s, 3×40 mm/s, 3×0.2 mm/s, 3×20 mm/s).

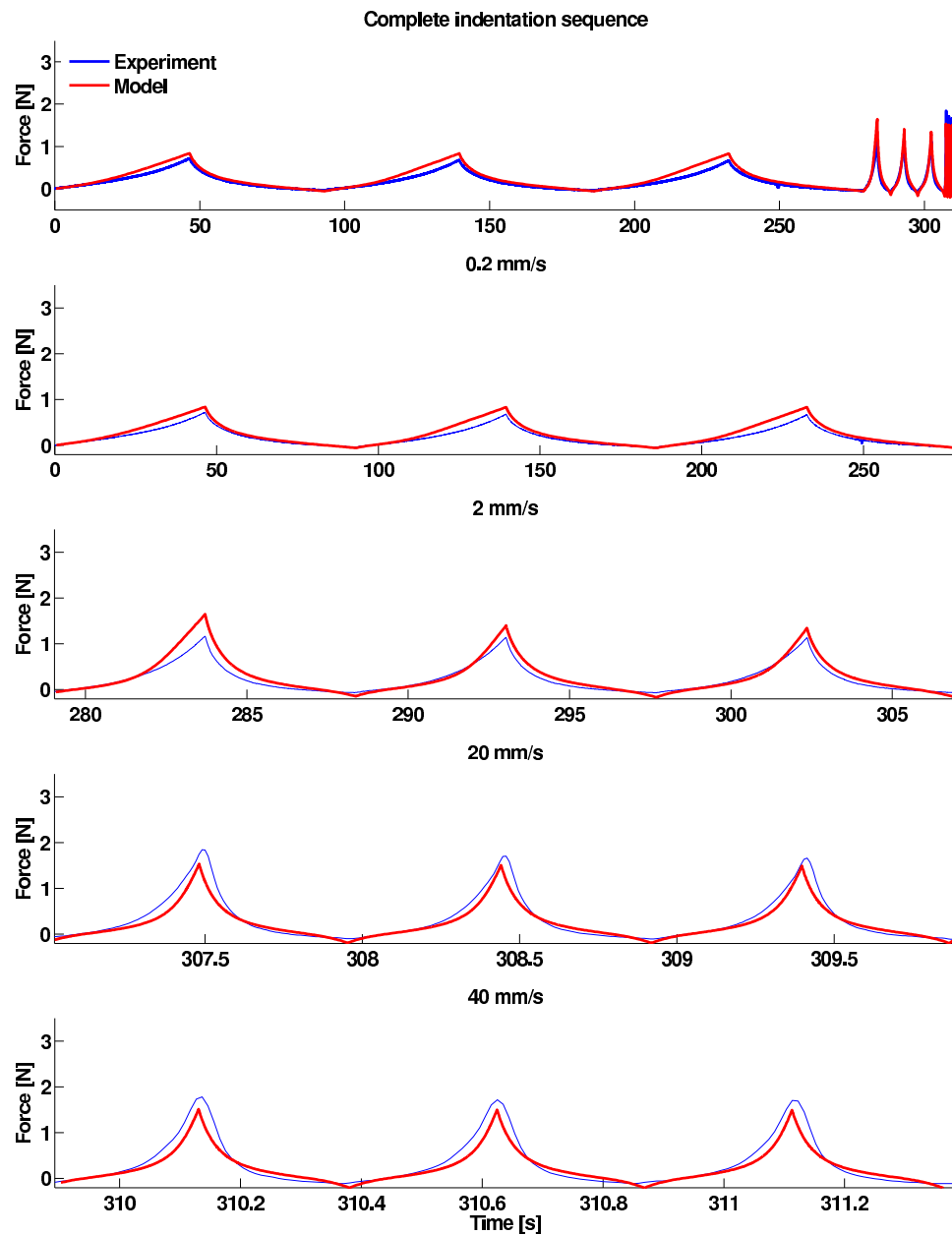


Figure 5.24: Liver 2: using the estimated material parameters, the predictive ability of the model is evaluated by comparing its response to an alternative loading history (3×0.2 mm/s, 3×2 mm/s, 3×20 mm/s, 3×40 mm/s).

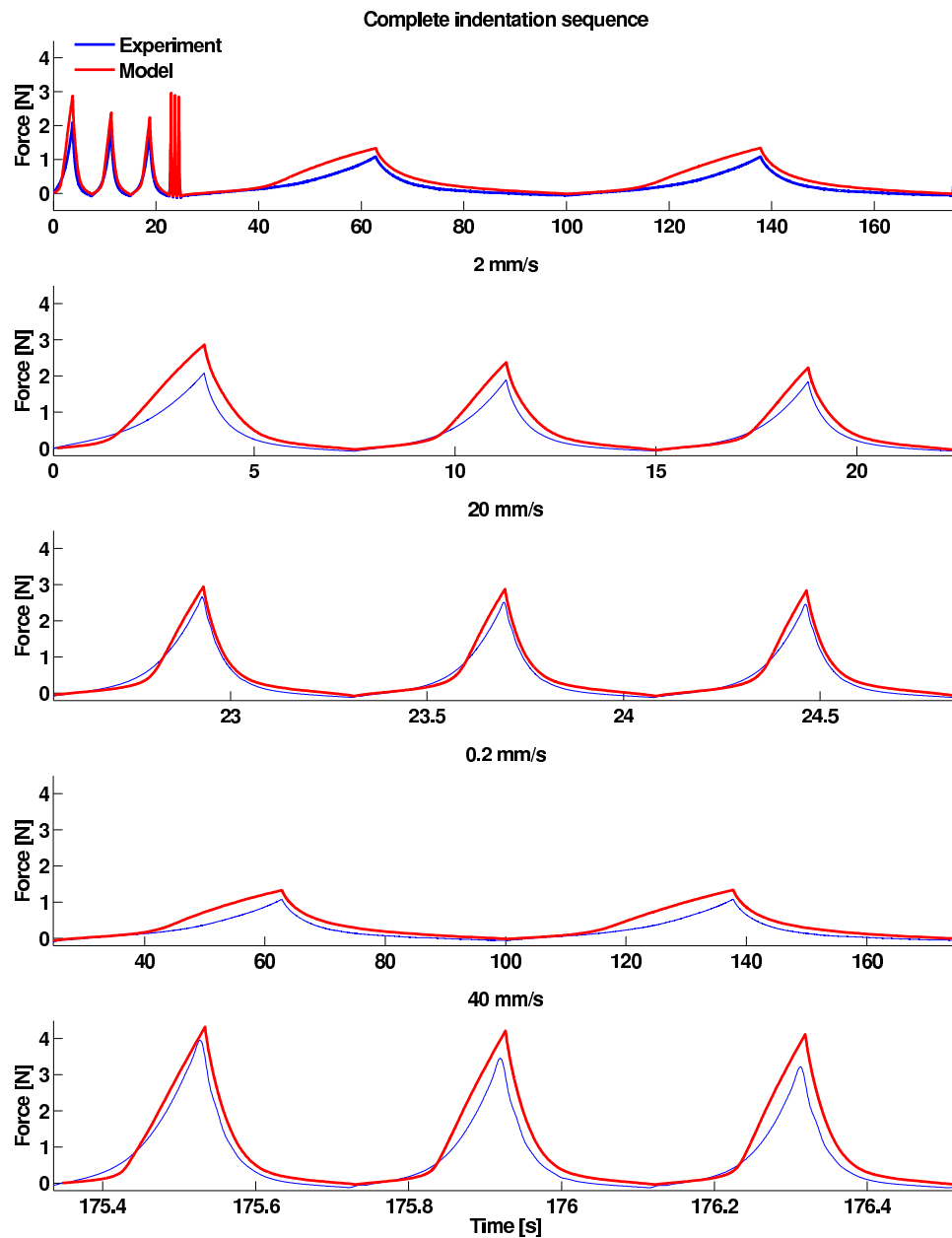


Figure 5.25: Liver 3: using the estimated material parameters, the predictive ability of the model is evaluated by comparing its response to an alternative loading history (3×2 mm/s, 3×20 mm/s, 2×0.2 mm/s, 3×40 mm/s).

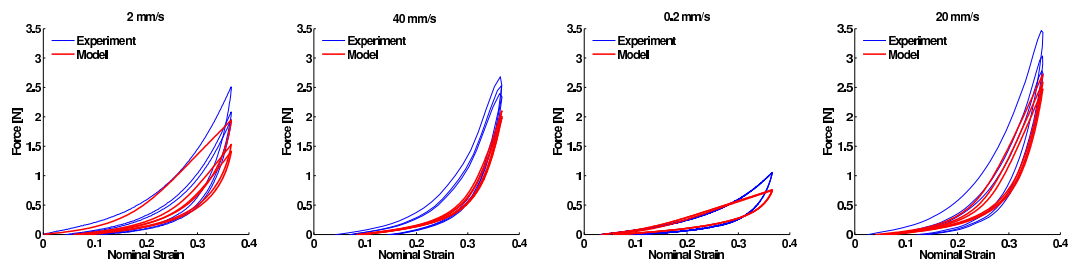


Figure 5.26: Liver 1: indentation cycles from alternative loading history separated into individual indenter displacement rates.

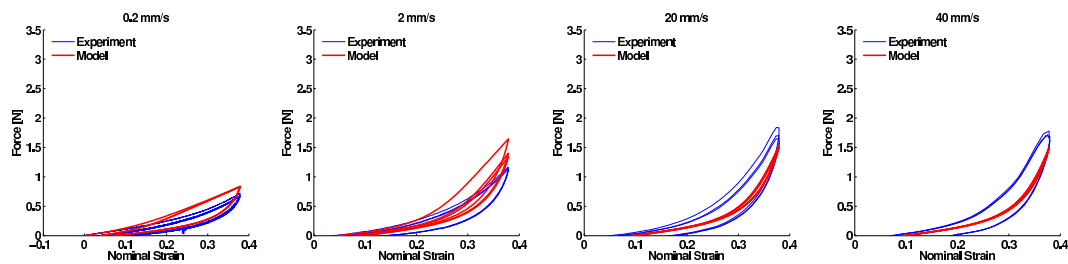


Figure 5.27: Liver 2: indentation cycles from alternative loading history separated into individual indenter displacement rates.

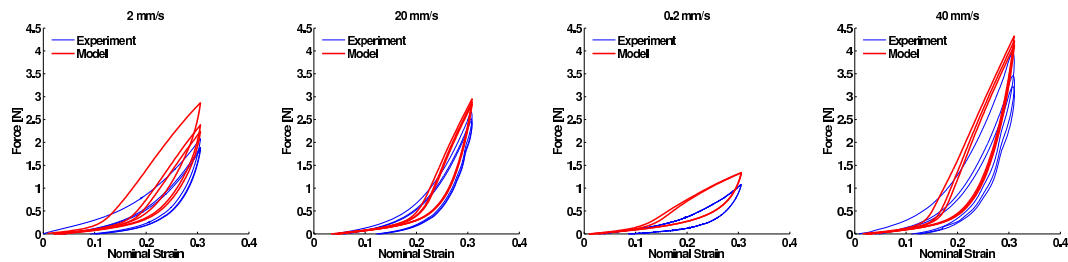


Figure 5.28: Liver 3: indentation cycles from alternative loading history separated into individual indenter displacement rates.

characterize and decouple the shear and bulk compliance components of the tissue response; (iii) it captures the viscoelastic tissue response across two orders of strain rate magnitude; (iv) it does not rely on a pre-conditioning protocol and instead measures the "virgin" response of the tissue upon the first and subsequent indentations; (v) the proposed model has very little (if any) ambiguity in its parameter space, due to the incremental determination of the simplest constitutive law required and the proper constraint on the interaction between the bulk and shear response components measured by the full-field volumetric imaging.

The model fits to the experimental data, as well the validation study showing good predictive ability, suggest that the constitutive material law and the associated testing protocol are appropriate for characterizing the large-strain, nonlinear, visco-elastic response of the liver. The liver experiments have revealed a significant preconditioning effects of the tissue. We were able to capture these effects with a reptation-limited power law formulation of the nonlinear viscous component of the model. Based on our investigation of the potential constitutive formulations, the proposed rheological configuration is the simplest form with the fewest number of material parameters capable of capturing all of the salient features of the tissue time-dependent response. The rheological configuration of the constitutive law was determined by an incremental constitutive model selection process (see Chapter 2), considering rheological arrangements from the standard linear solid to the final 9-parameter law employed in this work.

The concurrent volumetric imaging is an essential component of the characterization, facilitating the recovery of the bulk component of the material response. In each specimen, we have considered image data from one indentation cycle at 2 mm/s displacement rate, mostly due to the difficulties associated with obtaining long volumetric sequences necessary to capture the full indentation history. Furthermore, the 2 mm/s tests contain deformations that are slow relative to the image acquisition rate, resulting in small frame-to-frame voxel displacements. Traditionally, large frame-to-frame displacement provide a significant challenge to differentail optical flow and significantly degrade its accuracy. Alternative methods relying to exhaustive searches of the local neighborhood, however, may be implemented to estimate local deformation at the faster experimental strain rates. Also, the presented results only show the vertical component of the internal organ deformation field. In the model fitting process, however, all components of the deformation field are considered and contribute equally to the objective error. In future work, it would be beneficial to consider the higher noise and lower resolution associated with the lateral imaging plane. One potential approach to addressing this issue is to estimate the noise characteristics resolution limits in all three imaging direction, as well as their dependence on the distance from the transducer. Such noise level estimates can be readily incorporated into the motion confidence parameters associated with each local image motion estimate.

In this study we were able to reduce the computational cost of the finite-element simulations by modeling the organ response under the axisymmetric formulation. The

approach is permissible for the organ geometry and boundary conditions here, but requires a mapping step between the image-based local motion estimates in cartesian 3D space and the axisymmetric coordinate system of the mechanical model.

The choice of the optimization algorithm along with appropriate initial parameter estimates and parameter constraints are essential for the success of high-dimensional optimization process. This work relied on the bounded simplex method due its fast convergence. Fast convergence is an important consideration in this application due to the computational cost associated with each evaluation of the objective function, which consists of three finite-element simulation with total runtime on the order of 8 minutes on a personal computer (dual Intel Xeon 2.8 GHz, 2 GB RAM). The drawbacks of the simplex method include its global convergence properties, especially in scenarios with multiple global minima and non-smooth objective function surface often seen in problems involving numerical approximation methods, such as the finite-element method. Based on these considerations, exploration of alternative, more robust optimization algorithms, such as simulated annealing and various forms of genetic algorithms is an interesting direction for future investigation. While one of the main drawbacks of such methods is their slow convergence, these limitations may be partially addressed with faster hardware and parallel architectures. The simulated parallel algorithm within a neighborhood (SPAN) proposed by Higginson et al. (2005) [58] is a promising optimization approach, which is designed to minimize inter-processor communication and closely retain the heuristics of the conventional serial simulated annealing algorithm. This optimization method is appealing for computational problems in biomechanics, as the authors demonstrate linear scaling of the algorithm with the number of processors in parallel architectures.

Chapter 6

Conclusion and Future Work

This work provides methods and techniques for image-based mechanical characterization of soft tissue by combining methods from computational biomechanics and nonrigid image registration.

6.1 Image-based Mechanical Characterization of Soft Tissues

Image based methods are an emerging approach to *in vivo* tissue characterization. One of their advantages is the ability to measure the *in vivo* boundary conditions, which can then be properly accounted for in the modeling process. Furthermore, image-based methods provide full-field experimental data, which offers much richer information about the material response. Devising proper methods for processing volumetric data and estimating the deformation fields is essential for future advances of these methods.

There are numerous challenges associated with these methods, such as being able to acquire, process, and analyze the massive amounts of image data obtain from fast 3D imaging, such as 3D ultrasound.

6.2 Nonrigid Image Registration for Image-Guided Surgery

The methods developed within this thesis show much potential in nonrigid image registration for image-guided procedures. In such applications, the material constitutive law and parameters must be known *a priori*. If a good tissue model and properties are available, the understanding of the tissue's mechanical response may be directly incorporated into the nonrigid-image registration process and use a finite-element biomechanical model as a mechanical regularizer (smoother) of the estimated

deformation field between the reference and deformed (intra-operative) image.

This is an area of research with potentially very high impact. One of the aspects that should be further investigated is the role of the individual parameters and their effect on the accuracy of the resulting deformation field. Recent work by Rohlfing (2003) [105] has shown that enforcing the incompressibility constraint in registration of breast imaged data significantly improves the accuracy of registration, suggesting that the tissue's bulk modulus (compressibility) parameter significantly affects the final deformation fields and is consistent with our finding in chapter 4 as well in Jordan et al. (2008) [64].

6.3 Future Directions

Robust Local Image Motion Estimation

The local image motion estimation methods employed in this work rely on the differential approach to the estimation of optical flow. This approach offers good accuracy, as shown in the performance analysis section, and is appealing to its computational efficiency. This is an especially important consideration when processing large 3D ultrasound data sets. The differential optical flow methods are derived from the first order Taylor series approximation of the continuity equation of the image domain and are therefore not well-suited for image sequences with large frame-to-frame displacements.

Alternative methods, such as exhaustive local search methods or the optical flow methods proposed by Singh (1990) [115] offer much improved accuracy under large frame-to-frame deformations. The challenge in potential application of these methods with the characterization framework lies in fast implementation to make them feasible when processing large data sets from real-time 3D ultrasound.

Robust Global Optimization

Robust optimization methods for material parameter estimation are an important area of further investigation. As discussed in chapter 6, fast simulated annealing methods, such as the simulated parallel algorithm within a neighborhood (SPAN) proposed by Higginson et al. (2005) [58] is a promising optimization approach, which promises excellent potential for parallelization.

Fast Implementations

Regardless of the specific form of the full 3D nonlinear visco-poroelastic model, the computational complexity prevents real-time applications, which are currently limited to spring-mass models [20], linear elastic models [54, 31], and simple nonlinear models

[132, 103]. Investigation of a systematic simplification of the final liver model will therefore be fundamental to its adoption by the simulation community.

The recent work Miller et al. (2007) [94] and Taylor et al. (2007) [122] has demonstrated that fast nonlinear visco-elastic biomechanical models can be implemented at real-time frame rates by combining the benefits of the total explicit Lagrangian formulation and the massively parallel architecture of modern graphics processing units (GPUs).

Evaluating the computational efficiency of the proposed finite-element liver model with the goal of real-time applications in surgical simulators and image-guided procedures is an important next step towards applications of accurate models in the clinical setting. A systematic approach to reducing the computational cost associated with the current model may be devised, considering the following areas of potential improvements:

1. Simplified constitutive equations using the fast constitutive model prototyping methods developed in chapter 2, it is possible to evaluate the relative contributions of individual constitutive element in specific loading rates and deformation modes. This approach suggests that a heuristic approach for potential simplifications of the constitutive form may be devised. Specifically, one can evaluate accuracy vs. speed tradeoff of the full nonlinear visco-elastic model in comparison to simpler constitutive configurations.
2. Simplified meshes the mesh density significantly affects the computational time associated with the model preprocessing and solution. By pursuing a rigorous mesh convergence study, analogously to the simple convergence study presented in section 5.2.3, the dependence between numerical accuracy and mesh density may be exploited for faster model run times. If the mesh accuracy limits are well characterized for various loading histories, rates, and boundary interactions, meshing guidelines may be developed to provide user-specified levels of numerical accuracy while minimizing computational run time.
3. Preprocessing simplification of the constitutive form and pre-computation of the model stiffness matrix using approximation techniques described by Gibson and Mirtich (1997) [54] and Cotin et al. (1999) [31] may be investigated to characterized the accuracy loss associated with such techniques.
4. Fast collision detection - fast collision detection algorithms are essential for efficient surgical simulation and model interaction. It is an active area of research with many potential avenues for improving the computation efficiency of tool-tissue interactions, as well as tissue-tissue interaction, which are known to be notoriously challenging. One of the potential avenues for improving the boundary checking / collision detection is the use of novel analytical shape description methods (in contrast to mesh-based methods), which would allows for fast and potentially direct computation of model collisions.

Other Applications

There are numerous opportunities and future directions for performing image-based tissue characterization on other tissue types and organ systems. Furthermore, the non-invasive nature of the image-based approach suggest that there are numerous opportunities for image-based diagnostic applications. In addition, future efforts should investigate the feasibility of applications on other scales (i.e. confocal microscopy and atomic force microscopy). The methods developed in this thesis are independent of imaging modality as well as the length scale at which these methods are applied. Confocal microscopy of cellular biomechanics is an emerging area of research. In conjunction with atomic force microscopy, an experimental protocol very similar to that described in this thesis may be devised and used to offer insight into the cellular mechanical response and provide new mean for elucidating the structural components and function of the cytoskeleton.

6.4 Final Words

This thesis work presented a general tissue characterization framework, which relies on conventional indentation testing coupled with concurrent volumetric imaging. The framework was applied to constitutive characterization of perfused porcine liver, resulting in a visco-elastic nonlinear constitutive law and its finite-element implementation capable of predicting mechanical response of the liver in situations representative of surgical manipulation. Furthermore, the second chapter demonstrated through incremental model improvements that the proposed eight parameter model offers good trade-off between model simplicity (number of material parameters) and accuracy under a wide range of applied strain rates. Because of the fast temporal resolution of the volumetric imaging system, this tissue testing approach may be attractive to visco-elastic image-based characterization of many other tissues and has great potential for *in vivo* applications.

Bibliography

- [1] ABAQUS. *ABAQUS Theory Manual*. SIMULIA, Providence, RI, version 6.7 edition, 2007.
- [2] N. Abolhassani, R. Patel, and M. Moallem. Needle insertion into soft tissue: a survey. *Medical Engineering and Physics*, 29(4):413–431, May 2007.
- [3] S. K. Alam, E. J. Feleppa, A. Kalisz, and S. Ramchandran. Prostate elastography: preliminary in vivo results. In *Proceedings of SPIE*, volume 5750, 2005.
- [4] R. Alterovitz, K. Goldberg, and A. Okamura. Planning for steerable bevel-tip needle insertion through 2D soft tissue with obstacles. In *Robotics and Automation, 2005. ICRA 2005. Proceedings of the 2005 IEEE International Conference on*, pages 1640–1645, 18–22 April 2005.
- [5] R. Alterovitz, K. Goldberg, J. Pouliot, I-C. J. Hsu, Y. Kim, S. M. Noworolski, and J. Kurhanewicz. Registration of mr prostate images with biomechanical modeling and nonlinear parameter estimation. *Medical Physics*, 33(2):446–454, Feb 2006.
- [6] N Archip, O. Clatz, S. Whalen, D Kacher, A. Fedorov, A. Kot, N. Chrisochoides, F. Jolesz, A. Golby, P. M Black, and S. K. Warfield. Non-rigid alignment of pre-operative mri, fmri, and dt-mri with intra-operative mri for enhanced visualization and navigation in image-guided neurosurgery. *Neuroimage*, 35(2):609–624, Apr 2007.
- [7] E. M. Arruda and M. C. Boyce. A three-dimensional constitutive model for the large stretch behavior of rubber elastic materials. *Journal of Mechanics and Physics of Solids*, 41:389–412, 1993.
- [8] M. Audette. *Anatomical surface identification, range-sensing and registration for characterizing intrasurgical brain deformations*. PhD thesis, McGill University, 2003.
- [9] R. Bajcsy and S. Kovacic. Multi-resolution elastic matching. *Computer Vision, Graphics, and Image Processing*, 46:1–21, 1989.

-
- [10] S. Baker and I. Matthews. Lucas-Kanade 20 Years On: A Unifying Framework. *International Journal of Computer Vision*, 56(3):221–255, March 2004.
- [11] A. Balakrishnan and S. Socrate. Material Property Differentiation in Indentation Testing Using Secondary Sensors. *Experimental Mechanics*, (in press), 2007.
- [12] R. A. Baldewsing, C. L. de Korte, J. A. Schaar, F. Mastik, and A. F. W. van der Steen. A finite element model for performing intravascular ultrasound elastography of human atherosclerotic coronary arteries. *Ultrasound in Medicine and Biology*, 30(6):803–813, Jun 2004.
- [13] J. L. Barron, D. J. Fleet, and S. S. Beauchemin. Performance of optical flow techniques. *International Journal of Computer Vision*, 12(1):43–77, 1994.
- [14] J. S. Bergstrom and M. C. Boyce. Constitutive modeling of the time-dependent and cyclic loading of elastomers and application to soft biological tissues. *Mechanics of Materials*, 33:523–530, 2001.
- [15] D. Bielser and M. H. Gross. Open surgery simulation. *Studies in Health Technology and Informatics*, 85:57–63, 2002.
- [16] J. E. Bischoff, E. M. Arruda, and K. Grosh. Finite element modeling of human skin using an isotropic, nonlinear elastic constitutive model. *Journal of Biomechanics*, 33(6):645–652, Jun 2000.
- [17] J. E. Bischoff, E. M. Arruda, and K. Grosh. A rheological network model for the continuum anisotropic and viscoelastic behavior of soft tissue. *Biomechanics and Modeling in Mechanobiology*, 3(1):56–65, Sep 2004.
- [18] A. Bistoquet, J. Oshinski, and O. Skrinjar. Left Ventricular Deformation Recovery From Cine MRI Using an Incompressible Models. *IEEE Transactions on Medical Imaging*, 26(9):1136–1153, Sep 2007.
- [19] R. Bowden, T. A. Mitchell, and M. Sarhadi. Real-time dynamic deformable meshes for volumetric segmentation and visualization. In A. F. Clark, editor, *British Machine Vision Conference*, volume 1, pages 310–319, 1997.
- [20] M. Bro-Nielsen, D. Helfrick B. Glass, X. Zeng, and H. Connacher. VR simulation of abdominal trauma surgery. In J. D. Westwood, H. M. Hoffman, D. Stredney, and S. J. Weghorst, editors, *Medicine meets virtual reality: Art, science, and technology*, pages 117–123, 1998.
- [21] M. Bro-Nielsen and C. Gramkow. Fast fluid registration of medical images. In *Proceedings of Visualization in Biomedical Computing*, volume 1131 of *Springer Lecture Notes in Computer Science*, pages 267–276, 1996.

- [22] I. Brouwer, J. Ustin, L. Bentley, A. Sherman, N. Dhruv, and F. Tendick. Measuring in vivo animal soft tissue properties for haptic modeling in surgical simulation. *Studies in Health Technology and Informatics*, 81:69–74, 2001.
- [23] J. D. Brown, J. Rosen, Y. S. Kim, L. Chang, M. N. Sinanan, and B. Hannaford. In-vivo and in-situ compressive properties of porcine abdominal soft tissues. *Studies in Health Technology and Informatics*, 94:26–32, 2003.
- [24] F. J. Carter, T. G. Frank, P. J. Davies, D. McLean, and A. Cuschieri. Measurements and modelling of the compliance of human and porcine organs. *Medical Image Analysis*, 5(4):231–236, Dec 2001.
- [25] T. J. Carter, M. Sermesant, D. M. Cash, D. C. Barratt, C. Tanner, and D. J. Hawkes. Application of soft tissue modelling to image-guided surgery. *Medical Engineering and Physics*, 27(10):893–909, Dec 2005.
- [26] David M Cash, Michael I Miga, Sean C Glasgow, Benoit M Dawant, Logan W Clements, Zhujiang Cao, Robert L Galloway, and William C Chapman. Concepts and preliminary data toward the realization of image-guided liver surgery. *Journal of Gastrointestinal Surgery*, 11(7):844–859, 2007.
- [27] E. J. Chen, J. Novakofski, W. K. Jenkins, and W. D. O’Brien. Young’s modulus measurements of soft tissues with application to elasticity imaging. *IEEE Transactions on Ultrasonics, Ferroelectrics, and Frequency Control*, 43(1):191–194, 1996.
- [28] G. Christensen, S. Joshi, and M. Miller. Volumetric transformation of brain anatomy. *IEEE Transactions on Medical Imaging*, 16(6):864–877, 1997.
- [29] O. Clatz, H. Delingette, I.-F. Talos, A.J. Golby, R. Kikinis, F.A. Jolesz, N. Ayache, and S.K. Warfield. Robust nonrigid registration to capture brain shift from intraoperative MRI. *IEEE Transactions on Medical Imaging*, 24(11):1417–1427, 2005.
- [30] T. Corpetti, E. Memin, A. Santa-Cruz, D. Heitz, and G. Arroyo. Optical flow estimation in experimental fluid mechanics. In *Proceedings of ISSPA*, 2003.
- [31] S. Cotin, H. Delingette, and N. Ayache. Real-time elastic deformations of soft tissues for surgery simulation. *IEEE Transactions on Visualization and Computer Graphics*, 5(1):62–73, 1999.
- [32] C. Davatzikos. Spatial transformation and registration of brain images using elastically deformable models. *Computer Vision, Graphics, and Image Processing*, 66(2):207–222, 1997.

- [33] P. Davies. Mathematical modeling for keyhole surgery simulation: a biomechanical model for spleen tissue. *IMA Journal of Applied Mathematics*, 67:41–67, 2002.
- [34] S. L. Dawson. A critical approach to medical simulation. *Bulletin of the American College of Surgeons*, 87:12–18, 2002.
- [35] C. L. de Korte, J. A. Schaar, F. Mastik, P. W. Serruys, and A. F. van der Steen. Intravascular elastography: from bench to bedside. *J Interv Cardiol*, 16(3):253–259, Jun 2003.
- [36] S. P. DiMaio, G. S. Fischer, S. J. Haker, N. Hata, I. Iordachita, C. M. Tempany, R. Kikinis, and G. Fichtinger. A system for MRI-guided prostate interventions. In *The First IEEE/RAS-EMBS International Conference on Biomedical Robotics and Biomechatronics, 2006. BioRob 2006.*, pages 68–73, February 20–22, 2006.
- [37] S. P. DiMaio and S. E. Salcudean. Needle steering and motion planning in soft tissues. *Biomedical Engineering, IEEE Transactions on*, 52(6):965–974, June 2005.
- [38] S.P. DiMaio and S.E. Salcudean. Needle insertion modeling and simulation. *Robotics and Automation, IEEE Transactions on*, 19(5):864–875, Oct. 2003.
- [39] S. Dokos, I. J. LeGrice, B. H. Smaill, J. Kar, and A. A. Young. A triaxial-measurement shear-test device for soft biological tissues. *J Biomech Eng*, 122(5):471–478, Oct 2000.
- [40] A. du Bois d’Aische, M. De Craene, S. Haker, N. Weisenfeld, C. Tempany, B. Macq, and S. K. Warfield. Improved Non-rigid Registration of Prostate MRI. In *International Conference on Medical Image Computing and Computer-Assisted Intervention*, Springer Lecture Notes in Computer Science, pages 845–852, September 2004.
- [41] D. R. Einstein, A. D. Freed, N. Stander, B. Fata, and I. Vesely. Inverse parameter fitting of biological tissues: a response surface approach. *Annals of Biomedical Engineering*, 33(12):1819–1830, 2005.
- [42] S. L. Evans, C. A. Holt, H. Ozturk, K. Saidi, and N. G. Shrive. Measuring soft tissue properties using digital image correlation and finite element modelling. In *Experimental Analysis of Nano and Engineering Materials and Structures*, pages 313–314. Springer Netherlands, 2007.
- [43] S. Febvay, S. Socrate, and M.D. House. Biomechanical modeling of cervical tissue: A quantitative investigation of cervical funneling. In *ASME International*

- Mechanical Engineering Congress and Exposition (IMECE)*, Washington, DC, 2003.
- [44] M. Ferrant, A. Nabavi, B. Macq, F. A. Jolesz, R. Kikinis, and S. K. Warfield. Registration of 3-D intraoperative MR images of the brain using a finite-element biomechanical model. *IEEE Transactions on Medical Imaging*, 20(12):1384–1397, 2001.
- [45] J. Ferry. *Viscoelastic Properties of Polymers*. John Wiley & Sons, Inc., 1970.
- [46] G. Fichtinger, T. L. DeWeese, A. Patriciu, A. Tanacs, A. Mazilu, J. H. Anderson, K. Masamune R. H. Taylor, and D. Stoianovici. Robotically assisted prostate biopsy and therapy with intra-operative ct guidance. *Journal of Academic Radiology*, 9(1):60–74, 2001.
- [47] P. Foroughi, P. Abolmaesumi, and K. Hashtrudi-Zaad. Intra-Subject Elastic Registration of 3D Ultrasound Images. *Medical Image Analysis*, 10(5):713–725, 2006.
- [48] Y. C. Fung. *Biomechanics: Mechanical Properties of Living Tissues*. Springer-Verlag, New York, second edition, 1993.
- [49] A. G. Gallagher and C. U. Cates. Approval of virtual reality training for carotid stenting: What this means for procedural-based medicine. *Journal of the American Medical Association*, 292:3024–3026, 2004.
- [50] B. S. Garra. Imaging and estimation of tissue elasticity by ultrasound. *Ultrasound Quarterly*, 23(4):255–268, Dec 2007.
- [51] B. S. Garra, E. I. Cespedes, J. Ophir, S. R. Spratt, R. A. Zuurbier, C. M. Magnant, and M. F. Pennanen. Elastography of breast lesions: initial clinical results. *Radiology*, 202(1):79–86, Jan 1997.
- [52] T. C. Gasser, R. W. Ogden, and G. A. Holzapfel. Hyperelastic modelling of arterial layers with distributed collagen fibre orientations. *Journal of the Royal Society Interface*, 3(6):15–35, Feb 2006.
- [53] A. Gefen and S. S. Margulies. Are in vivo and in situ brain tissues mechanically similar? *Journal of Biomechanics*, 37(9):1339–1352, Sep 2004.
- [54] S. Gibson and B. Mirtich. A survey of deformable modeling in computer graphics. Technical Report TR-97-19, Mitsubishi Electric Research Lab, Cambridge, MA, 1997.

- [55] A. Hagemann, K. Rohr, H.S. Stiehl, U. Spetzger, and J.M. Gilsbach. Biomechanical modeling of the human head for physically based, nonrigid image registration. *IEEE Transactions on Medical Imaging*, 18(10):875–884, 1999.
- [56] N. Hata, R. Dohi, S. Warfield, W. Wells, R. Kikinis, and J. F.A. Multimodality deformable registration of pre- and intraoperative images for mri-guided brain surgery. In *International Conference on Medical Image Computing and Computer-Assisted Intervention*, volume 1496 of *Lecture Notes in Computer Science*, pages 1067–1074, 1998.
- [57] Hibbit, Karlsson, and & Sorensen. *ABAQUS/Standard 6.7 user's manual*. Hibbit, Karlsson, & Sorensen, Pawtucket, RI, 2007.
- [58] J. S. Higginson, R. R. Neptune, and F. C. Anderson. Simulated parallel annealing within a neighborhood for optimization of biomechanical systems. *Journal of Biomechanics*, 38(9):1938–1942, Sep 2005.
- [59] K. M. Hiltawsky, M. Krger, C. Starke, L. Heuser, H. Ermert, and A. Jensen. Freehand ultrasound elastography of breast lesions: clinical results. *Ultrasound in Medicine & Biology*, 27(11):1461–1469, Nov 2001.
- [60] G. A. Holzapfel. *Nonlinear Solid Mechanics: A Continuum Approach for Engineering*. Wiley, 1st edition, 2000.
- [61] B. K. P. Horn and B. G. Schunck. Determining Optical Flow. *Artificial Intelligence*, 16(1-3):186–203, 1981.
- [62] T. Hu and J. P. Desai. Characterization of soft-tissue material properties: Large deformation analysis. In *International Symposium on Medical Simulation*, page 294, Cambridge, MA, 2004.
- [63] P. Jordan. 3D implementation of the Laplacian-smooth Horn & Schunck optical flow. Technical report, Harvard University, 2006.
- [64] P. Jordan, S. Socrate, T. Zickler, and R.D. Howe. A nonrigid image registration framework for identification of tissue mechanical parameters. In *International Conference on Medical Image Computing and Computer Aided Intervention*, 2008.
- [65] P. Jordan, T.E. Zickler, S. Socrate, and R.D. Howe. Modular nonrigid image registration framework using nonlinear mechanical regularization (submitted). *Medical Image Analysis*, 2008.
- [66] D. Kalanovic, M. P. Ottensmeyer, J. Gross, G. Buess, and S. L Dawson. Independent testing of soft tissue visco-elasticity using indentation and rotary shear deformations. *Medicine Meets Virtual Reality*, 2003.

- [67] F. Kallel, R. E. Price, E. Konofagou, and J. Ophir. Elastographic imaging of the normal canine prostate in vitro. *Ultrasonic Imaging*, 21(3):201–215, Jul 1999.
- [68] M. Kauer, V. Vuskovic, J. Dual, G. Szekely, and M. Bajka. Inverse finite element characterization of soft tissues. *Medical Image Analysis*, 6(3):275–287, Sep 2002.
- [69] A. E. Kerdok. *Characterizing the Nonlinear Mechanical Response of Liver to Surgical Manipulation*. PhD thesis, Harvard University, 2006.
- [70] A. E. Kerdok, P. Jordan, Y. Liu, P. Wellman, S. Socrate, and R. D. Howe. Identification of nonlinear constitutive law parameters of breast tissue. In *ASME Summer Bioengineering Conference, Vail, CO*, 2005.
- [71] A. E. Kerdok, M. P. Ottensmeyer, and R. D. Howe. Effects of perfusion on the viscoelastic characteristics of liver. *Journal of Biomechanics*, 39(12):2221–2231, 2006.
- [72] J. Kim, B. Tay, N. Stylopoulos, D.W. Rattner, and M.A. Srinivasan. Characterization of intra-abdominal tissues from in vivo animal experiment for surgical simulation. In *Medical Image Computing and Computer Assisted Intervention*, 2003.
- [73] T. A. Krouskop, T. M. Wheeler, F. Kallel, B. S. Garra, and T. Hall. Elastic moduli of breast and prostate tissues under compression. *Ultrasonic Imaging*, 20(4):260–274, Oct 1998.
- [74] U. Kuhnappel, H. K. Cakmak, and H. Maass. Endoscopic surgery training using virtual reality and deformable tissue simulation. *Computers & Graphics*, 24(1):671–682, 2000.
- [75] S. K. Kyriacou, C. Davatzikos, S. J. Zinreich, and R. N. Bryan. Nonlinear elastic registration of brain images with tumor pathology using a biomechanical model. *IEEE Transactions on Medical Imaging*, 18(7):580–592, 1999.
- [76] J. C. Lagarias, J. A. Reeds, M. H. Wright, and P. E. Wright. Convergence Properties of the Nelder-Mead Simplex Method in Low Dimensions. *SIAM Journal of Optimization*, 9(1):112–147, 1998.
- [77] D. Laharie, F. Zerbib, X. Adhoute, X. Bou-Lahorgue, J. Foucher, L. Castra, A. Rullier, J. Bertet, P. Couzigou, M. Amouretti, and V. de Ldinghen. Diagnosis of liver fibrosis by transient elastography (fibroscan) and non-invasive methods in crohn’s disease patients treated with methotrexate. *Alimentary Pharmacology & Therapeutics*, 23(11):1621–1628, Jun 2006.

- [78] M. J. Ledesma-Carbayo, J. Kybic, M. Desco, A. Santos, M. Shling, P. Hunziker, and M. Unser. Spatio-temporal nonrigid registration for ultrasound cardiac motion estimation. *IEEE Transactions on Medical Imaging*, 24(9):1113–1126, 2005.
- [79] S. Lim and A. El Gamal. Optical Flow Estimation Using High Frame Rate Sequences. In *Proceedings of the International Conference on Image Processing*, volume 2, pages 925–928, 2001.
- [80] M.G. Linguraru, N. Vasilyev, P.J. Del Nido, and R.D. Howe. Atrial septal defect tracking in 3D cardiac ultrasound. In *Lecture Notes in Computer Science*, volume 4190, pages 596–603. Medical Image Computing and Computer-Assisted Intervention (MICCAI), Springer New York, 2006.
- [81] A. Liu, C. Kaufmann, and D. Tanaka. An architecture for simulating needle-based surgical procedures. In *International Conference on Medical Image Computing and Computer-Assisted Intervention*, pages 1137–1144, 2001.
- [82] Z. Liu and L. E. Bilston. Large deformation shear properties of liver tissue. *Biorheology*, 39(6):735–742, 2002.
- [83] D. Loeckx, J. Ector, F. Maes, J. D’hooge, D. Vandermeulen, J-U Voigt, H. Heidebuchel, and P. Suetens. Spatiotemporal non-rigid image registration for 3d ultrasound cardiac motion estimation. In *Proceedings of SPIE Medical Imaging*, volume 6513, 2007.
- [84] B. D. Lucas and T. Kanade. An Iterative Image Registration Technique with an Application to Stereo Vision. In *Proceedings of the 7th International Joint Conference on Artificial Intelligence (IJCAI '81)*, pages 674–679, 1981.
- [85] E. Mazza, A. Nava, D. Hahnloser, W. Jochum, and M. Bajka. The mechanical response of human liver and its relation to histology: an in vivo study. *Medical Image Analysis*, 11(6):663–672, Dec 2007.
- [86] M. Meadows. Computer-assisted surgery: An update. *FDA Consumer Magazine*, July-August, 2005.
- [87] M. I. Miga, T. K. Sinha, D. M. Cash, R. L. Galloway, and R. J. Weil. Cortical surface registration for image-guided neurosurgery using laser-range scanning. *IEEE Transactions on Medical Imaging*, 22(8):973–985, 2003.
- [88] K. Miller. Constitutive modelling of abdominal organs. *Journal of Biomechanics*, 33(3):367–373, Mar 2000.
- [89] K. Miller. How to test very soft biological tissues in extension? *Journal of Biomechanics*, 34(5):651–657, May 2001.

-
- [90] K. Miller. Method of testing very soft biological tissues in compression. *Journal of Biomechanics*, 38(1):153–158, 2005.
- [91] K. Miller and K. Chinzei. Constitutive modelling of brain tissue: experiment and theory. *Journal of Biomechanics*, 30(11-12):1115–1121, 1997.
- [92] K. Miller and K. Chinzei. Mathematical modelling of brain tissue mechanical properties for computer and robot assisted surgery. *Journal of Mathematical Modelling and Scientific Computing*, 13(1/2):1–11, 2001.
- [93] K. Miller, K. Chinzei, G. Orsengo, and P. Bednarz. Mechanical properties of brain tissue in-vivo: experiment and computer simulation. *Journal of Biomechanics*, 33(11):1369–1376, 2000.
- [94] K. Miller, G. Joldes, D. Lance, and A. Wittek. Total Lagrangian explicit dynamics finite element algorithm for computing soft tissue deformation. *Communications in Numerical Methods in Engineering*, 23(2):121–134, 2007.
- [95] K. M. Myers, A. P. Paskaleva, M. House, and S. Socrate. Mechanical and biochemical properties of human cervical tissue. *Acta Biomaterialia*, 4(1):104–116, Jan 2008.
- [96] A. Nava, E. Mazza, M. Furrer, P. Villiger, and W. H. Reinhart. In vivo mechanical characterization of human liver. *Medical Image Analysis*, 12(2):203–216, Apr 2008.
- [97] A. Nava, E. Mazza, F. Kleinermann, N. J. Avis, J. McClure, and M. Bajka. Evaluation of the mechanical properties of human liver and kidney through aspiration experiments. *Technology and Health Care*, 12(3):269–280, 2004.
- [98] A. M. Okamura, C. Simone, and M. D. O’Leary. Force modeling for needle insertion into soft tissue. *IEEE Transactions on Biomedical Engineering*, 51(10):1707–1716, Oct 2004.
- [99] J. Ophir, F. Kallel, T. Varghese, E. Konofagou, K. Alam, T. Krouskop, B. Garra, and R. Righetti. Elastography. *Comptes Rendus de l’Academie des Sciences*, IV:1–20, 2001.
- [100] M. P. Ottensmeyer. In vivo measurement of solid organ visco-elastic properties. *Studies in Health Technology and Informatics*, 85:328–333, 2002.
- [101] X. Papademetris, A. J. Sinusas, D. P. Dione, R. T. Constable, and J. S. Duncan. Estimation of 3-D Left Ventricular Deformation from Medical Images using Biomechanical Models. *IEEE Transactions on Medical Imaging*, 21(7):786–800, 2002.

- [102] N. Papenberg, A. Bruhn, T. Brox, S. Didas, and J. Weickert. Highly accurate optic flow computation with theoretically justified warping. *International Journal of Computer Vision*, 67(2):141–158, 2006.
- [103] G. Picinbono, H. Delingette, and N. Ayache. Non-linear and anisotropic elastic soft tissue models for medical simulation. In *Proceedings of The International Conference on Robotics and Automation*, volume 2, pages 1370–1375, 2001.
- [104] J. Rexilius, S. K. Warfield, C. R. G. Guttman, X. Wei, R. Benson, L. Wolfson, M. Shenton, M. Handels, and R. Kikinis. A novel nonrigid registration algorithm and applications. In *Proceedings of the 4th International Conference on Medical Image Computing and Computer-Assisted Intervention (MICCAI)*, pages 923–931, 2001.
- [105] T. Rohlfing, Jr. Maurer, C.R., D.A. Bluemke, and M.A. Jacobs. Volume-preserving nonrigid registration of MR breast images using free-form deformation with an incompressibility constraint. *IEEE Transactions on Medical Imaging*, 22(6):730–741, 2003.
- [106] L. Roose, W. Mollemans, D. Loeckx, F. Maes, and P. Suetens. Biomechanically based elastic breast registration using mass tensor simulation. *Proceedings of the 4th International Conference on Medical Image Computing and Computer-Assisted Intervention (MICCAI)*, 9:718–725, 2006.
- [107] J. Rosen, J. D. Brown, L. Chang, M. Barreca, M. Sinanan, and B. Hannaford. The bluedragon - a system for measuring the kinematics and dynamics of minimally invasive surgical tools in-vivo. In *IEEE International Conference on Robotics and Animation*, 2002.
- [108] J. Rosen, J. D. Brown, S. De, M. Sinanan, and B. Hannaford. Biomechanical properties of abdominal organs in vivo and postmortem under compression loads. *Journal of Biomechanical Engineering*, 130(2):021020, Apr 2008.
- [109] M. B. Rubin and S. R. Bodner. A three-dimensional nonlinear model for dissipative response of soft tissue. *International Journal of Solids and Structures*, 39:5081–5099, 2002.
- [110] N. V. Ruiters, T. O. Muller, R. Stotzka, H. Gemmeke, J. R. Reichenbach, and W. A. Kaiser. Automatic image matching for breast cancer diagnostics by a 3D deformation model of the mamma. *Biomedical Technology*, 47 Suppl 1 Pt 2:644–647, 2002.
- [111] A. Samani, J. Bishop, and D. B. Plewes. 3D finite element model for breast MRI non-rigid registration. In *Proceedings of International Society for Magnetic Resonance in Medicine*, page 837, 2001.

- [112] E. Samur, M. Sedef, C. Basdogan, L. Avtan, and O. Duzgun. A robotic indenter for minimally invasive measurement and characterization of soft tissue response. *Medical Image Analysis*, 11(4):361–373, Aug 2007.
- [113] M. Sermesant, C. Forest, X. Pennec, H. Delingette, and N. Ayache. Deformable biomechanical models: application to 4D cardiac image analysis. *Medical Image Analysis*, 7(4):475–488, 2003.
- [114] L. F. Shampine. *Numerical Solution of Ordinary Differential Equations*. Chapman & Hall, New York, 1994.
- [115] A. Singh. *Image-flow computation: Estimation-theoretic framework, unification and integration*. PhD thesis, Columbia University, 1990.
- [116] O. Skrinjar, A. Nabavi, and J. Duncan. Model-driven brain shift compensation. *Medical Image Analysis*, 6(4):361–373, Dec 2002.
- [117] W. S. Slaughter. *The Linearized Theory of Elasticity*. Birkhauser, 2002.
- [118] S. Socrate and M. C. Boyce. A Constitutive Model for the Large Strain Behavior of Cartilage. In *Proceedings of 2001 Bioengineering Conference*, volume 50, pages 597–598. ASME, 2001.
- [119] J.-K. Suh and R. L. Spilker. Indentation analysis of biphasic articular cartilage: Nonlinear phenomena under finite deformation. *Journal of Biomechanical Engineering*, 116:1–9, 1994.
- [120] H. Sun, D. Roberts, A. Hartov, K. Rick, and K. Paulsen. Using cortical vessels for patient registration during image-guided neurosurgery: a phantom study. In *Proceedings of SPIE*, volume 5029, pages 183–191, May 2003.
- [121] G. Szekely, G. Brechbuhler, J. Dual, R. Enzler, J. Hug, R. Hutter, N. Ironmonger, M. Kauer, V. Meier, P. Niederer, A. Rhomberg, P. Schmid, G. Schweitzer, M. Thaler, V. Vuskovic, G. Troster, U. Haller, and M. Bajka. Virtual reality-based simulation of endoscopic surgery. *Presence: Teleoperators and Virtual Environments*, 9(3):310–333, 2000.
- [122] Zeike A Taylor, Mario Cheng, and Sbastien Ourselin. Real-time nonlinear finite element analysis for surgical simulation using graphics processing units. In *International Conference on Medical Image Computing and Computer Assisted Intervention*, volume 10, pages 701–708, 2007.
- [123] F. Tendick, M. Downes, T. Goktekin, M. C. Cavusoglu, D. Feygin, X. Wu, R. Eval, M. Hegarty, and L. W. Way. A virtual environment testbed for training laparoscopic surgical skills. *Presence: Teleoperators and Virtual Environments*, 9(3):236–255, 2000.

- [124] M. Ursino, J. L. Tasto, B. H. Nguyen, R. Cunningham, and G. L. Merrill. Cathsim: an intravascular catheterization simulator on a pc. *Studies in Health Technology and Informatics*, 62:360–366, 1999.
- [125] D. Valtorta and E. Mazza. Dynamic measurement of soft tissue viscoelastic properties with a torsional resonator device. *Medical Image Analysis*, 9(5):481–490, Oct 2005.
- [126] I. M. Ward. *Mechanical Properties of Solid Polymers*. John Wiley & Sons, Inc., 1983.
- [127] S.K. Warfield, M. Ferrant, X. Gallez, A. Nabavi, F.A. Jolesz, and R. Kikinis. Real-time biomechanical simulation of volumetric brain deformation for image guided neurosurgery. In *SC 2000: High Performance Networking and Computing Conference*, page 23, 04-10 Nov. 2000.
- [128] J. Weickert and C. Schnörr. A theoretical framework for convex regularizers in pde-based computation of image motion. *International Journal of Computer Vision*, 45(3):245–264, 2001.
- [129] P. Wellman. *Tactile Imaging*. PhD thesis, Harvard University, 1999.
- [130] A. Wittek, T. Dutta-Roy, Z. Taylor, A. Horton, T. Washio, K. Chinzei, and K. Miller. Subject-specific non-linear biomechanical model of needle insertion into brain. *Comput Methods Biomech Biomed Engin*, 11(2):135–146, Apr 2008.
- [131] A. Wittek, K. Miller, R. Kikinis, and S. K Warfield. Patient-specific model of brain deformation: application to medical image registration. *Journal of Biomechanics*, 40(4):919–929, 2007.
- [132] X. Wu, M. S. Downes, T. Goktekin, and F. Tendick. Adaptive nonlinear finite elements for deformable body simulation using dynamic progressive meshes. In *Eurographics*, volume 20, pages 349–359, 2001.
- [133] W.-C. Yeh, P.-C. Li, Y.-M. Jeng, H.-C. Hsu, P.-L. Kuo, M.-L. Li, P.-M. Yang, and P.-H. Lee. Elastic modulus measurements of human liver and correlation with pathology. *Ultrasound in Medicine & Biology*, 28(4):467–474, 2002.
- [134] F. Yeung, S. F. Levinson, D. Fu, and K. J. Parker. Feature-adaptive motion tracking of ultrasound image sequences using a deformable mesh. *IEEE Transactions on Medical Imaging*, 17(6):945–956, 1998.
- [135] C. J. Zhu and C.C.-B. Wang. *Biphasic Theory for Hydrated Soft Tissues*. New York Orthopaedic Hospital Research Laboratory, 1998.
- [136] O. C. Zienkiewicz. *The Finite Element Method*. McGraw-Hill, 3 edition, 1977.

Appendix A

Deriving Laplacian-Smooth Horn & Schunck Optical Flow

First-Order Motion Field Smoothness

Traditionally, the Horn & Schunck algorithm [61] is implemented with a first-order motion smoothness constraint. The corresponding functional to be minimized is

$$\Phi(u, v, w) = \int_{\Omega} \left(\left(\frac{\partial I}{\partial x} u + \frac{\partial I}{\partial y} v + \frac{\partial I}{\partial z} w + \frac{\partial I}{\partial t} \right)^2 + \alpha E_s \right) dx dy dz, \quad (\text{A.1})$$

where E_s is the regularization term defined as

$$\begin{aligned} E_s = & \left(\frac{\partial u}{\partial x} \right)^2 + \left(\frac{\partial u}{\partial y} \right)^2 + \left(\frac{\partial u}{\partial z} \right)^2 \\ & + \left(\frac{\partial v}{\partial x} \right)^2 + \left(\frac{\partial v}{\partial y} \right)^2 + \left(\frac{\partial v}{\partial z} \right)^2 \\ & + \left(\frac{\partial w}{\partial x} \right)^2 + \left(\frac{\partial w}{\partial y} \right)^2 + \left(\frac{\partial w}{\partial z} \right)^2. \end{aligned} \quad (\text{A.2})$$

First-order smoothness term results in a homogenous smoothing of the resulting motion field and therefore blurs discontinuities, sinks, and sources in the motion field. Other regularizers have been proposed in literature, including the Laplacian [61], div-curl [30], and anisotropic flow-driven [128] operators.. Since the original paper by Horn and Schunck does not derive the variational solution for the Laplace-smooth regularization, it is derived in this document following the derivation of the first-order smoothness solution.

The minimization of the functional $\Phi(u, v, w)$ in Eq. A.1 can be achieved through calculus of variations. The Euler-Lagrange equations are the essential tool in variational problems and are analogous to zero-slope estimation (setting partial derivatives to zero) in calculus. The Euler-Lagrange equations for the functional in Eq. A.1 are

$$\nabla^2 u = \frac{1}{\alpha} \left(\frac{\partial I}{\partial x} u + \frac{\partial I}{\partial y} v + \frac{\partial I}{\partial z} w + \frac{\partial I}{\partial t} \right) \frac{\partial I}{\partial x} \quad (\text{A.3})$$

$$\nabla^2 v = \frac{1}{\alpha} \left(\frac{\partial I}{\partial x} u + \frac{\partial I}{\partial y} v + \frac{\partial I}{\partial z} w + \frac{\partial I}{\partial t} \right) \frac{\partial I}{\partial y} \quad (\text{A.4})$$

$$\nabla^2 w = \frac{1}{\alpha} \left(\frac{\partial I}{\partial x} u + \frac{\partial I}{\partial y} v + \frac{\partial I}{\partial z} w + \frac{\partial I}{\partial t} \right) \frac{\partial I}{\partial z}. \quad (\text{A.5})$$

To solve this variational problem in a finite-difference scheme, the Laplacian terms can be approximated numerically as

$$\nabla^2 \psi \approx \bar{\psi}_{ijk} - \psi_{ijk}, \quad (\text{A.6})$$

where $\bar{\psi}_{ijk}$ is a Gaussian-weighted spatial average around point (i, j, k) . The Eqns. A.4 can then be rewritten as

$$\bar{u}_{ijk} - u_{ijk} = \frac{1}{\alpha} \left(\frac{\partial I}{\partial x} u_{ijk} + \frac{\partial I}{\partial y} v_{ijk} + \frac{\partial I}{\partial z} w_{ijk} + \frac{\partial I}{\partial t} \right) \frac{\partial I}{\partial x} \quad (\text{A.7})$$

$$\bar{v}_{ijk} - v_{ijk} = \frac{1}{\alpha} \left(\frac{\partial I}{\partial x} u_{ijk} + \frac{\partial I}{\partial y} v_{ijk} + \frac{\partial I}{\partial z} w_{ijk} + \frac{\partial I}{\partial t} \right) \frac{\partial I}{\partial y} \quad (\text{A.8})$$

$$\bar{w}_{ijk} - w_{ijk} = \frac{1}{\alpha} \left(\frac{\partial I}{\partial x} u_{ijk} + \frac{\partial I}{\partial y} v_{ijk} + \frac{\partial I}{\partial z} w_{ijk} + \frac{\partial I}{\partial t} \right) \frac{\partial I}{\partial z}. \quad (\text{A.9})$$

The iterative solution to this system of equation is solved by the Gauss-Seidel iterative approach. Iterative techniques are preferable for large systems, such as this one. Gauss-Seidel is preferred over the Jacobi method because it requires no vector copying and additional storage. The Gauss-Seidel iterative technique for a system of equations $A\phi = b$ can be written as

$$\phi_i^{k+1} = \frac{1}{a_{ii}} \left(b_i - \sum_{j<i} a_{ij} \phi_j^{k+1} - \sum_{j>i} a_{ij} \phi_j^k \right). \quad (\text{A.10})$$

Therefore, the resulting set of iterative equations (after dropping the ijk subscript for brevity) is

$$u^{k+1} = \bar{u}^k - \frac{\left(\frac{\partial I}{\partial x} \bar{u}^k + \frac{\partial I}{\partial y} \bar{v}^k + \frac{\partial I}{\partial z} \bar{w}^k + \frac{\partial I}{\partial t} \right) \frac{\partial I}{\partial x}}{\alpha + \left(\frac{\partial I}{\partial x} \right)^2 + \left(\frac{\partial I}{\partial y} \right)^2 + \left(\frac{\partial I}{\partial z} \right)^2} \quad (\text{A.11})$$

$$v^{k+1} = \bar{v}^k - \frac{\left(\frac{\partial I}{\partial x} \bar{u}^k + \frac{\partial I}{\partial y} \bar{v}^k + \frac{\partial I}{\partial z} \bar{w}^k + \frac{\partial I}{\partial t}\right) \frac{\partial I}{\partial y}}{\alpha + \left(\frac{\partial I}{\partial x}\right)^2 + \left(\frac{\partial I}{\partial y}\right)^2 + \left(\frac{\partial I}{\partial z}\right)^2} \quad (\text{A.12})$$

$$w^{k+1} = \bar{w}^k - \frac{\left(\frac{\partial I}{\partial x} \bar{u}^k + \frac{\partial I}{\partial y} \bar{v}^k + \frac{\partial I}{\partial z} \bar{w}^k + \frac{\partial I}{\partial t}\right) \frac{\partial I}{\partial z}}{\alpha + \left(\frac{\partial I}{\partial x}\right)^2 + \left(\frac{\partial I}{\partial y}\right)^2 + \left(\frac{\partial I}{\partial z}\right)^2}. \quad (\text{A.13})$$

Laplacian Motion Field Smoothness

Extending the Horn & Schunck algorithm to Laplacian-smooth regularization requires reformulation of the functional $\Phi(u, v, w)$. While the overall form remains as

$$\Phi(u, v, w) = \int_{\Omega} \left(\left(\frac{\partial I}{\partial x} u + \frac{\partial I}{\partial y} v + \frac{\partial I}{\partial z} w + \frac{\partial I}{\partial t} \right)^2 + \alpha E_s \right) dx dy dz, \quad (\text{A.14})$$

The E_s is in this case defined as

$$E_s = (\nabla^2 u)^2 + (\nabla^2 v)^2 + (\nabla^2 w)^2, \quad (\text{A.15})$$

where the Laplacian operator ∇^2 is defined as

$$\nabla^2 = \frac{\partial^2}{\partial x^2} + \frac{\partial^2}{\partial y^2} + \frac{\partial^2}{\partial z^2}. \quad (\text{A.16})$$

Minimization of $\Phi(u, v, w)$ is again performed by the Euler-Lagrange equations, which in this case yield the following system of equations

$$\nabla^4 u = \frac{1}{\alpha} \left(\frac{\partial I}{\partial x} u + \frac{\partial I}{\partial y} v + \frac{\partial I}{\partial z} w + \frac{\partial I}{\partial t} \right) \frac{\partial I}{\partial x} \quad (\text{A.17})$$

$$\nabla^4 v = \frac{1}{\alpha} \left(\frac{\partial I}{\partial x} u + \frac{\partial I}{\partial y} v + \frac{\partial I}{\partial z} w + \frac{\partial I}{\partial t} \right) \frac{\partial I}{\partial y} \quad (\text{A.18})$$

$$\nabla^4 w = \frac{1}{\alpha} \left(\frac{\partial I}{\partial x} u + \frac{\partial I}{\partial y} v + \frac{\partial I}{\partial z} w + \frac{\partial I}{\partial t} \right) \frac{\partial I}{\partial z}, \quad (\text{A.19})$$

where ∇^4 is the biharmonic operator defined as

$$\begin{aligned} \nabla^4 &= \nabla^2 \nabla^2 = \left(\frac{\partial^2}{\partial x^2} + \frac{\partial^2}{\partial y^2} + \frac{\partial^2}{\partial z^2} \right)^2 = \\ &= \frac{\partial^4}{\partial x^4} + \frac{\partial^4}{\partial y^4} + \frac{\partial^4}{\partial z^4} + 2 \frac{\partial^4}{\partial x^2 y^2} + 2 \frac{\partial^4}{\partial x^2 z^2} + 2 \frac{\partial^4}{\partial y^2 z^2}. \end{aligned} \quad (\text{A.20})$$

In two-dimensional problems, the numerical approximation of the biharmonic operator can be obtained from 2D convolution of 5-point 2D Laplacian kernels

$$k = \begin{bmatrix} 0 & 1 & 0 \\ 1 & -4 & 1 \\ 0 & 1 & 0 \end{bmatrix}, \quad (\text{A.21})$$

yielding the following differencing scheme:

$$\begin{aligned} \nabla^4 \psi_{i,j} = & -20\psi_{i,j} + 8(\psi_{i+1,j} + \psi_{i-1,j} + \psi_{i,j+1} + \psi_{i,j-1}) \\ & - 2(\psi_{i+1,j+1} + \psi_{i+1,j-1} + \psi_{i-1,j+1} + \psi_{i-1,j-1}) \\ & - 1(\psi_{i+2,j} + \psi_{i-2,j} + \psi_{i,j+2} + \psi_{i,j-2}). \end{aligned} \quad (\text{A.22})$$

Similarly, the biharmonic operator in 3D can be obtained by 3D convolution of two 7-point Laplacian kernels (center-point weight is -6, 6 nearest neighbors have weight 1), yielding the following finite-difference approximation

$$\begin{aligned} \nabla^4 \psi_{i,j,k} = & -42\psi_{i,j,k} + 12(\psi_{i+1,j,k} + \psi_{i-1,j,k} + \psi_{i,j+1,k} + \psi_{i,j-1,k} + \psi_{i,j,k+1} + \psi_{i,j,k-1}) \\ & - 2(\psi_{i+1,j+1,k} + \psi_{i+1,j-1,k} + \psi_{i-1,j+1,k} + \psi_{i-1,j-1,k}) \\ & - 2(\psi_{i+1,j,k+1} + \psi_{i-1,j,k+1} + \psi_{i,j+1,k+1} + \psi_{i,j-1,k+1}) \\ & - 2(\psi_{i+1,j,k-1} + \psi_{i-1,j,k-1} + \psi_{i,j+1,k-1} + \psi_{i,j-1,k-1}) \\ & - 1(\psi_{i+2,j,k} + \psi_{i-2,j,k} + \psi_{i,j+2,k} + \psi_{i,j-2,k} + \psi_{i,j,k+2} + \psi_{i,j,k-2}). \end{aligned} \quad (\text{A.23})$$

We can then proceed by expressing the biharmonic term as

$$\nabla^4 \psi_{i,j,k} = \bar{\bar{\psi}}_{i,j,k} - \psi_{i,j,k}, \quad (\text{A.24})$$

where $\bar{\bar{\psi}}_{i,j,k}$ is defined as

$$\begin{aligned} \bar{\bar{\psi}}_{i,j,k} = & \frac{12}{42}(\psi_{i+1,j,k} + \psi_{i-1,j,k} + \psi_{i,j+1,k} + \psi_{i,j-1,k} + \psi_{i,j,k+1} + \psi_{i,j,k-1}) \\ & - \frac{2}{42}(\psi_{i+1,j+1,k} + \psi_{i+1,j-1,k} + \psi_{i-1,j+1,k} + \psi_{i-1,j-1,k}) \\ & - \frac{2}{42}(\psi_{i+1,j,k+1} + \psi_{i-1,j,k+1} + \psi_{i,j+1,k+1} + \psi_{i,j-1,k+1}) \\ & - \frac{2}{42}(\psi_{i+1,j,k-1} + \psi_{i-1,j,k-1} + \psi_{i,j+1,k-1} + \psi_{i,j-1,k-1}) \\ & - \frac{1}{42}(\psi_{i+2,j,k} + \psi_{i-2,j,k} + \psi_{i,j+2,k} + \psi_{i,j-2,k} + \psi_{i,j,k+2} + \psi_{i,j,k-2}). \end{aligned} \quad (\text{A.25})$$

Under this definition of $\bar{\psi}_{i,j,k}$ the iterative Gauss-Seidel equations have a form identical to the standard Horn & Schunck formulation:

$$u^{k+1} = \bar{u}^k - \frac{\left(\frac{\partial I}{\partial x} \bar{u}^k + \frac{\partial I}{\partial y} \bar{v}^k + \frac{\partial I}{\partial z} \bar{w}^k + \frac{\partial I}{\partial t} \right) \frac{\partial I}{\partial x}}{\alpha + \left(\frac{\partial I}{\partial x} \right)^2 + \left(\frac{\partial I}{\partial y} \right)^2 + \left(\frac{\partial I}{\partial z} \right)^2} \quad (\text{A.26})$$

$$v^{k+1} = \bar{v}^k - \frac{\left(\frac{\partial I}{\partial x} \bar{u}^k + \frac{\partial I}{\partial y} \bar{v}^k + \frac{\partial I}{\partial z} \bar{w}^k + \frac{\partial I}{\partial t} \right) \frac{\partial I}{\partial y}}{\alpha + \left(\frac{\partial I}{\partial x} \right)^2 + \left(\frac{\partial I}{\partial y} \right)^2 + \left(\frac{\partial I}{\partial z} \right)^2} \quad (\text{A.27})$$

$$w^{k+1} = \bar{w}^k - \frac{\left(\frac{\partial I}{\partial x} \bar{u}^k + \frac{\partial I}{\partial y} \bar{v}^k + \frac{\partial I}{\partial z} \bar{w}^k + \frac{\partial I}{\partial t} \right) \frac{\partial I}{\partial z}}{\alpha + \left(\frac{\partial I}{\partial x} \right)^2 + \left(\frac{\partial I}{\partial y} \right)^2 + \left(\frac{\partial I}{\partial z} \right)^2}. \quad (\text{A.28})$$

A.1 Euler-Lagrange Equations

The general form of the Euler-Lagrange equations for a functional $L(x, f(x), \frac{\partial f}{\partial x}, \dots, \frac{\partial^k f}{\partial x^k})$ is

$$\frac{\partial L}{\partial f} - \frac{d}{dx} \frac{\partial L}{\partial \frac{\partial f}{\partial x}} + \frac{d^2}{dx^2} \frac{\partial L}{\partial \frac{\partial^2 f}{\partial x^2}} - \dots - (-1)^k \frac{d^k}{dx^k} \frac{\partial L}{\partial \frac{\partial^k f}{\partial x^k}} = 0. \quad (\text{A.29})$$

A.1.1 Gradient-Smooth Horn & Schunck

The Euler-Lagrange equations yield the following equations for the first-order smoothing of the motion field:

$$\begin{aligned} \frac{\partial F(x, y, z, u, v, w)}{\partial u(x, y, z)} - \frac{d}{dx} \frac{\partial F(x, y, z, u, v, w)}{\partial \frac{\partial u(x, y, z)}{\partial x}} - \\ - \frac{d}{dy} \frac{\partial F(x, y, z, u, v, w)}{\partial \frac{\partial u(x, y, z)}{\partial y}} - \frac{d}{dz} \frac{\partial F(x, y, z, u, v, w)}{\partial \frac{\partial u(x, y, z)}{\partial z}} = 0 \end{aligned} \quad (\text{A.30})$$

$$\begin{aligned} \frac{\partial F(x, y, z, u, v, w)}{\partial v(x, y, z)} - \frac{d}{dx} \frac{\partial F(x, y, z, u, v, w)}{\partial \frac{\partial v(x, y, z)}{\partial x}} - \\ - \frac{d}{dy} \frac{\partial F(x, y, z, u, v, w)}{\partial \frac{\partial v(x, y, z)}{\partial y}} - \frac{d}{dz} \frac{\partial F(x, y, z, u, v, w)}{\partial \frac{\partial v(x, y, z)}{\partial z}} = 0 \end{aligned} \quad (\text{A.31})$$

$$\begin{aligned} \frac{\partial F(x, y, z, u, v, w)}{\partial w(x, y, z)} - \frac{d}{dx} \frac{\partial F(x, y, z, u, v, w)}{\partial \frac{\partial w(x, y, z)}{\partial x}} - \\ - \frac{d}{dy} \frac{\partial F(x, y, z, u, v, w)}{\partial \frac{\partial w(x, y, z)}{\partial y}} - \frac{d}{dz} \frac{\partial F(x, y, z, u, v, w)}{\partial \frac{\partial w(x, y, z)}{\partial z}} = 0. \end{aligned} \quad (\text{A.32})$$

A.1.2 Laplacian-Smooth Horn & Schunck

In the second-order (Laplacian) regularization the Euler-Lagrange equations take the form

$$\begin{aligned} \frac{\partial F(x, y, z, u, v, w)}{\partial u(x, y, z)} + \frac{d^2}{dx^2} \frac{\partial F(x, y, z, u, v, w)}{\partial \frac{\partial^2 u(x, y, z)}{\partial x^2}} + \\ + \frac{d^2}{dy^2} \frac{\partial F(x, y, z, u, v, w)}{\partial \frac{\partial^2 u(x, y, z)}{\partial y^2}} + \frac{d^2}{dz^2} \frac{\partial F(x, y, z, u, v, w)}{\partial \frac{\partial^2 u(x, y, z)}{\partial z^2}} = 0 \end{aligned} \quad (\text{A.33})$$

$$\begin{aligned} \frac{\partial F(x, y, z, u, v, w)}{\partial v(x, y, z)} + \frac{d^2}{dx^2} \frac{\partial F(x, y, z, u, v, w)}{\partial \frac{\partial^2 v(x, y, z)}{\partial x^2}} + \\ + \frac{d^2}{dy^2} \frac{\partial F(x, y, z, u, v, w)}{\partial \frac{\partial^2 v(x, y, z)}{\partial y^2}} + \frac{d^2}{dz^2} \frac{\partial F(x, y, z, u, v, w)}{\partial \frac{\partial^2 v(x, y, z)}{\partial z^2}} = 0 \end{aligned} \quad (\text{A.34})$$

$$\begin{aligned} \frac{\partial F(x, y, z, u, v, w)}{\partial w(x, y, z)} + \frac{d^2}{dx^2} \frac{\partial F(x, y, z, u, v, w)}{\partial \frac{\partial^2 w(x, y, z)}{\partial x^2}} + \\ + \frac{d^2}{dy^2} \frac{\partial F(x, y, z, u, v, w)}{\partial \frac{\partial^2 w(x, y, z)}{\partial y^2}} + \frac{d^2}{dz^2} \frac{\partial F(x, y, z, u, v, w)}{\partial \frac{\partial^2 w(x, y, z)}{\partial z^2}} = 0. \end{aligned} \quad (\text{A.35})$$